Doctoral Dissertation (Shinshu University)

The study of biocompatible nanocomposite

September 2016

Yong-Il Ko

Summary

Recently, nanotechnology holds great promise for fabricating next-generation electronic devices, energy storages, sensors, and composite materials. Since small sized materials below micro scale can be applied for nanotechnology, they have been investigated widely and actively in order to fully exploit their size and morphology effect. Especially, the polymeric nanofibers, prepared by the electrospinning system have attracted great attention because of their large surface area to volume ratio and good flexibility in surface functionalities. In addition, carbon materials have been examined as promising nanomaterials in nanotechnology because they are optically active, electrically conductive, and have a sufficiently small size.

However, it is difficult to develop multi-functional nano-biocomposites by incorporating carbon materials into organic nanofiber because both materials exhibit largely different physical and chemical properties and organic nanofibers are electrically insulating and mechanically weak. Furthermore, carbon materials are intrinsically insoluble in an aqueous solution because of their strongly bundled stacked structure as well as their hydrophobic nature. In my PhD thesis, to solve such intrinsic problems as well as to fully exploit their excellent properties in multifunctional biocomposites, I carried out systematic studies to improve mechanical and thermodynamic properties of the organic nanofiber, and also to prepare biocompatible carbon materials by attaching biomolecules to the surface.

In chapter 2, I prepared polylactide-derived nanofiber yarn by coating with silicone elastomer and then examined their shape memory properties in detail. It is confirmed that the mechanical and thermodynamic properties of the polylactide nanofiber yarn were remarkably enhanced via the twisting and annealing process. The coating with silicone elastomer largely improved the mechanical properties of the polylactide nanofiber yarn. Both processes directly contributed to the large enhancement both in the mechanical properties and in the shape memory behaviors.

In chapter 3, the annealing effect on both the thermodynamic properties and the shape memory behaviors of the polycaprolactone nanofiber yarn by coating with silicone elastomer was investigated in detail. The polycaprolactone nanofiber yarn was prepared by twisting organic nanofiber sheets with different thickness using various twist numbers. It is observed that the thermodynamic and mechanical properties were remarkably enhanced with increasing twist numbers and also by annealing process. Moreover, the coating with silicone elastomer has largely contributed to the sustained nanofiber feature of polycaprolactone above the melting point, thereby resulting in their improved toughness.

In chapter 4, I investigated the fabrication of carbon nanotubes-based biocomposite using mussel adhesive protein (MAP) and their promising applications. Firstly, the optical signals of semiconducting carbon nanotubes responded sensitively to external conditions including the formation of chemical bonds. In order to detect the iron-

3,4-dihydroxy-L-phenylalanine (DOPA) conjugation bonds with metal ions, individually dispersed double-walled carbon nanotubes (DWNTs) suspension was prepared via a homogeneous coating of MAP. MAP exhibited a high ability of individually dispersing the bundled DWNTs through the strong physical interactions with the outer tubes. The sensitively altered optical properties of the DWNT suspension upon addition of $FeCl_3$ solution can be explained by the formation of coordinative bonds between DOPA in MAP and Fe^{3+} ion. The iron-DOPA bonds acted as electron acceptors and thus provided a favorable non-radiative channel for the optical depression of signal from semiconducting inner tubes in DWNT suspension. Several physical and chemical effects on the sensitively altered photoluminescence of semiconducting inner tubes were explained based on the iron-DOPA bonds.

Then, I coated the metal-absorbed MAP-DWNTs suspensions on poly (vinylidene fluoride) (PVDF) nanofiber yarn to secure the electrical conductivity as well as the biocompatibility. To remove residual non-conductive MAP partially and also to expose DWNTs, vacuum ultraviolet irradiation was utilized to increase the electric conductivity of PVDF nanofiber yarn. Finally, electrically conductive, mechanically strong and biologically active PVDF yarn, prepared by coating with MAP-DWNT was characterized using various analytical tools.

Furthermore, I prepared DWNT-based aerogel via the self-assembled combination of MAP with ssDNA-dispersed DWNTs, followed by sol-gel and freeze drying processes. The coacervation process was confirmed using Raman/fluorescence and UV-Vis-NIR spectroscopy, and using dynamic light scattering. Furthermore, the mechanical and electrical properties were measured to verify the fabrication of the optically active, mechanically strong, electrically conductive, and biologically active aerogel.

In this thesis, I achieved the large improvement both in the mechanical and in the thermodynamic properties of the biodegradable polymer-derived nanofiber and their improved shape memory properties. Moreover, I demonstrated the effectiveness of MAP as a biocompatible dispersing agent for strongly bundled hydrophobic DWNTs based on the physical interaction between biomolecules and the sidewall of the tube. Then, I suggested the interesting application of bio-inspired DWNTs as multifunctional coating materials for improving mechanical and electrical properties as well as the biocompatibility of PVDF nanofiber yarn. Furthermore, the judicious combination of ssDNA with MAP makes it possible to produce carbon nanotube based aerogel, where DWNTs acted as reinforcing filler and also cross-linker. It is expected that experimental results I achieved will play a great role for developing multi-functional scaffold, bone-tissue engineering and drug delivery system in biomedical areas. Eventually, it is envisaged that environmentally friendly carbon materials can be applied for the fabrication of the biocompatible electronic device and gas absorption devices, where the electrical conductivity, mechanical strength and good biocompatibility are critically required.

Abbreviation

AFM	atomic force microscopy
BWF	Breit-Wigner-Fano
CNT	Carbon nanotube
DCM	dichloromethane
DLS	dynamic light scattering
DMA	dynamic mechanical analysis
DMF	N,N-dimethylformamide
DOPA	3,4-dihydroxy-L-phenylalanine
DWNT	double-walled carbon nanotube
E′	storage modulus
EDS	energy dispersive spectroscopy
MAP	mussel-adhesive protein
Mgfp	mytilus galloprovincialis foot protein
MWNT	multi-walled carbon nanotube
PCL	Polycaprolactone
PL	photoluminescence
PLLA	poly (L-lactide)
PVDF	Poly (vinylidene fluoride)
RBM	radial breathing modes
SDBS	sodium dodecyl benzene sulfonate
SDS	sodium dodecyl sulfonate
SEM	scanning electron microscope
SME	shape memory effect
SMP	shape memory polymers
ssDNA	single stranded deoxyribonucleic acid
SWNT	single-walled carbon nanotube
T/m	number of twists
tan δ	loss factor
TEM	transmission electron microscope
T_g	glass transition temperature
T_m	melting temperature

T_{trans}	transition temperature
UTM	universal testing machine
UV–vis–NIR	ultraviolet-visible-near Infrared
VUV	vacuum ultraviolet
WAXD	wide-angle X-ray diffraction
XPS	X-ray photoemission spectroscopy
XRD	X-ray Diffraction

Contents

List of Figures

List of Tables

Chapter 1

General Introduction

Chapter 1 General Introduction

1.1 Electrospinning

The electrospinning is the spinning process of synthetic fibers through the help of electrostatic forces with high voltage, and this process is capable of producing fibers in the nano- or submicron- range.[1] Electrospinning has attracted a great deal of attention in the last decade due to not only versatility for spinning with wide variety of polymers but also uniformity for producing fibers in the submicron range. Generally, fibers having diameters below 100 nm are commonly classified as nanofibers.[2] These fibers, with higher surface area and smaller pores than those of regular fibers, could be applied for variety of applications such as optical electronics, filtration, nanocatalysis, tissue scaffolds, and protective clothing. The electrospinning process applies the high voltage electric field in order to form the electrically charged jets from polymer solution, and produced jet was converted to nanofibers by rapid evaporation. The highly charged fibers are directed towards the oppositely charged collector, which can be a rotating drum or a flat plate.

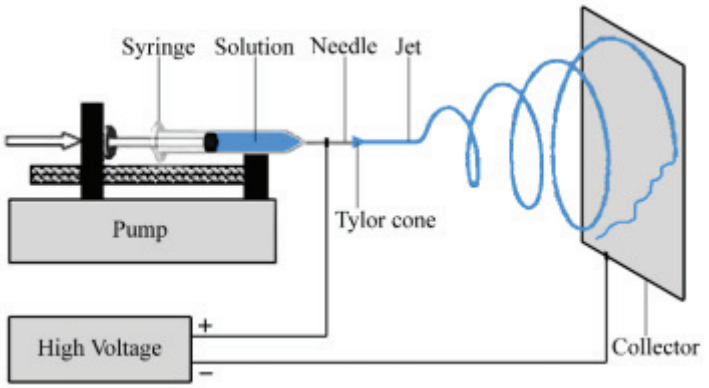

Figure 1.1 Schematic of electrospinning process [3]

1.1.1 Process Parameters

During electrospinning process, the charge transportation by the applied voltage cause the flow of the jet in the direction of the collector, and the control of the current affect the mass flow of the polymer at the nozzle tip.[4, 5] Thus, the applied voltage is a main parameter of the morphology and structure, because it directly influences the formation of Taylor cone and jet initiating point. The distance between from the nozzle to collector also affects the structure and morphology of electrospun nanofibers due to their dependence on the evaporation rate of solvent and deposition time.[6, 7] And the spinnability is easily affected by the flow rate of the polymer solution at the syringe because it influences the jet velocity and the material transfer rate.[7] Environmental

conditions during electrospinning process including the temperature, relative humidity (RH) of surrounding air and vacuum conditions affect the fiber structure and morphology of electrospun nanofibers, because they directly influence the evaporation rate and deposition time.[7, 8]

1.1.2 Solution Parameters

Due to the viscosity and surface tension of polymer solution could greatly affect the spinning ability, solution concentration is highly influential in the electrospinning process. [9] Generally, low concentration solution could induce the droplet shape by low surface tension, while higher concentration could prohibit nanofiber formation by higher viscosity. Furthermore, the jet formation is influenced by solution conductivity. The charged ions in the polymer solution enhance the charge carrying capacity of the jet, thereby subjecting it to higher tension with the applied electric field with high voltage.[10, 11]

1.1.3 Properties of Nanofibers

The thermal and mechanical properties of the electrospun nanofibers have marked differences compared to conventional fibers and bulk polymers.[12] From several published reports concerning thermal analysis of electrospun polymeric nanofibers, nanofibers have lower crystallinity, glass transition temperature (T_g), and melting temperature (T_m) than that of firm, regular fiber or powder shape even though same polymer. The high evaporation rate followed by rapid solidification at the final stages of electrospinning is expected to be the reason for the low crystallinity. [11, 13, 14]

Nanofibers have nanostructured surface morphologies which could affect mechanical properties such as tensile strength, Young`s modulus and elongation. Generally, electrospun nanofibers have shown reduced mechanical properties when compared with conventional fiber and cast films due to their lower crystallinity and highly pored structure. [10, 15] Therefore, additional processes will be needed to overcome these drawbacks.

1.2 Shape Memory Polymers

Shape-memory polymers (SMPs) are polymeric smart materials having the ability to return from “deformed” temporary shape to their “memorized” permanent shape triggered by an external stimulus such as heat, light, magnetic fields, electrical and pH change. Shape memory effects (SME) could be arose by the combination of a suitable molecular network design and programming process. Generally, molecular network include net-points and chain segment, which are sensitive to an external stimulus.

Therefore, thermoplastic SMPs are usually phase-separated materials, and they consist of at least two different domains, which are related to different thermal transition temperatures (T_{trans}). Therein the domains having higher T_{trans} (glass transition temperature T_g or melting temperature T_m) are called hard domains and are working as net points. This hard domain determines the permanent shape by physical (intermolecular interactions) or chemical (covalent bonds) nature to fix their permanent shape. The thermosensitive chain segments having lower thermal transition (T_g or T_m) are called switching domain.

The temporarily fixation of deformed shape (shape A in Figure 1.2) is occurred after extension under heat and cooling process by forming the additional reversible crosslinks within switching domains. These secondary temporary crosslinks could be formed by chemical bond or physical interaction such as crystallization (T_m) or vitrification (T_g). In this step, strain energy of switching domains is remained in the materials. By reheating, the glassy domains will return to the viscous state (T_g) or the crystallites will melt (T_m). Thus, the residual stress is released, then, the deformed shape is recovered to original permanent shape. Examples for polymer network architectures suitable to exhibit an SME are displayed in Figure 1.3.

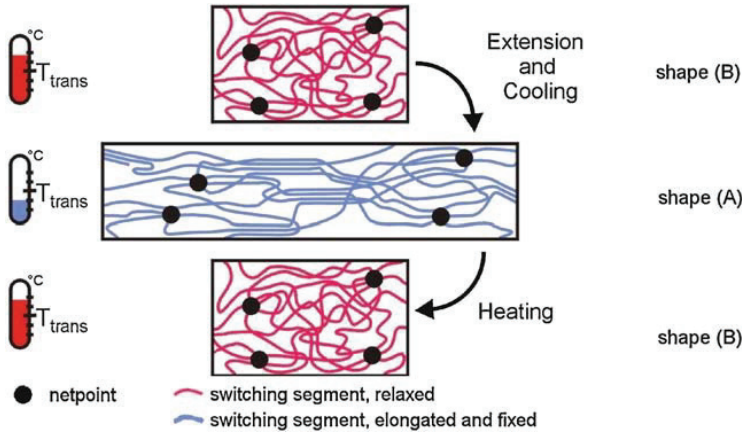

Figure 1.2 Molecular mechanism of the thermal-triggerd SME. T_{trans} is the thermal transition temperature (T_m or T_g) of the switching domain.[16]

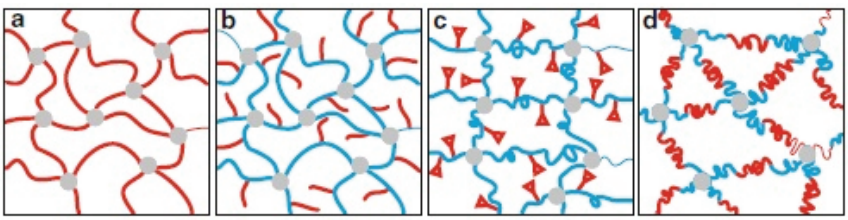

Figure 1.3 Examples for polymer network structure for exhibiting an SME (molecular switches: red; net-points: gray): (**a**) switching segments linking net-points, (**b**) side chains as switching segments, (**c**) functional groups as molecular switches capable to reversibly form a covalent bond, (**d**) ABA triblock segments linking net-points.[16]

1.3 Carbon Nanotubes

1.3.1 What is Carbon Nanotube?

Carbon nanotube (CNT) is allotropes of carbon which is a seamless long cylinder by rolling up graphite sheet which has the sp^2 carbon honeycomb lattice. It has a nano-sized diameter and its rolled-up layer has a one-atom level thickness. (Figure 1.4).[17-19] Since their unique configuration of cylindrical carbon molecules induce excellent properties, they have attracted a great deal of attention in various applications in nanotechnology.[20] For example, the Young's modulus is higher than any other material[21, 22] and their tensile strength is also 100 times higher than that of steel. Moreover, electrical current density is 100 times greater than for copper wire.

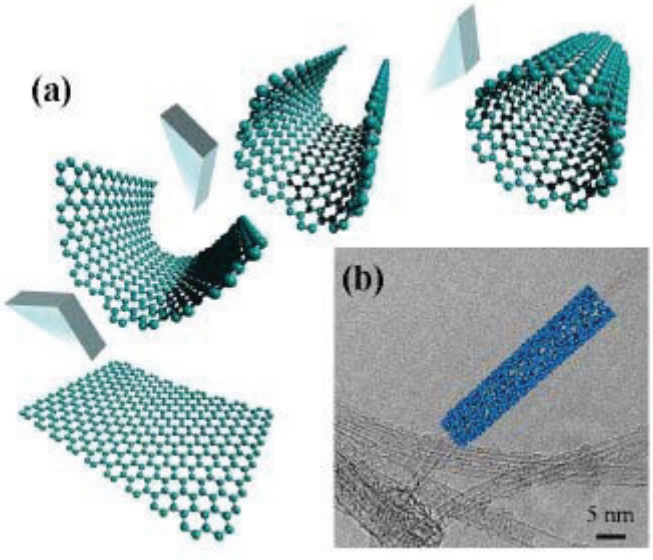

Figure 1.4 (a) A schematic diagram describing how CNT is made by rolling a single graphene (sp^2 carbon honeycomb lattice). (b) A typical high-resolution transmission electron microscope image of CNT.

Generally, CNTs can be classified according to the number of wall; Single-walled carbon nanotube (SWNTs), double walled carbon nanotubes (DWNTs) and multi-walled carbon nanotubes (MWNTs)(Figure 1.5). The diameter of SWNTs is about 1-2 nm and the length is between 0.2 and 5um, and their size usually depends on the synthetic method.[23] The aspect ratio (length to diameter) of SWNTs is over 10,000 due to SWNTs are regarded as one-dimensional material. These shape lead to quantum confinement of the wave vectors in the circumferential directions, although plane wave propagation occurring only along the nanotube axis. DWNTs have inner and outer tubes with 1-2nm of diameters.[24] double-walled carbon nanotubes (DWNTs), consisting of two coaxial

tubules have several advantages over single- and multi-walled carbon nanotubes (SWNTs and MWNTs) for various applications due to their unique optical and physicochemical properties.[25, 26] Because of buffer-like function of the outer tube, optical activity of the inner tube is largely different from the outer one with regard to external stimulus.[27-30] MWNTs consist of three or more walls of concentric graphene sheets, and their diameters are in the range of 2-100 nm. Also chirality of each tube is independent, thus they has larger inter-shell spacing than that of graphite. These unique structures of SW-, DW and MWNTs demonstrate that they are characteristic one-dimensional materials with attractive optical, electronic, thermal, mechanical, and chemical properties.

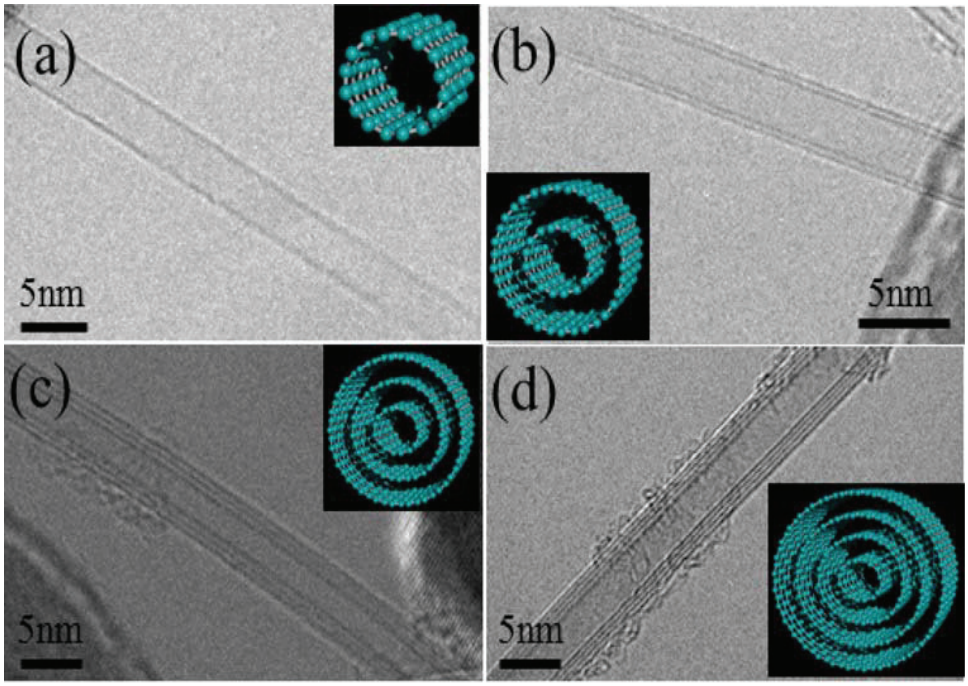

Figure 1.5 High resolution transmission electron microscopy (HR-TEM) images of (a) single-, (b) double-, (c) triple-, and (d) four-walled carbon nanotubes (CNTs, insets are their corresponding models). [24]

1.3.2 The Electric Properties of Carbon Nanotubes

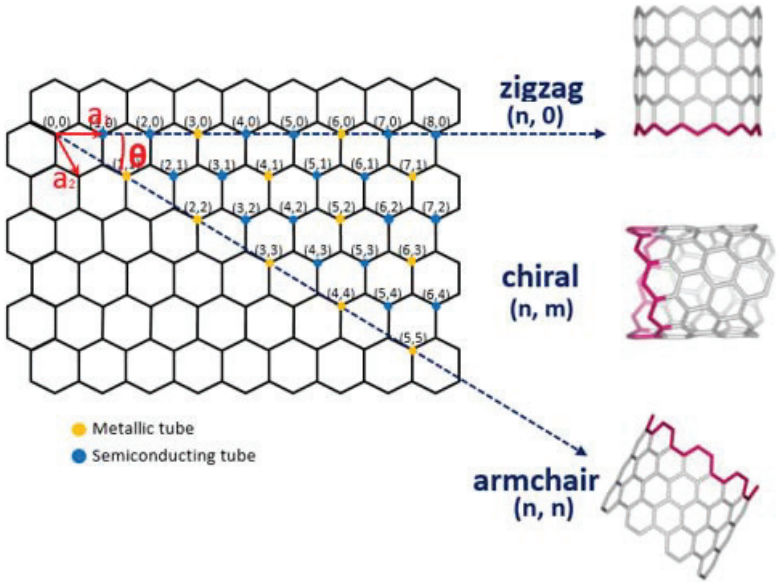

Figure 1.6 Schematic models of SWNTs from rolled up the graphite sheet in a certain orientation.

Most material conductors can be classified as either metals or semiconductors and it is usually determined on bandgap meaning the distance between valance band and conduction band.[31]

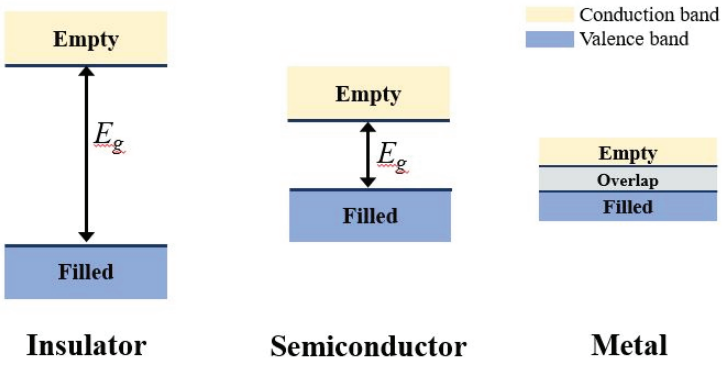

Figure 1.7 Bandgap, valence band, conduction band of insulator, semiconductor, and metal.

However, CNTs can be either metallic or semiconducting based on their chiral structures. Because CNTs can be rolled from a graphene sheet in many ways, thus there are many passible orientations of the hexagonal structure. The chirality structure can be indicated by two indices, (n,m).[17] The CNTs (n,m) represent metallic properties when n- m = 3q and q = 0, 1, 2, ⋯ and semiconducting properties when n - m = 3q ± 1 and q = 0, 1 , 2, ⋯.[31-33] Such interesting electronic properties are induced by quantum

confinement in the circumferential direction, thus electrons can propagate only along the nanotube axis, and so to their wave vector points. [34-36]

Moreover, because the crossing points between the quantization lines of wave vector and the Dirac point depend on the chiral angle, so that electric properties of CNTs are chirality (n,m) dependence. [37] The resulting number of conduction and valence bands effectively depends on the standing waves that are set up around the circumference of the CNTs. They have the sharp intensities (spikes) in the density of states which known as van Hove singularities and are the result of this one-dimensional quantum conduction. Consequently, the band gap for the metallic and semiconducting nanotubes is dependent of the tube diameter and chirality.

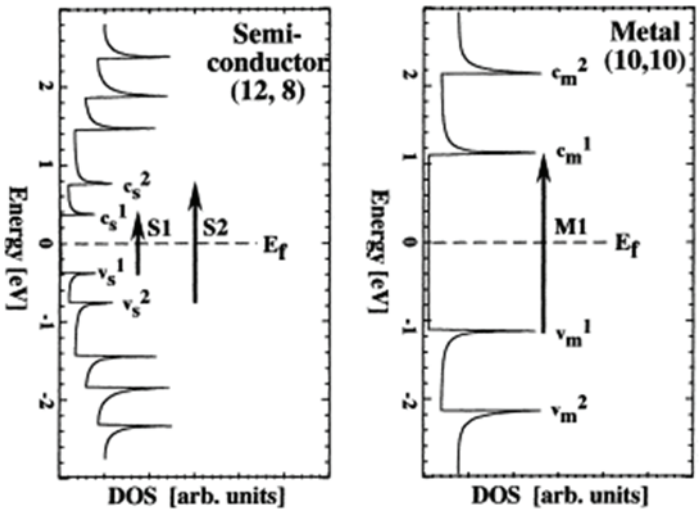

Figure 1.8 Density of electron states of (12,8) semiconducting and (10,10) metallic SWNT. [38]

1.3.3 The Physical Properties of Carbon Nanotubes

CNTs are known as one of the best thermal conductors. From their unique quantization of the phonon structure, carbon nanotubes are expected to have high thermal conductivity. The thermal conductivity of SWNTs at room temperature has been predicted to be extremely high, exceeding even that of graphite or diamond. In case of a isolated (10,10) SWNT, the thermal conductivity was measured to be 6,600 W/m·K, which exceeds that of isotopically pure diamond by 2 times.[39, 40]

Also CNTs have excellent mechanical strength. The sp^2 carbon-carbon bond in the graphite sheet with a planar honeycomb lattice is the strongest of all chemical bonds, with the great Young's modulus of graphene (1,086GPa). [40] As same reason, the Young`s modulus of SWNT was reported with a value of 1.06TPa by theoretical simulation and experimental measurement.[41] This remarkable mechanical properties of CNTs will make them useful for various applications.

1.3.4 Optical Analysis for Carbon Nanotubes

CNTs are nano-sized cylindrical materials and they have wide range of the diameter distribution, chirality, diameter, defects and impurity according to the synthetic, purification and post-treatment method.[42] CNTs are originally exhibit as a form of a large aggregated bundle structure. However, nanotubes could be isolated by using surfactant to disperse homogeneously. Therefore, it is necessary to identify these bundled and isolated tubes to verify their fundamental properties.

1.3.4.1 Raman Spectroscopy

Raman spectroscopy is remarkably efficient optical tool with quick and non-destructive process to characterize the optochemical properties of materials. The incident light excites an electron to a higher transition state from ground state, and the excited electron interacts with a phonon by electron-phonon coupling before returning to the original ground state. The energy of light with the non-elastic scattering is measured in respect to the vibrational wavenumber (cm^{-1}), and commonly, the Stokes scattering that stronger signal from the loss side is counted as positive.[37]

In the case of CNTs, because of the density of states is sharply peaked, signal of resonance Raman scattering between van Hove transitions is significantly stronger than non-resonant behavior. Hence, resonance Raman scattering with nanotubes gives important information of the vibrational mode from the Raman shift, as well as of the optical transition energy between each van Hove transitions, since their energy gap is close to the energy of the laser.[37] Thus, Raman spectroscopy can provide the comprehensive information of CNTs such as electronic structure, diameter, crystallinity, purity, chirality and chirality.[43]

Generally, there are several characteristic peaks in the Raman spectra of CNTs: the radial breathing mode (RBM) at low-frequency and the D, G and 2D (G') modes higher frequency. Among them, distinctive Raman line of the tubular structure without in graphite is RBM, in which all carbon atoms vibrate towards circumferential direction in phase perpendicular to the axis changing the radius of the tubes.[44] The frequency of RBM provides the information of the chirality and diameter. The RBM signals are also helpful for observation of the surrounding environment of the side wall of nanotubes.

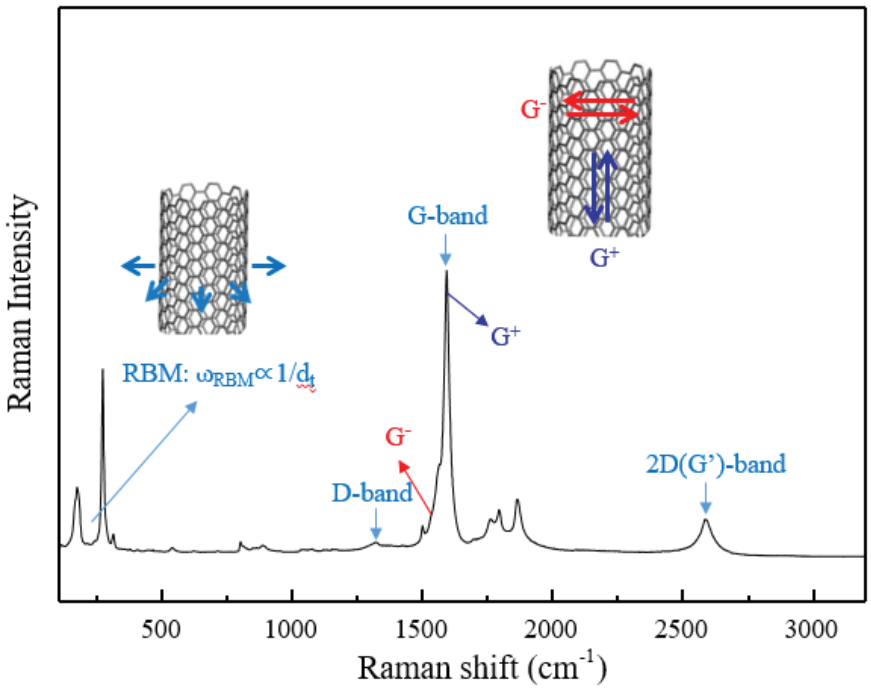

Figure 1.9 Raman spectra from a bundle DWNTs sample (excited with 785nm)

1.3.4.2 UV-Vis-NIR spectroscopy

Optical absorption spectroscopy has been used to determine the not only concentration of CNTs in the solution but also agglomeration of SWNTs in suspensions. This tool has the ability to probes the joint density of electronic states of CNTs.[45] According to Beer-Lambert's law ($A = log\ Io/I = \varepsilon\ C\ l$), the absorbance A is directly proportional to concentration of nanotubes C when extinction coefficient ε and light path l are fixed, hence the absorption intensity is proportional to the amount of CNTs dissolved in the solution. Furthermore, when CNTs are isolated in aqueous solution, each energy gap of the individual CNTs corresponding van Hove singularity is separated. Thus, sharpened absorption peaks are released, and these phenomenon can be considered as the direct indicator of dispersion state.[46]

1.3.4.3 Photoluminescence

Photoluminescence (PL) has been used to observe the band gap of semiconducting CNTs. In general, agglomeration of nanotubes with bundled structure quenches the photoluminescence by interactions of side-by-side contact with van-der Waals force. Thus the bright emission spectra show evidence of the individually isolated CNTs. [43, 47, 48] Moreover, PL maps have been widely useful for verifying the (n, m) distribution of semiconducting SWNTs.[48, 49]

1.4 Mussel Adhesive Protein

1.4.1 What is Mussel Adhesive Protein?

Mussel is one of the most exciting underwater creatures that have high ability of adhering to the organic and/or inorganic substrate in saltwater. [50-52] Even though the adhesion of most glues or tapes usually decrease in soaked environments, mussels tightly attached rock with regard to tides, waves in saline water. [53] The secret of their unusual properties is due to the special protein on their byssal threads. The end of each thread consists of an adhesive plaque containing mussel adhesive protein (MAP) that allows mussel to stick to various surfaces, including plastic, metal, even Teflon.[53-55] Because of these marvelous ability of MAPs, they have been considered as a potential powerful bio-adhesive and their adhesion mechanism has been studied.[56-58]

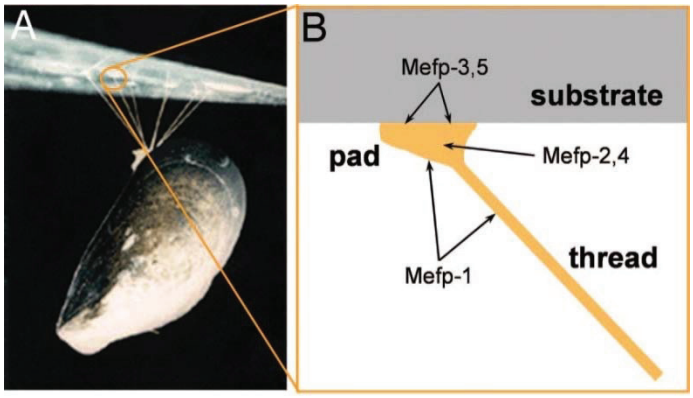

Figure 1.10 (a) Real image of MAP adhering to substrate, and (b) scheme of thread of MAP near substrate.[59, 60]

1.4.2 The Structure of Mussel Adhesive Protein

MAP, usually extracted from mussel or recombinant, consists of some kinds of mussel foot protein. Particularly, there are several proteins participating adherence in the end of plaque from byssal thread, and those adhesive proteins were called as foot protein type 1 (fp-1) to type 6 (fp-6), respectively.[54, 61-64] The interesting thing is that all of them contain rich amount of certain amino acid, L-3,4-dihydroxyphenylalanine (DOPA), which is made via hydroxylation from the amino acid L-tyrosine. [62, 63]

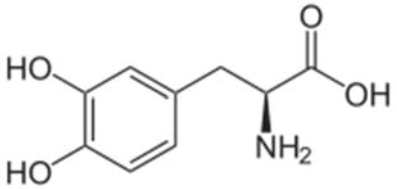

Figure 1.11 Chemical structure of L-3,4-dihydroxyphenylalanine (DOPA)

Catechol (3,4-dihydroxyphenyl) groups in DOPA could form strong hydrogen bonds with hydrophilic materials and also they bond with metal ion and metal oxide. [65-67] DOPA moieties are able to cross-link each other by oxidation and then converto to DOPA-quinone.[60] It was reported that more DOPAs in MAP, especially fp-3 and fp-5, are encased near the contact interface.[62, 63] In addition, MAPs not containing DOPA showed very low level of ability to adhere.[68] From these reports, DOPA is the key material of distinct ability for adhesion of mussel.

Table 1.1 Chemical structure of L-3,4-dihydroxyphenylalanine (DOPA)[69]

Protein	Mass (kDa)	DOPA (mol%)	Features
fp-1	~110	~13	- about 80 times repeats of AKPSYPPTYK - two variants, basic protein - surface coating
fp-2	~40	~3	- Cysteine rich - abundant in adhesion plaque
fp-3	~6	~20	- arginine rich, hydroxyarginine - 20~30 variants - surface adhesion
fp-4	~80	~5	- histidine, lysine, arginine rich - Cu2+ binding
fp-5	~9.5	~30	- phosphoserine - YK or YH repeats - surface adhesion
fp-6	~11	~4	- cysteine rich (~11 mol%)

1.4.3 The Properties of Mussel Adhesive Protein

MAP has received a great deal of attention because of its unique properties and benefits, so that many researches are ongoing for its commercialization. MAP has a good ability to adhere to a variety of substrates like plastics, metals, ceramic, Teflon (the hydrophobic natures), and even cell or skin of living bodies. [55] Its adhesion strength does not change in humid environment. [50] It is highly biocompatible so that doesn't show inflammation or immunogenicity. [56, 57] Finally, it doesn't show harmful effect on environments as it is biodegradable. [56-58]

It was reported that the adhering properties of MAP results from the formation of chemical bonding of catechol groups and chemical functional group in DOPA. The adhesion force of one catechol molecule was quantitatively measured by atomic force microscopy (AFM).[69] The adhesion force was measured as one catechol molecule attached to AFM tip was passed on two different surfaces. The adhesion force of catechol on TiO_2 surface was the degree of coordinate bonding force. DOPA residue contacting a wet metal oxide surface revealed a surprisingly high strength yet fully reversible, noncovalent interaction. There was oxidation of catechol group in DOPA, as occurs during curing of the secreted mussel glue, the oxidation dramatically reduced the strength of the interaction to metal oxide but results in high strength irreversible covalent bond formation to an organic surface.[59]

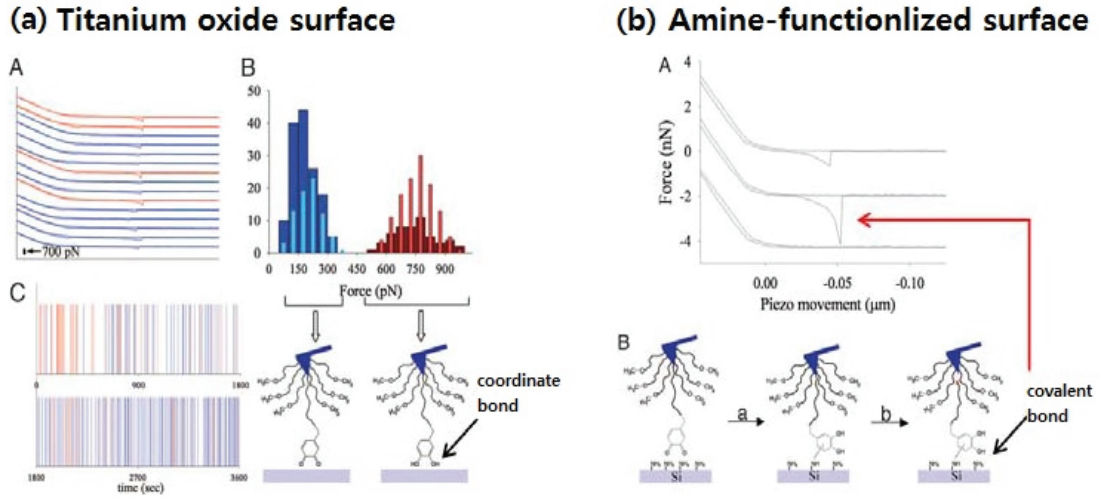

Figure 1.12 Adherence force of catechol in MAP for (a) TiO2 surface and (b) amine-functionalized surface measured using AFM.[59]

1.5 Reference

[1] A. Greiner, J.H. Wendorff, *Angew Chem Int Edit,* **46**, 5670-5703, (2007)
[2] A. MacDiarmid, W. Jones, I. Norris, J. Gao, A. Johnson, N. Pinto, J. Hone, B. Han, F. Ko, H. Okuzaki, *Synthetic Metals,* **119**, 27-30, (2001)
[3] M. Ziabari, V. Mottaghitalab, A.K. Haghi, *Braz J Chem Eng,* **26**, 53-62, (2009)
[4] J. Deitzel, J. Kleinmeyer, J. Hirvonen, N.B. Tan, *Polymer,* **42**, 8163-8170, (2001)
[5] G. Taylor, Electrically driven jets, Proceedings of the Royal Society of London A: Mathematical, Physical and Engineering Sciences, The Royal Society, 1969, pp. 453-475.
[6] J. Deitzel, N. Beck Tan, J. Kleinmeyer, J. Rehrmann, D. Tevault, D. Reneker, I. Sendijarevic, A. McHugh, Army Research Laboratory Technical Report, ARL-TR-1989, 1999.
[7] S. Megelski, J.S. Stephens, D.B. Chase, J.F. Rabolt, *Macromolecules,* **35**, 8456-8466, (2002)
[8] P.K. Baumgarten, *Journal of colloid and interface science,* **36**, 71-79, (1971)
[9] J.M. Deitzel, J. Kleinmeyer, D. Harris, N.C.B. Tan, *Polymer,* **42**, 261-272, (2001)
[10] C.J. Buchko, L.C. Chen, Y. Shen, D.C. Martin, *Polymer,* **40**, 7397-7407, (1999)
[11] X. Zong, K. Kim, D. Fang, S. Ran, B.S. Hsiao, B. Chu, *Polymer,* **43**, 4403-4412, (2002)
[12] T. Subbiah, G.S. Bhat, R.W. Tock, S. Pararneswaran, S.S. Ramkumar, *J Appl Polym Sci,* **96**, 557-569, (2005)
[13] J. Deitzel, J. Kleinmeyer, D. Harris, N.B. Tan, *Polymer,* **42**, 261-272, (2001)
[14] M. Bognitzki, T. Frese, M. Steinhart, A. Greiner, J.H. Wendorff, A. Schaper, M. Hellwig, *Polymer Engineering and Science,* **41**, 982-989, (2001)
[15] H. Schreuder-Gibson, P. Gibson, K. Senecal, M. Sennett, J. Walker, W. Yeomans, D. ZIEGLER, P.P. TSAI, *Journal of Advanced Materials,* **34**, 44-55, (2002)
[16] A. Lendlein, S. Kelch, *Angewandte Chemie International Edition,* **41**, 2034-2057, (2002)
[17] M.S. Dresselhaus, G. Dresselhaus, P.C. Eklund, Science of fullerenes and carbon nanotubes: their properties and applications, Academic press1996.
[18] A. Jorio, G. Dresselhaus, M.S. Dresselhaus, Carbon nanotubes: advanced topics in the synthesis, structure, properties and applications, Springer Science & Business Media2007.
[19] A. Oberlin, M. Endo, T. Koyama, *Journal of crystal growth,* **32**, 335-349, (1976)
[20] R.H. Baughman, A.A. Zakhidov, W.A. de Heer, *Science,* **297**, 787-792, (2002)
[21] C. Lee, X. Wei, J.W. Kysar, J. Hone, *science,* **321**, 385-388, (2008)
[22] A.A. Balandin, S. Ghosh, W. Bao, I. Calizo, D. Teweldebrhan, F. Miao, C.N. Lau, *Nano letters,* **8**, 902-907, (2008)
[23] P. Ajayan, *Chemical reviews,* **99**, 1787-1800, (1999)
[24] Y.A. Kim, K.S. Yang, H. Muramatsu, T. Hayashi, M. Endo, M. Terrones, M.S. Dresselhaus, *Carbon Lett,* **15**, 77-88, (2014)
[25] Y.A. Kim, H. Muramatsu, T. Hayashi, M. Endo, M. Terrones, M.S. Dresselhaus, *Chem Vapor Depos,* **12**, 327-+, (2006)
[26] Y.A. Kim, H. Muramatsu, M. Kojima, T. Hayashi, M. Endo, M. Terrones, M.S. Dresselhaus, *Chem Phys Lett,* **420**, 377-381, (2006)
[27] G.M. do Nascimento, T. Hou, Y.A. Kim, H. Muramatsu, T. Hayashi, M. Endo, N. Akuzawa, M.S. Dresselhaus, *Carbon,* **49**, 3585-3596, (2011)

[28] H. Muramatsu, T. Hayashi, Y.A. Kim, D. Shimamoto, M. Endo, V. Meunier, B.G. Sumpter, M. Terrones, M.S. Dresselhaus, *Small,* **5**, 2678-2682, (2009)
[29] N. Kamaraju, S. Kumar, Y.A. Kim, T. Hayashi, H. Muramatsu, M. Endo, A.K. Sood, *Appl Phys Lett,* **95**, (2009)
[30] T. Hayashi, D. Shimamoto, Y.A. Kim, H. Muramatsu, F. Okino, H. Touhara, T. Shimada, Y. Miyauchi, S. Maruyama, M. Terrones, M.S. Dresselhaus, M. Endo, *Acs Nano,* **2**, 485-488, (2008)
[31] R. Saito, G. Dresselhaus, M.S. Dresselhaus, Physical properties of carbon nanotubes, World Scientific1998.
[32] J.W. Wilder, L.C. Venema, A.G. Rinzler, R.E. Smalley, C. Dekker, *Nature,* **391**, 59-62, (1998)
[33] L. Van Hove, *Physical Review,* **89**, 1189, (1953)
[34] P.G. Collins, P. Avouris, *Scientific american,* **283**, 62-69, (2000)
[35] M. Anantram, F. Leonard, *Reports on Progress in Physics,* **69**, 507, (2006)
[36] T. Ando, *NPG asia materials,* **1**, 17-21, (2009)
[37] M.S. Dresselhaus, G. Dresselhaus, R. Saito, A. Jorio, *Physics reports,* **409**, 47-99, (2005)
[38] N. Minami, S. Kazaoui, R. Jacquemin, H. Yamawaki, K. Aoki, H. Kataura, Y. Achiba, *Synthetic Metals,* **116**, 405-409, (2001)
[39] J. Hone, *Dekker Encyclopedia of Nanoscience and Nanotechnology,* **6**, 603-610, (2004)
[40] R.S. Ruoff, D.C. Lorents, *Carbon,* **33**, 925-930, (1995)
[41] J.-P. Salvetat, G.A.D. Briggs, J.-M. Bonard, R.R. Bacsa, A.J. Kulik, T. Stöckli, N.A. Burnham, L. Forró, *Physical review letters,* **82**, 944, (1999)
[42] H. Kataura, Y. Kumazawa, Y. Maniwa, I. Umezu, S. Suzuki, Y. Ohtsuka, Y. Achiba, *Synthetic metals,* **103**, 2555-2558, (1999)
[43] A. Jorio, R. Saito, J. Hafner, C. Lieber, M. Hunter, T. McClure, G. Dresselhaus, M. Dresselhaus, *Physical Review Letters,* **86**, 1118, (2001)
[44] M. Dresselhaus, G. Dresselhaus, A. Jorio, A. Souza Filho, R. Saito, *Carbon,* **40**, 2043-2061, (2002)
[45] A. Ryabenko, T. Dorofeeva, G. Zvereva, *Carbon,* **42**, 1523-1535, (2004)
[46] D.A. Heller, P.W. Barone, J.P. Swanson, R.M. Mayrhofer, M.S. Strano, *J Phys Chem B,* **108**, 6905-6909, (2004)
[47] M.J. O'Connell, S.M. Bachilo, C.B. Huffman, V.C. Moore, M.S. Strano, E.H. Haroz, K.L. Rialon, P.J. Boul, W.H. Noon, C. Kittrell, J.P. Ma, R.H. Hauge, R.B. Weisman, R.E. Smalley, *Science,* **297**, 593-596, (2002)
[48] S. Lebedkin, F. Hennrich, T. Skipa, M.M. Kappes, *J Phys Chem B,* **107**, 1949-1956, (2003)
[49] Y.H. Miyauchi, S.H. Chiashi, Y. Murakami, Y. Hayashida, S. Maruyama, *Chem Phys Lett,* **387**, 198-203, (2004)
[50] J.H. Waite, *Chemtech,* **17**, 692-697, (1987)
[51] M.E. Yu, J.Y. Hwang, T.J. Deming, *J Am Chem Soc,* **121**, 5825-5826, (1999)
[52] J.H. Waite, *Int J Adhes Adhes,* **7**, 9-14, (1987)
[53] J.H. Waite, *Biol Rev,* **58**, 209-231, (1983)
[54] L.M. Rzepecki, K.M. Hansen, J.H. Waite, *Biol Bull,* **183**, 123-137, (1992)
[55] H.G. Silverman, F.F. Roberto, *Mar Biotechnol,* **9**, 661-681, (2007)
[56] J. Dove, P. Sheridan, *J Am Dent Assoc,* **112**, 879-879, (1986)
[57] D.A. Grande, M.I. Pitman, *B Hosp Joint Dis Ort,* **48**, 140-148, (1988)

[58] B.P. Lee, P.B. Messersmith, J.N. Israelachvili, J.H. Waite, *Annu Rev Mater Res,* **41**, 99-132, (2011)
[59] H. Lee, N.F. Scherer, P.B. Messersmith, *P Natl Acad Sci USA,* **103**, 12999-13003, (2006)
[60] M.E. Yu, T.J. Deming, *Macromolecules,* **31**, 4739-4745, (1998)
[61] D.R. Filpula, S.M. Lee, R.P. Link, S.L. Strausberg, R.L. Strausberg, *Biotechnol Progr,* **6**, 171-177, (1990)
[62] V.V. Papov, T.V. Diamond, K. Biemann, J.H. Waite, *J Biol Chem,* **270**, 20183-20192, (1995)
[63] J.H. Waite, X.X. Qin, *Biochemistry-Us,* **40**, 2887-2893, (2001)
[64] J.H. Waite, *J Biol Chem,* **258**, 2911-2915, (1983)
[65] T.J. Deming, *Curr Opin Chem Biol,* **3**, 100-105, (1999)
[66] M.J. Sever, J.T. Weisser, J. Monahan, S. Srinivasan, J.J. Wilker, *Angew Chem Int Edit,* **43**, 448-450, (2004)
[67] J. Monahan, J.J. Wilker, *Chem Commun,* 1672-1673, (2003)
[68] F. Natalio, R. Andre, S.A. Pihan, M. Humanes, R. Wever, W. Tremel, *J Mater Chem,* **21**, 11923-11929, (2011)
[69] H.J. Cha, D.S. Hwang, S. Lim, *Biotechnol J,* **3**, 631-8, (2008)

Chapter 2

Silicone-Coated Elastomeric Polylactide Nanofiber Filaments: Mechanical Properties and Shape Memory Behaviors

Chapter 2 Silicone-Coated Elastomeric Polylactide Nanofiber Filaments: Mechanical Properties and Shape Memory Behaviors

2.1 Introduction

"Shape-memory material" is a class of stimuli-responsive material, and is has received increasing attention due to their interesting properties and potential applications, such as heat-shrinkable tubing, actuators, sensors, textiles, deployable medical devices and surgical tools, etc. Shape memory metallic alloys are already commercially applied in various industries, but it has many disadvantages such as high cost, low transition temperature and low recovery ability. To overcome these drawbacks, biocompatible and biodegradable shape memory polymers (SMPs) have received increasing attention.[1,2] SMPs are a kind of smart polymeric materials that have the ability to "memorize" a permanent shape, be manipulated to retain or "fix" a temporary shape, and later recover to its original (permanent) shape upon external stimulus such as heat, electricity, or irradiation.[3,4] Thermally induced SMPs are outstanding in all kinds of SMPs. A change in shape induced by T_{trans} (transition temperature), such as T_g (glass transition temperature) and T_m (melting temperature), is called a thermally induced shape memory effect. This kind of polymer can maintain the temporary shape when cooling after deformation at the temperature above its T_{trans}, and return to the permanent shape again after reheating above T_{trans}.[5] There are several typical examples of SMPs, for instance, a polyurethane,[6] main-chain liquid crystalline elastomer (LCE),[7] EPDM ionomers incorporating a range of crystallizable fatty acid salts,[8] and hydrogels with crystallizable alkyl side chains,[9] etc.

Polylactic acid (PLA) is an aliphatic polyester derived by ring-opening polymerization (ROP) from lactic acid, which is prepared from plant starch, and is the most well-studied bioplastics. Most noticeable advantages of PLA are its biocompatibility and biodegradability.[10] And it can be easily processed to produce the thermoplastic products by conventional processes including injection molding, thermoforming and extrusion. In recent years, electrospun nanofibers have been widely used in biomedical areas.[11-13] High surface area-to-volume ratio and high porosity of these nanofibers allow enhanced cell adhesion and proliferation, which hence make them suitable for biomedical applications. For these reasons, electrospun PLA nanofibers can be widely used in various biomedical applications.[14] However, PLA-based nanofibrous bioplastic with shape memory and recyclability have received poor attentions despite these advantages. There are several reasons for this: high stiffness and low toughness of PLA itself as well as poor mechanical properties of electrospun PLA nanofibers.[10] In this paper, we report the silicone-coated elastomeric PLA nanofiber filaments with shape memory and recyclability prepared by a combination of electrospinning,[11-13] twisting,[15,16] and silicone-

coating methods.[17,18] To the best of our knowledge, there have been no studies of elastomeric PLA nanofiber filaments as SMPs. The mechanical properties and shape memory effects of the corresponding silicone-coated elastomeric PLA nanofiber filaments were investigated.

2.2 Experimental

2.2.1 Materials

Poly (L-lactide) (PLLA, M_w = 152,000 g/mol) was purchased from Sigma-Aldrich. Dichloromethane (DCM) and N,N-dimethylformamide (DMF) were purchased from Wako Pure Chemical Industries. Sylgard 184 (hereafter "Sylgard") was commercially available from Dow Corning and consisted of liquid components (a mixture of catalyst Pt and prepolymer dimethylsiloxane with vinyl groups) and curing agent (prepolymer dimethylsiloxane with vinyl groups and Si-H groups).[17,19] All chemicals were of analytical grade and were used without further purification.

2.2.2 Electrospinning

To produce electrospun nanofibers, a high voltage power supply (CPS-60 K022V1, Chunpa EMT Co.) capable of generating voltage up to 80 kV was used as a source of electric field. The PLLA polymer was dissolved in a mixture of DCM and DMF (7:3 by a weight ratio) as solvent, and the concentration of the PLLA solution was 8.0 wt%. The prepared solution was supplied through a 10 ml glass syringe attached to a metallic tip with an inner diameter of 0.6 mm, equipped to micro-syringe pump (KDS-100, Kd scientific Co., USA), and then electrospun onto a rotating metallic collector. The copper wire connected to a positive electrode (anode) was inserted into the polymer solution, and a negative electrode (cathode) was attached to a metallic collector. The applied voltage was 13 kV. The distance between tip to collector was 15 cm. The feed ratio of a syringe pump was controlled by 2.0 ml/h. The averaged fiber diameter and thickness of the resultant PLLA nanofiber mats were 780 ± 40 nm and 28 ± 2 μm, respectively.

2.2.3 Slitting and Dry Twisting Process

To process 2D nonwoven nanofibrous mats into 1D nanofiber filaments, we have previously proposed the general method of slitting and twisting.[15,16] Figure 2.1a and 2.1b present a schematic of electrospinning-slitting-twisting process and a real digital photograph of the twisting machine Q3 (MM-20; Daiei Kagaku Seiki MFG Co., Ltd., Japan), respectively. Briefly, the electrospun PLLA fibrous mats were gently cut into a ribbon-shaped one using a knife. Here, both sides of the nonwoven nanofibrous mats were

sandwiched between the papers to prevent the collapse of the morphologies on cutting. The distance between the chuck was fixed at 15 cm. After the ribbon-shaped nonwoven nanofiber mats were attached to each chuck, and the right side chuck was automatically rewound. This twisting machine had a meter, which could control the number of rotations. The slitting and twisting process may have peculiar processing parameters such as the width of the slit (mm) and the number of twists (twist per meter; T/m). In this study, the width of the slit was controlled to be 3, 5, 7, and 9 mm. The number of twists was 300, 500, 700, and 900 T/m, respectively. But when the number of twists was greater than 900 T/m, a filament was broken.

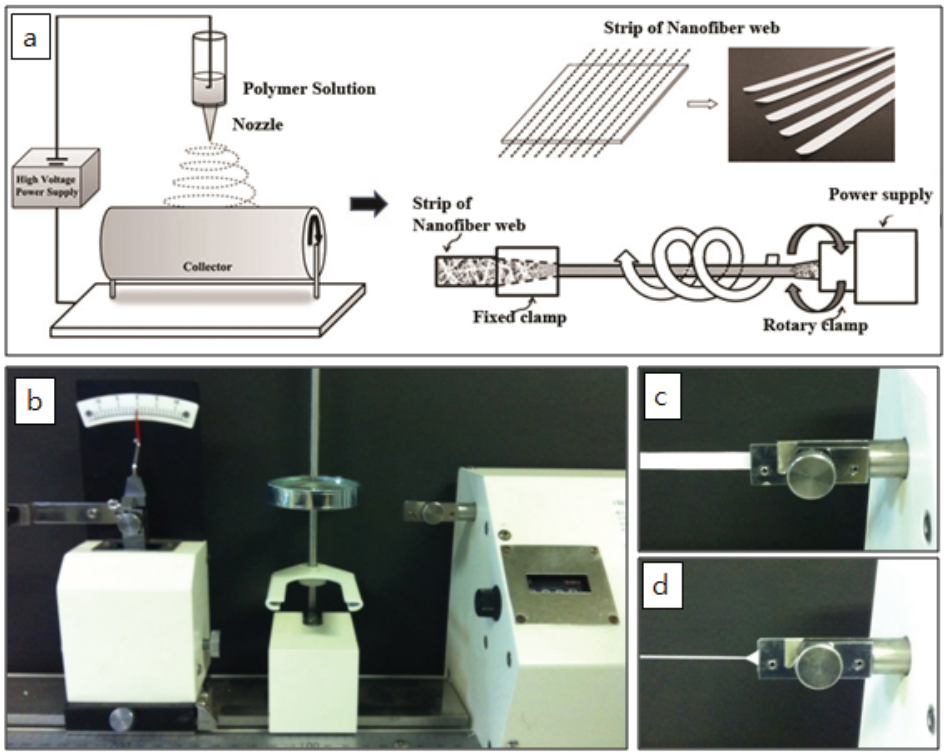

Figure 2.1 (a) Schematic diagram of slitting and twisting process, (b) digital photo of real twisting machine. Digital photo of the nanofiber mat clipped to the right chuck (c) before twisting and (d) after twisting.

2.2.4 Sylgard Coating

Here, the PLLA nanofiber filaments were annealed at 75 ºC for 24h to eliminate a thermal history before Sylgard coating. The annealed PLLA nanofiber filaments were immersed in a two-part mixture of Sylgard 184 (mixing ratio of silicone elastomers base and curing agent = 10:1) and then vacuum was applied for 40 min to ensure complete infiltration of Sylgard 184 into the PLLA nanofiber filaments. The Sylgard 184 was consisted of two parts, silicone elastomer base (a mixture of Pt catalyst and prepolymer dimethylsiloxane with vinyl groups), and curing agent (prepolymer dimethylsiloxane with vinyl groups and Si-H groups). The silicone prepolymers in viscous base part are not hardened itself. The platinum catalyst in the base part switches Si-H group in the curing agent to activated siloxane compound, and this activation causes cross-linking with vinyl end-prepolymers. This reaction is very slow, thus, curing process is maintained over 48h.[19,20] After carefully removing the extra Sylgard 184 resin on the surface, the infiltrated Sylgard/PLLA nanofiber filaments were cured at room temperature for 48 hrs. The fabricated Sylgard/PLLA composites showed an average PLLA weight fraction (measured gravimetrically) of ca. 68.8 % with a small standard deviation of 0.5 %.

2.2.5 Characterization

The morphologies of electrospun PLLA nanofiber mats, filaments, and Sylgard-coated filaments were observed with a scanning electron microscope (SEM; S-3000N, Hitachi, Japan and JSM-6010LA, JEOL, Japan). Mechanical properties of specimens were performed by using a universal testing machine (AG-5000G; Shimazu Co., Japan) under a cross-head speed of 10 mm/min at room temperature. In accordance with ASTM D-638, the nonwoven nanofibers were prepared in the shape of a dumbbell, and then at least five specimens were tested for tensile behavior and the average values were reported. The gauge length of nanofiber filaments was 50 mm. The drawing rate was 10 mm/min at a road cell of 40N. The gauge length of nanofiber filaments was 50 mm. Dynamic mechanical analysis (DMA) was carried out on a DVA-225 (ITK Co. Ltd., Japan), using a tensile resonant mode at a heating rate of 5.0 ºC/min from room temperature to 200 ºC and at a frequency of 1.0 Hz.

The shape memory behavior of the Sylgard-coated elastomeric PLLA nanofiber filaments was evaluated according to the cyclic shape deformation-recovery process: firstly, the straight PLLA nanofiber filament was manipulated to make a permanent coiled shape using a glass rod. Afterwards, the coiled PLLA nanofiber filament was vacuum-annealed at 75 ºC for 24 hrs to remove the thermal history, and used for a visual presentation of the shape recovery process. To measure shape-recovery property, the permanent coiled shape was preheated at 80 ºC for 10 min, deformed to straight shape,

and allowed to cool. The shape-recovery was investigated by placing the shape-fixed (straight) sample on a hot water at 80 ºC.

2.3 Results and Discussion

2.3.1 Mechanical Properties of the PLLA Nanofiber Filaments

Effect of The Width of Nanofiber Mats

To improve the mechanical properties of the nonwoven PLLA nanofibers, a novel method for preparing nanofiber filaments was developed by combining electrospinning with twisting methods. The typical morphologies and mechanical properties of the resultant PLLA nanofiber filaments with different widths of nanofiber mats are shown in Fig. 2.2. As seen in Fig. 2(top), the diameter of nanofiber filaments was increased by increasing the width of the nanofiber mats at a constant number of twists (500 T/m). Moreover, many voids between the nanofibers were largely reduced with increasing the width of nanofiber mats, due to the increased number of fibers constituting the filament by increasing the width of nanofiber mats. Fig. 2.2(a, b; bottom) presents the tensile strength and Young's modulus of the PLLA nanofiber filaments prepared with different widths of nanofiber mats at a constant number of twists (500 T/m). Young's modulus, tensile strength, and elongation at break of the PLLA nanofiber filaments clearly increased with increasing of the width of the nanofiber membranes, which were also well coincided with the previous results.[15,16] The enhanced mechanical properties of the nanofiber filaments could be attributed to the combined effects of the decreased voids and increased internal friction in the nanofiber filaments that resulted from increasing the width of the nanofiber membranes, as confirmed by SEM analysis (Fig. 2.2(top)). The toughness, defined as the energy absorbed by the electrospun nanofiber filaments until breaking, for the PLLA nanofiber filaments was also increased (ca. 425.5%) when the width of the PLLA nanofiber mats increased from 3.0 to 9.0 mm. As a result, it was concluded that the strong interface interactions between the nanofibers were increased by increasing the width of the nanofiber membranes, which improved the load transfer efficiency, resulting in an increase in tensile strength and Young's modulus of the nanofiber filaments.

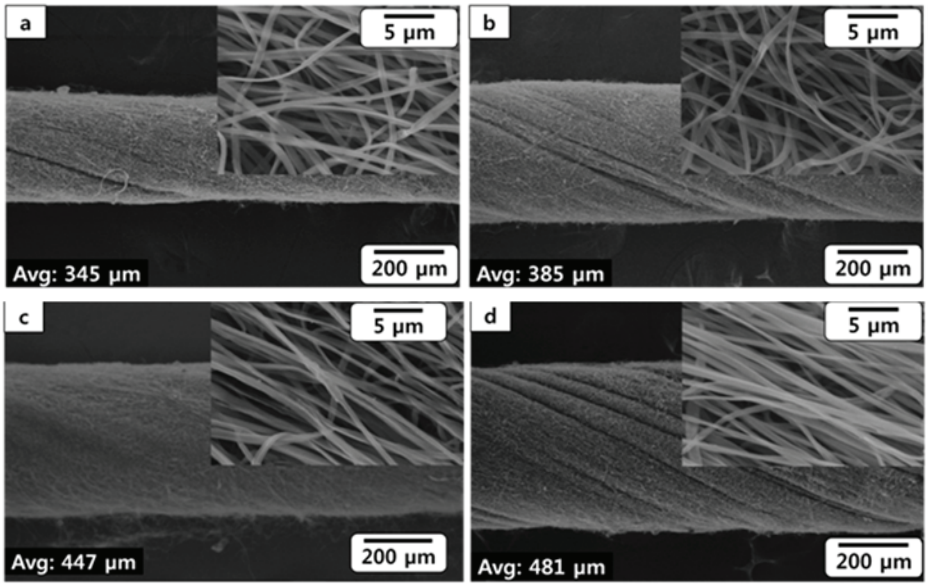

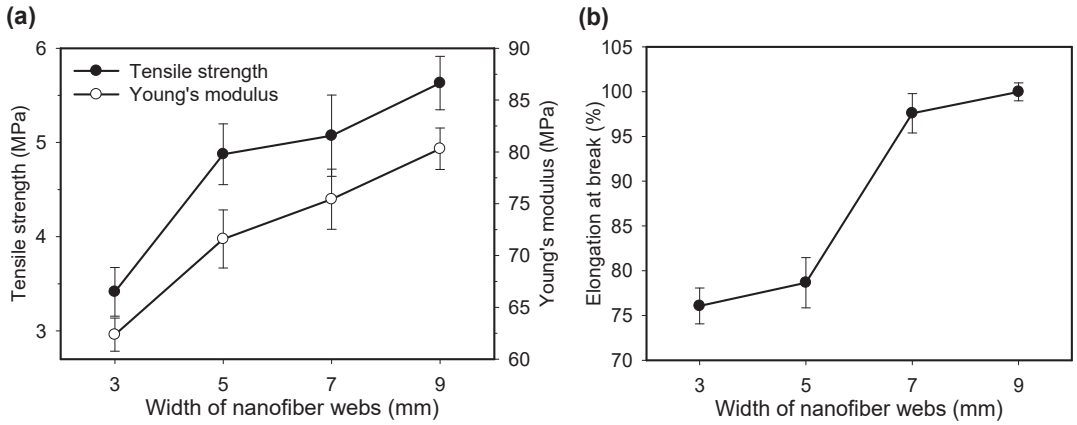

Figure 2.2 (Top) SEM images of PLLA nanofiber filaments with different widths of nanofiber mats: (a) 3 mm, (b) 5 mm, (c) 7 mm, and (d) 9 mm. (Bottom) (a) Tensile strength and Young's modulus, and (b) elongation at break of PLLA nanofiber filaments with different widths of nanofiber mats. The number of twists of all PLLA nanofiber filaments was 500 T/m.

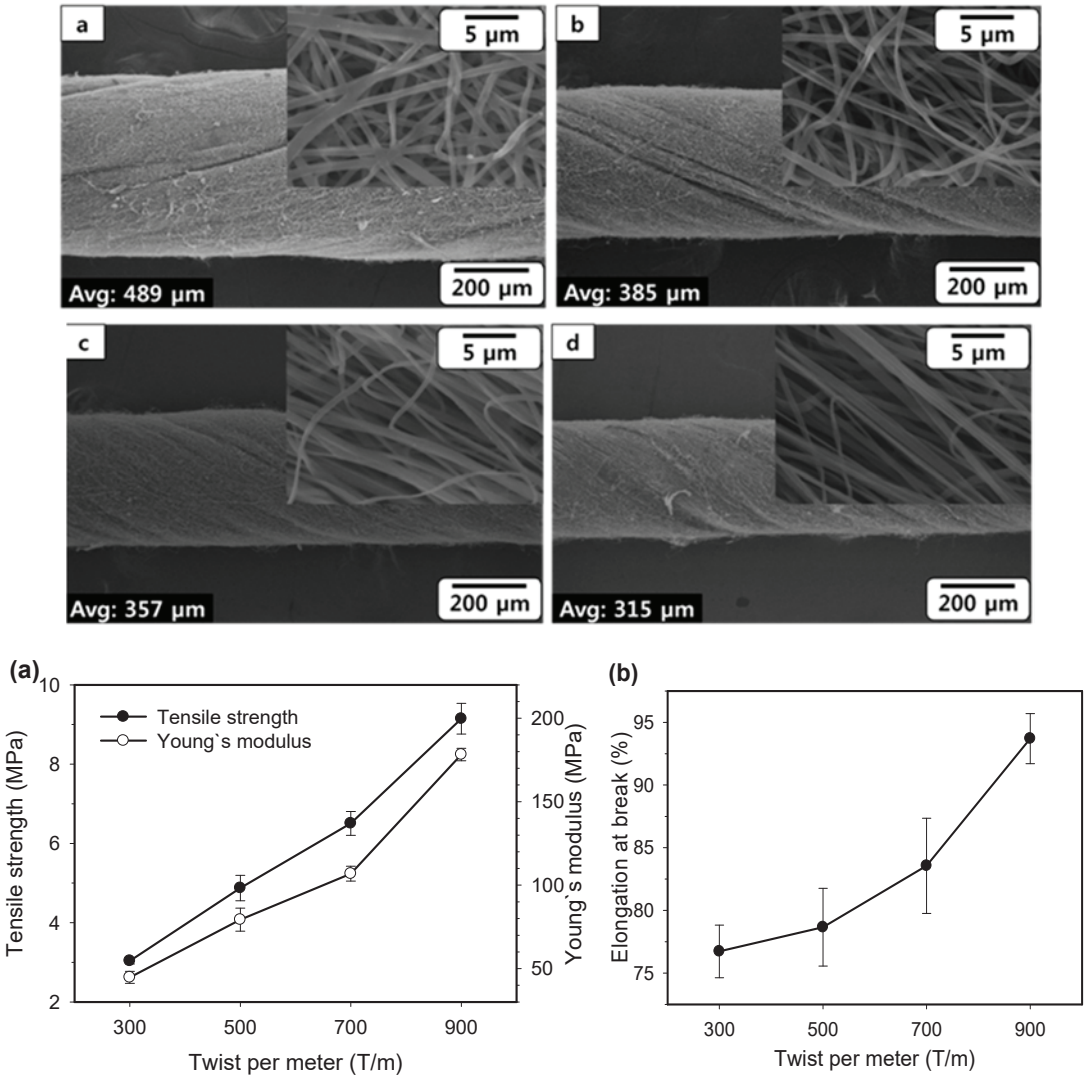

Figure 2.3 (Top) SEM images of PLLA nanofiber filaments with different numbers of twists: (a) 300 T/m, (b) 500 T/m, (c) 700 T/m, and (d) 900 T/m. (Bottom) (a) Tensile strength and Young's modulus and (b) elongation at break of PLLA nanofiber filaments with different numbers of twist. The width of the nanofiber mats of all PLLA nanofiber filaments was 5 mm.

Effect of the Twist Number

Fig. 2.3 presents SEM images and mechanical properties of the PLLA nanofiber filaments prepared with different numbers of twists at a constant width of nanofiber mat (5.0 mm). As expected, the diameter of nanofiber filaments largely decreased with increasing the number of twists (Fig. 2.3(top)). The fiber density also increased, and the fibers were well aligned along the filament long axis. When the number of twists was 900 T/m, the resultant PLLA nanofiber filaments clearly formed a helical structure composed of almost fully stretched individual nanofibers. As the number of twists was further increased to above 900 T/m, the nanofiber filaments were broken. The tensile test was carried out. Similar results were observed (Fig. 2.3(bottom)), indicative of a gradual increase in Young's modulus and tensile strength of PLLA nanofiber filaments with respect to the number of twists. The detailed Young's modulus, tensile strength, elongation at break, and toughness of the PLLA nanofiber filaments were shown in Table 2.1.

Table 2.1 Mechanical properties of PLLA nanofiber filaments with different widths of mats and numbers of twists.

Width of webs (mm)	Number of twist (T/m)	Tensile strength (MPa)	Young's modulus (MPa)	Elongation at break (%)	Toughness (mJ)
3.0	500	3.4 ± 0.3	62.4 ± 1.6	76.1 ± 2.0	15.7
5.0	300	3.0 ± 0.1	44.8 ± 3.8	76.7 ± 2.1	26.7
	500	4.9 ± 0.3	71.6 ± 2.8	78.7 ± 2.8	33.0
	700	6.5 ± 0.3	106.9 ± 5.1	83.6 ± 3.8	35.3
	900	9.1 ± 0.5	178.2 ± 4.2	93.7 ± 2.0	39.0
7.0	500	5.1 ± 0.4	75.4 ± 2.9	97.6 ± 2.2	43.9
9.0	500	5.6 ± 0.3	80.3 ± 2.9	100.0 ± 1.0	66.8

2.3.2 Dynamic Mechanical Analysis of the PLLA Nanofiber Filaments

Fig. 2.4 presents the changes of storage modulus (E′) and loss factor (tan δ) in the PLLA nanofiber filaments with different numbers of twists on heating from the DMA testing. All specimens were annealed by heat treatment at 75 ºC for 24h in order to remove the thermal history before DMA test. The E′ and tan δ of the PLLA nanofiber filament display one distinct transition in the given temperature range, which can be attributed to the glass transition of PLLA. The glass transition temperature was determined from the temperature at which the loss factor is a maximum.[21,22] Moreover, all specimens showed the similar transition temperature range where E′ suddenly decreased and tan δ sharply changed with the increasing temperature. E' was gradually increased by increasing the number of twists. For instance, as increasing the number of twists from 300 T/m to 900 T/m, the E′ at 40 ºC was increased by 339.4%. It indicated that the increase in the number of twists improved the elasticity and strength of the PLLA nanofiber filaments, accompanying a slight increase in T_g. The detailed data were shown in Table 2.2.

Table 2.2 Thermodynamic properties and glass transition temperatures of annealed PLLA nanofiber filaments with different twisting numbers.

Number of twist (T/m)	Storage modulus at 40 ºC (MPa)	Storage modulus at 100 ºC (MPa)	Deviation of storage modulus[a] (MPa)	T_g (ºC)
300	136.9	8.4	128.5	71.2
500	216.3	14.8	202.3	71.8
700	259.3	17.5	241.8	72.3
900	464.7	30.4	434.3	72.5

[a] The difference (dE′) in storage modulus measured by DMA in between the glassy state (at 40 ºC) and the rubber state (at 100 ºC).

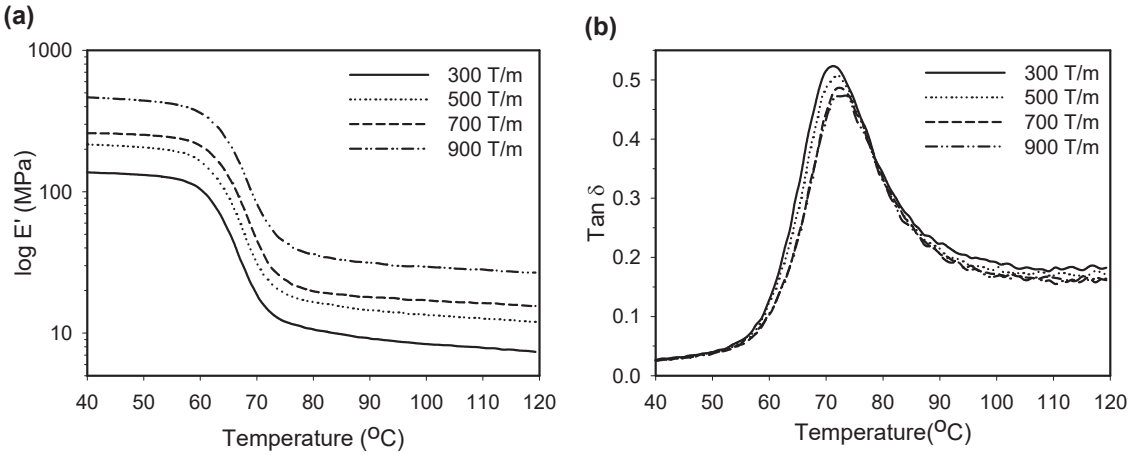

Figure 2.4 Dynamic viscoelastic curve for the PLLA nanofiber filaments with different numbers of twists after annealing: (a) storage modulus and (b) tan δ versus temperature. The width of the nanofiber mats of all PLLA nanofiber filaments was 5 mm.

2.3.3 Sylgard-coated elastomeric PLLA nanofiber filaments

Morphologies

The surface and cross-section morphologies of the Sylgard-coated PLLA nanofiber filaments were studied by SEM. Figures 2.5a, 5b, and 5c present the characteristic morphologies of the electrospun nanofiber mat, nanofiber filament, and Sylgard-coated nanofiber filament, respectively. The surfaces of the Sylgard-coated nanofiber filament clearly proved that the infiltration was complete with all the original voids by Sylgard, while the nanofiber filaments were preserved (Figure 2.5c). The cross-sectioned surface of nanofiber filaments further confirmed the complete infiltration, indicating a biphasic (nanofibers as *a reinforcer* and Sylgard as *a matrix*) bulk morphology (Figure 2.5e). It was therefore expected that Sylgard coating could improve the toughness of the nanofiber filaments as well as the durability of the original shape of the nanofiber filament during shape memory behaviors.

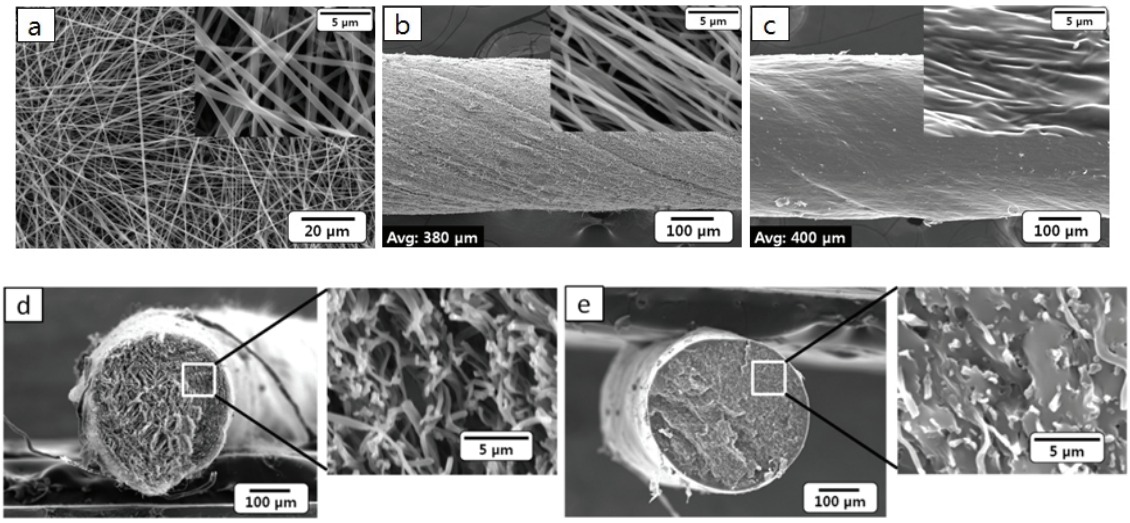

Figure 2.5 SEM images of PLLA nanofiber (a) as-spun mat, (b) filament, (c) Sylgard-coated filament, and cross-section of (d) filament and (e) Sylgard-coated filament. The width of nanofiber mats and the number of twists of filaments were 7 mm and 700 T/m, respectively.

Mechanical Properties

Compared with as-spun PLLA nanofiber filament (~ 6.5 MPa), the tensile strength of annealed PLLA nanofiber filaments was largely increased to 8.3 MPa. But the breaking elongation of the annealed PLLA nanofiber filament (ca. 53.2%) was lower than that of as-spun PLLA nanofiber filament (ca. 83.6%) due to a cold crystallization (Fig. 2.6). As seen in Fig. 2.6, while the tensile strength of the Sylgard-coated nanofiber filament was almost the same as that of the annealed nanofiber filaments without Sylgard-coating, the elongation at breaking and the toughness were remarkably increased by 132.1% and 174.8%, respectively. These results indicated that silicone elastomer was effectively worked as a toughener. As a result, it could be expected that Sylgard coating could lead to less plastic deformation during the shape-deformation/recovery process due to a rubber-toughened plastic system.

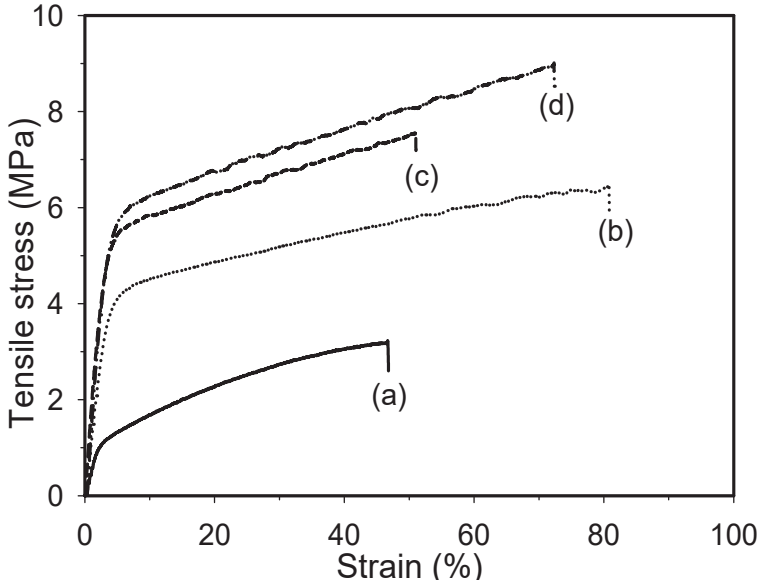

Figure 2.6 Stress-strain curves of PLLA nanofiber (a) as-spun mat, (b) filament, (c) annealed filament and (d) annealed Sylgard-coated nanofiber filament. The width of nanofiber mats and the number of twists of filaments were 5 mm and 700 T/m, respectively.

Dynamic Mechanical Analysis

DMA analysis also confirmed the cold crystallization effect by annealing. Fig. 2.7 presents the changes of storage modulus (E′) and loss factors (tan δ) in *as-spun*, *annealed* and *Sylgard-coated annealed* PLLA nanofiber filaments. As seen in Fig. 2.7a, storage modulus at 40 ºC of as-spun and annealed PLLA nanofiber filaments were 128.4 and 488.7 MPa, respectively. Moreover, the storage modulus in the Sylgard-coated annealed PLLA nanofiber filament exhibited the similar behavior to the annealed PLLA nanofiber filament without Sylgard coating, in accordance with the tensile strength of the Sylgard-coated annealed PLLA nanofiber filament. And interesting change was observed around the melting temperature (T_m ~ 172.3 ºC) of PLLA. The storage modulus of as-spun PLLA nanofiber filament was missing at about 180 ºC, whereas in Sylgard-coated annealed PLLA nanofiber filament, storage modulus was dropped to 0.46 MPa and then maintained without disappearance. These results were occurred since PLLA part was melted while the Sylgard (T_m > 400 ºC) part was remained. Here, the storage modulus of neat Sylgard was about 1.0 MPa.[17] As a result, it was found that Sylgard-coating treatment resulted in a significant role to maintain the shape of PLLA nanofiber filament even above melting temperature.

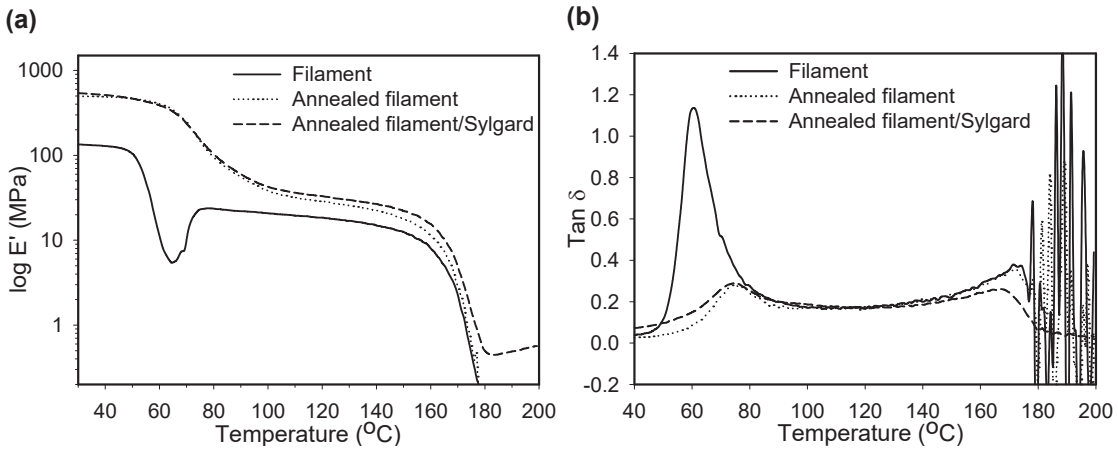

Figure 2.7 Dynamic viscoelastic curve for as-spun, annealed, and Sylgard-coated PLLA nanofiber filaments: (a) storage modulus and (b) tan δ versus temperature. The width of nanofiber mats and the number of twists of filaments were 7 mm and 700 T/m, respectively.

2.3.4 Shape Memory Behaviors of Sylgard-coated Elastomeric PLLA Nanofiber Filaments

Fig. 2.8 presents the schematic illustration of the shape memory cycle of Sylgard-coated PLLA nanofiber filament. The Sylgard-coated PLLA nanofiber filament was first heated to the above shape memory transition temperature (T_{trans}; switching temperature), which was generally T_g or T_m, leading to the material softening (modulus drop). A deformation force was subsequently applied to form the temporary shape (straight shape) from the permanent shape (coil shape). The Sylgard-coated PLLA nanofiber filament was then cooled down under load. Upon unloading, the deformed temporary shape was fixed (Fig. 2.8b). When the Sylgard-coated PLLA nanofiber filament in its temporary shape was re-heated to a shape recovery temperature under a stress free condition, the original (or permanent) shape was recovered (Fig. 2.8c). The switching temperature was 80 °C, which was above T_g of PLLA (cal. 74.3 °C). A series of photographs were taken as a visual presentation of the shape recovery behavior. It showed the higher recovery rate at wider width of slits and larger twisting number (Fig. 2.9a). The recovery rate of the Sylgard-coated PLLA nanofiber filament (slit width: 7mm, twisting number: 700 T/m) was 1.8s. It was 2.7 times higher speed than that of the Sylgard-coated PLLA nanofiber filament (slit width: 3mm, twisting number: 300T/m) (Fig. 2.9b).

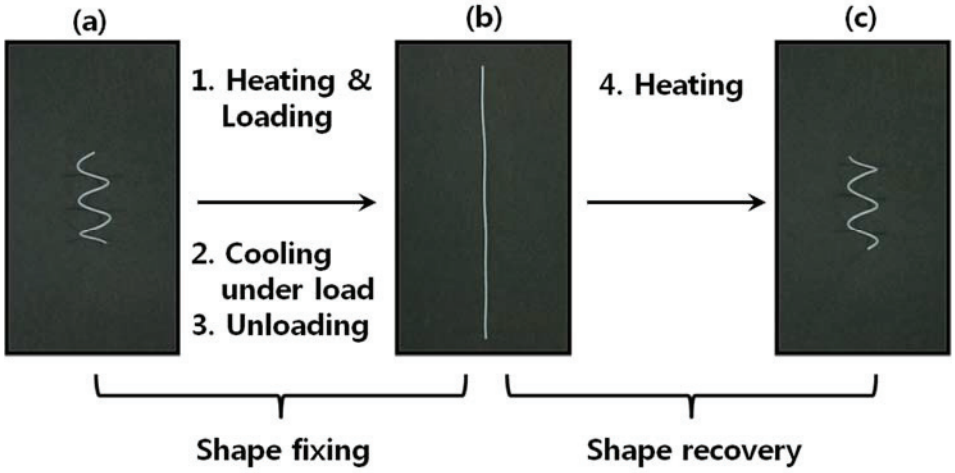

Figure 2.8 Schematic illustration of cyclic shape deformation-recovery process.

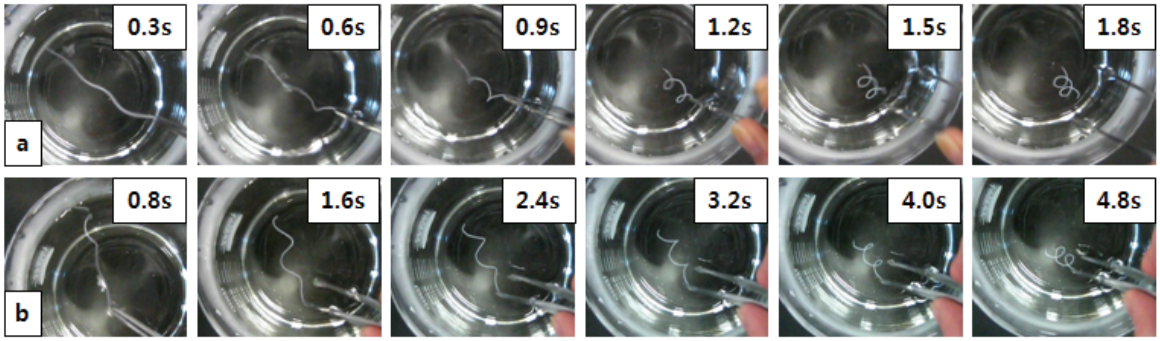

Figure 2.9 Optical images of shape memory Sylgard-coated PLLA filaments with (a) 7 mm and 700 T/m, and (b) 3 mm and 300 T/m.

Fig. 2.10 presents the DMA data of the same samples shown in Fig. 2.9 (the Sylgard-coated PLLA nanofiber filaments; (a) slit width: 7mm, twisting number: 700 T/m, (b) slit width: 3mm, twisting number: 300T/m). Based on a visual presentation of the shape recovery behavior and the DMA analysis, it was expected that the shape-memory effect could be evaluated by probing the difference (dE′) in storage modulus between the glassy state and the rubber state.[5] The difference in the Sylgard-coated PLLA nanofiber filament (slit width: 7mm, twisting number: 700 T/m) was about 442.9 MPa, which was significantly larger than that (~ 103.3 MPa) of the Sylgard-coated PLLA nanofiber filament (slit width: 3mm, twisting number: 300 T/m). It meant that the PLLA nanofiber filament produced by larger twisting number and larger slitting width presented faster recovery rate from temporary shape to permanent shape. Indeed, the shape recovery rate was increased by 2.7 times. As a result, it was concluded that shape-memory effect was enhanced due to an increased dE′ induced by increasing the twisting number as well as the slit width.

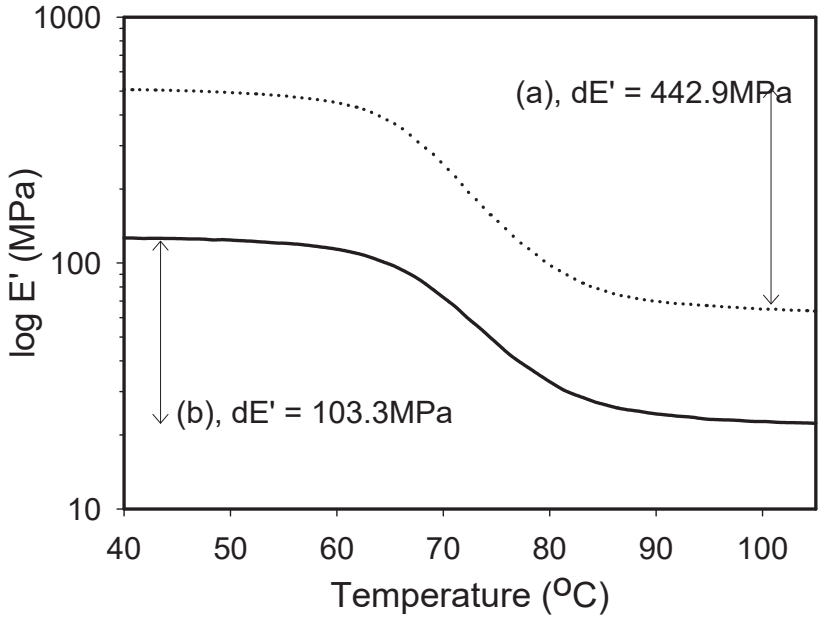

Figure 2.10 Storage modulus (E′) versus temperature of shape memory Sylgard-coated PLLA nanofiber filament with (a) 300 T/m and 3 mm, and (b) 700 T/m and 7 mm.

2.4 Conclusion

The Sylgard-coated PLLA nanofiber filaments were successfully prepared by the combined methods of electrospinning, twisting, and Sylgard-coating. Young's modulus, tensile strength, and elongation at break of the PLLA nanofiber filaments dramatically increased with increasing the width of nanofiber mats as well as twisting number, due to the effects of the decreased voids as well as increased internal friction in the nanofiber filaments. E′ and tan δ of the PLLA nanofiber filaments displayed one distinct transition in the given temperature range, which could be attributed to the glass transition of PLLA. SEM analysis of the cross-sectioned surface of nanofiber filaments also confirmed the complete infiltration of the silicone elastomer, indicating a biphasic (nanofibers as *a reinforcer* and Sylgard as *a matrix*) bulk morphology. Interestingly, it was observed that Sylgard-coating had a significant role to maintain the shape of PLLA nanofiber filaments even above melting temperature and to toughen the PLLA nanofiber filaments. In addition, the higher rate in shape memory behavior was observed at wider width of slits and larger twisting number. The recovery rate of the Sylgard-coated PLLA nanofiber filament (slit width: 7 mm, twisting number: 700 T/m) was 1.8s. It was 2.7 times higher speed than that of the Sylgard-coated PLLA nanofiber filament (slit width: 3mm, twisting number: 300 T/m).

2.5 References

[1] Lendlein and S. Kelch, *Angew. Chem. Int. Ed.*, 2002, **41**, 2034.

[2] T. Tadaki, K. Otsuka and K. Annu. *Rev. Mater. Sci.*, 1988, **18**, 25.

[3] M. Behl , M. Razzaq and A. Lendlein, *Adv. Mater.*, 2010, **22**, 3388.

[4] M. Behl and A. Lendlein, *J. Mater. Chem.*, 2010, **20**, 3335.

[5] X. Zheng, S. Zhou, X. Li and J. Weng, *Biomaterials*, 2006, **27**, 4288.

[6] Z. Haitao, H. Jinlian and C. Shaojun, *J. Mater. Sci.*, 2011, **46**, 3464.

[7] A. Rousseau and P. T. Mather, *J. Am. Chem. Soc.*, 2003, **125**, 15300.

[8] R. A. Weiss, E. Izzo and S. Mandelbaum, *Macromolecules*, 2008, **41**, 2978.

[9] Y. Osada and A. Matsuda, *Nature*, 1995, **376**, 219.

[10] W. Zhang, L. Chen and Y. Zhang, *Polymer*, 2009, **50**, 1311.

[11] H. R. Kim, B. S. Kim and I. S. Kim, *Compos. Sci. Technol.*, 2012, **72**(11), 1233.

[12] S. Kim and I. S. Kim, *Polym. Rev.*, 2011, **51**(3), 235.

[13] Ohsawa, K. H. Lee, B. S. Kim, S. Lee and I. S. Kim, *Polymer*, 2010, **51**, 2007.

[14] V. Fundador, A. Takemura and T. Iwata, *Macromol. Mater. Eng.*, 2010, **295**, 865.

[15] Y. J. Lee, B. S. Kim, H. S. Kim and I. S. Kim, *J. Polym. Res.*, 2012, **19**(2), 1.

[16] R. Nakashima, K. Watanabe, Y. J. Lee, B. S. Kim and I. S. Kim, *Adv. Polym. Technol.*, 2013, **32**, E44.

[17] X. Luo and P. Mather, *Macromolecules*, 2009, **42**, 7251.

[18] M. Handke, B. Handke, A. Kowalewska and W. Jastrzebski, *J. Molecular Structure*, 2009, **254,** 924–926,.

[19] Yang, X. Liu, Y. Jin, Y. Zhu, D. Zeng, X. Jiang and H. Ma, *Biomacromolecules*, 2009, **10**, 3335.

[20] K. Efimenko, W. E. Wallace and J. Genzer, *J. Colloid and Interface Science*, 2002, **254**, 306.

[21] NC. Bleach, SN. Nazhat, KE. Tanner, M. Kellomaki and P. Tormala, *Biomaterials*, 2002, **23**, 1579.

[22] Y. P. Liu, K. Gall, M. L. Dunn and P. M. Cluskey, *Mech. Mater.*, 2004, **36**, 929.

Chapter 3

Annealing effects on mechanical properties and shape memory behaviors of silicone-coated elastomeric polycaprolactone nanofiber filaments

Chapter 3 Annealing effects on mechanical properties and shape memory behaviors of silicone-coated elastomeric polycaprolactone nanofiber filaments

3.1 Introduction

Shape memory polymers (SMPs) are a class of polymers, which can respond to external stimulus by changing their shape and color. Unlike that of shape memory alloys (SMAs) [1], the shape memory effect in SMPs is predominantly an entropic phenomenon [2] and can be induced by various external stimuli, usually heat [3] or in some cases light [4], electric field [5], magnetic field [6], or radiation [7] to return to its original shape. SMPs having good memory, elasticity, and biocompatibility are in demand for biomedical implants [8]. Polycaprolactone (PCL) is a hydrophobic, semicrystalline polymer, which has a low melting point (60 °C). It is one of the earliest synthetic polymers to be commercialized due to high biocompatibility [9]. PCL and its copolymers/composites were demonstrated as very flexible and rubber-like elastic materials useful for tissue engineering. Due to the clear advantages of PCL, there have been several preceding researches about the SMPs employing PCL, for example, composites of PCL/poly(ester acrylate) [7], POSS initiated PCL networks [10], aramid-PCL films [11], melt-spun PCL/polyurethane microfibers [12], PCL/epoxylated natural rubber blend films [13], ethyl cellulose/PCL composite films [14] and Sylgard-coated PCL nanofibers [15], etc.

The wide range of solubility and elasticity of PCL allows it to be electrospun into nanofibers and twisted to form nanofiber filaments. Electrospinning is a versatile technique for producing nanofibers with hierarchically aligned structures [16]. However, to date, there has been no report on the shape memory effect of the Sylgard-coated PCL nanofiber filaments. In this study, the effects of annealing on the mechanical and shape memory properties of the corresponding Sylgard-coated PCL filaments were examined.

3.2 Experimental

3.2.1 Electrospinning

The solution of polycaprolactone (PCL, *Mw*= 65000g/mol, Aldrich) was prepared using DMF at the concentration of 15.0 wt%.[15,17] The solution was supplied through a 10 mL syringe attached to a metallic tip with an inner diameter of 0.6 mm equipped with a micro-syringe pump (KDS-100, Kd scientific Co., USA). The electrospinning was performed using a high voltage power supply (CPS-60 K022V1 Chunpa EMT Co.) at 15 kV at a tip-to-collector distance of 15 cm at about 25^{o}C at relative humidity of 45-50%. The electrospun fibers were collected on a grounded aluminum foil.

3.2.2 Preparation of Nanofiber Filaments

The 1D nanofiber filaments were prepared by slitting and dry twisting similar to our previous reports.[18,19,20] At first the PCL nanofibrous mats were cut into a shape of ribbon using a knife. Secondly, the ends of the non-woven ribbon were attached to two chucks placed at a distance of 15 cm and then twisted using a Q3 (MM-20; Daiei Kagaku Seiki MFG Co., Ltd., Japan) machine. This slit and twist process is controlled by parameters such as slit width (mm) and the number of twists (twist per meter; T/m). In this study, the slit widths were set at 3, 5, 7, and 9 mm, whereas the numbers of twists were 300, 700, 1100, and 1500 T/m.

3.2.3 Sylgard Coating

The resulting PCL nanofiber filaments were coated with Sylgard (Sylgard 184from Dow Corning) by a method similar to our previous reports, and followed by carefully removing the extra Sylgard on the surface, the infiltrated Sylgard/PCL nanofiber filaments were cured at room temperature for 24 h. Afterwards, the Sylgard-coated PCL nanofiber filaments were further annealed at 60^{o}C for 24 h to eliminate the thermal history. The fabricated Sylgard/PCL composites consist of an average PCL weight fraction (measured gravimetrically) of *ca.* 25.6%with a standard deviation of less 0.5%.

3.2.4 Characterization

The as-spun PCL nanofibers, filaments, and Sylgard-coated filaments were platinum sputtered at 20 mA for 120 s and the morphologies were observed under a scanning electron microscope (SEM; S-3000N, Hitachi, Japan and JSM-6010LA, JEOL, Japan). Mechanical properties of the non-woven nanofibrous mats and the filaments were examined using a universal testing machine (AG-5000G; Shimadzu Co., Japan) under a cross-head speed of 10 mm/min at room temperature. The tensile strength of the specimens was tested according to ASTM D638-10 and an average value of five experiments was reported.[21] The drawing rate was 10 mm/min at 40N load cell. A DVA-225 (ITK Co. Ltd., Japan) was used to carry out dynamic mechanical analysis (DMA) in a tensile resonant mode at a frequency of 1.0 Hz where the specimen was heated from room temperature to 100 ^{o}C at the rate of 5.0 ^{o}C/min.

3.3 Results and Discussion

3.3.1 Mechanical Effect of the Width of Mats and the Twisting Number

The SEM morphology of as-spun PCL non-woven mat (Figure 3.1) shows fine fibers having diameters of φ=790±80 nm. The as-spun PCL non-woven mats were twisted into nanofiber filaments. The mechanical properties of the filaments are controlled mainly by two factors, namely the width of the fiber mat and twist number. In order to study the effect of thickness and twist number, the as-spun PCL nanofiber having widths of 3, 5, 7, and 9 mm were twisted at the rate of 700 T/m. The filaments formed a helical structure consisting of fully stretched nanofibers, when the fiber mats are twisted at 1100 T/m (Figure 3.2). A further increase in the twist number caused the breakdown of the filaments. Young′s modulus and elongation at break were increased significantly by increasing the width of the nanofiber mats. Toughness showed a linear relationship with the width of the mats. The toughness of the filaments increased 5 times (ca. 576.4%) from 62.7 to 361.4 mJ when the width of the nanofiber mat increased from 3.0 to 9.0 mm at constant twisting of 700 T/m (Figure 4b and Table 3.1). It was obvious that the enhanced mechanical properties of the filaments were due to the increased number of nanofibers present in the thicker mats which contributed more interfacial interactions between the nanofibers. Accordingly, the effect of the twist number on the mechanical properties was similar to the effect of width of the fiber mat (Figure 2, 4a and Table 3.1).

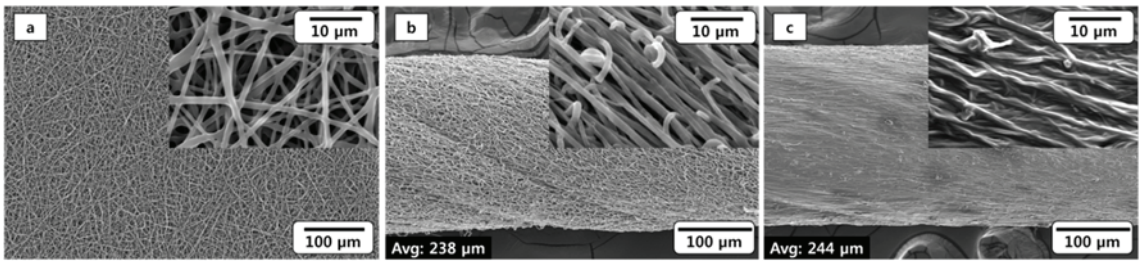

Figure 3.1 SEM images of PCL nanofiber (a) web, (b) filament and (c) Sylgard/filament. The width of webs and the number of twists of filaments were 7mm and 700 T/m.

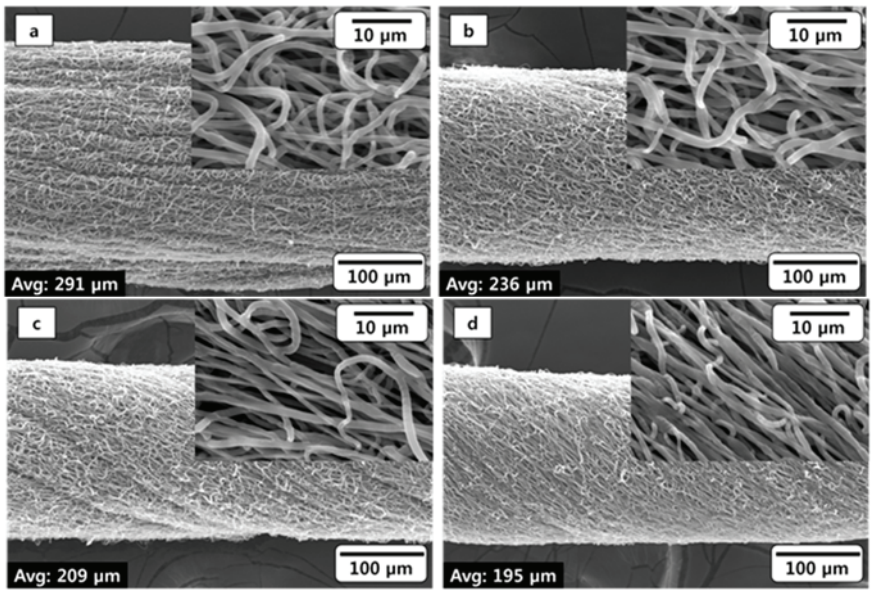

Figure 3.2 SEM images of PCL nanofiber filaments with different numbers of twists: (a) 300 T/m, (b) 700 T/m, (c) 1100 T/m, and (d) 1500 T/m. (width: 5 mm, constant)

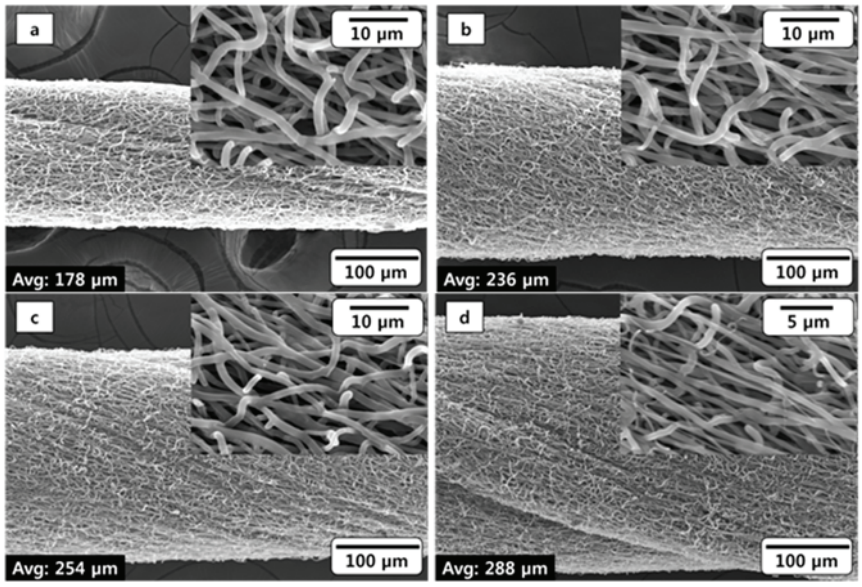

Figure 3.3 SEM images of PCL nanofiber filaments with different widths of nanofiber membranes: (a) 3 mm, (b) 5 mm, (c) 7 mm, and (d) 9 mm. (twists number: 700 T/m, constant)

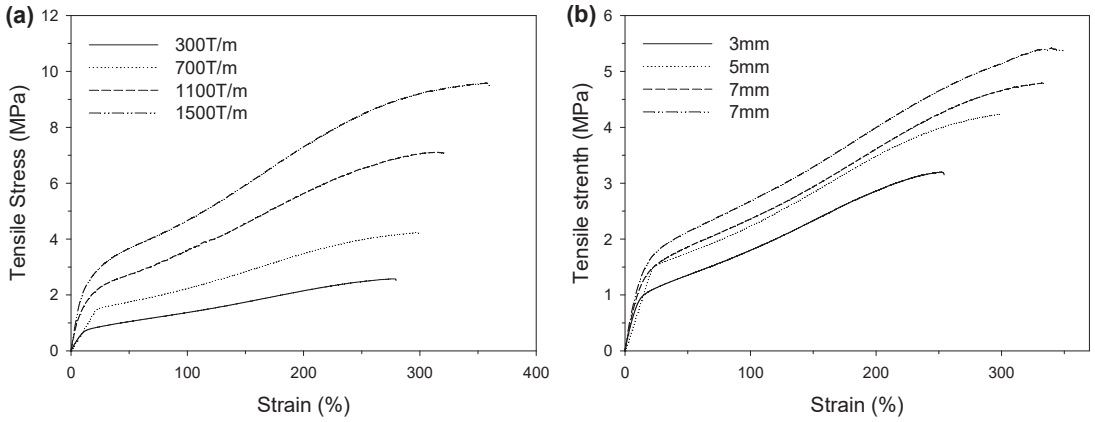

Figure 3.4 Stress-strain curve of PCL nanofiber filaments with different (a) numbers of twists (width: 5mm, constant), and (b) width of nanofiber mats (twisting number: 700T/m, constant).

Table 3.1 Mechanical properties of PCL nanofiber Filament with different numbers of twists, width and process.

Number of twist (T/m)	Width of webs (mm)	Sylgard treatment	Annealing	Tensile strength (MPa)	Young's modulus (MPa)	Elongation at break (%)	Toughness (mJ)
300	5	-	-	2.6 ± 0.4	5.5± 1.2	277.8 ± 7.6	119.9
700	3	-	-	3.2 ± 0.2	6.9 ± 0.7	250.9 ± 6.3	62.7
	5	-	-	4.2 ± 0.7	7.1 ± 1.5	297.6 ± 4.2	138.4
	7	-	-	4.8 ± 1.1	10.1 ± 1.2	332.5 ± 8.9	270.6
	9	-	-	5.4 ± 0.3	11.2 ± 0.8	349.6 ± 5.7	361.4
1100	5	-	-	7.1 ± 0.6	11.5 ± 2.2	315.7 ± 6.3	180.8
1500	5	-	-	9.6 ± 1.3	17.3 ± 1.0	357.7 ± 10.5	202.0
Web	5	-	-	2.2 ± 0.4	4.5 ± 0.9	119.1 ± 3.4	9.4
1100	5	-	-	7.1 ± 0.6	11.5 ± 2.2	315.7 ± 6.3	180.8
1100	5	O	-	8.0 ± 0.3	11.3 ± 1.3	464.8 ± 10.3	323.7
1100	5	O	O	9.1 ± 0.7	15.6 ± 1.7	365.1 ± 8.2	278.6

3.3.2 Dynamic Mechanical Analysis of the Nanofiber Filaments

Dynamic mechanical analysis (DMA) testing also indicated that the increase in the number of twist improved the elasticity and strength of the PCL nanofiber filaments, which is well coincided with the results of mechanical properties (Figure 3.5). E′ was gradually increased by increasing the number of twists.

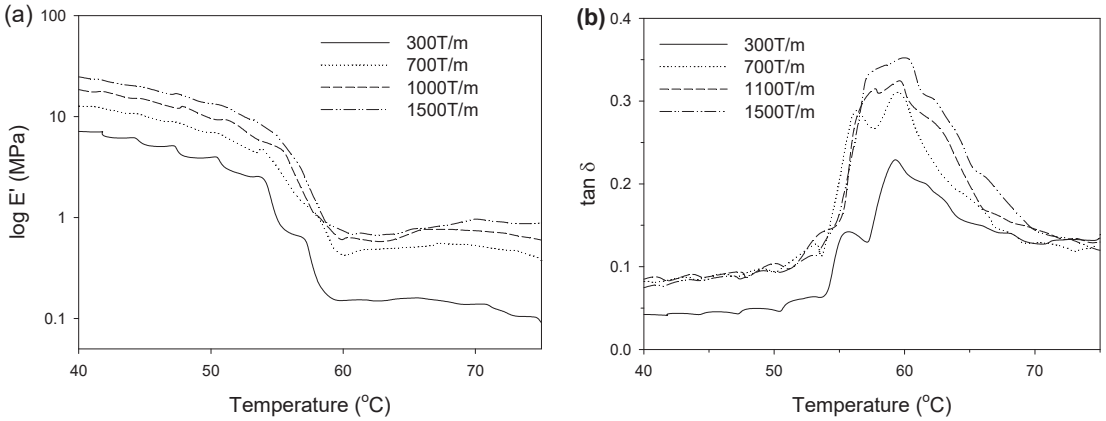

Figure 3.5 Dynamic viscoelastic curve of (a) storage modulus and (b) tan δ versus temperature for the PCL nanofiber filaments with different numbers of twists. The width of the nanofiber mats of all PCL nanofiber filaments was 5 mm.

3.3.3 Sylgard-Coated Elastomeric PCL Nanofiber Filaments

Morphologies and Mechanical Properties

The surface and cross-sectional morphologies of the Sylgard-coated nanofiber filaments revealed complete infiltration of Sylgard into the voids of the filaments with preserving the nanofibers (Figure 3.6). The Sylgard-coating is expected to provide rubber like elasticity to the PCL nanofiber filaments along with improving the toughness and durability. As expected, the Sylgard-coated PCL filaments exhibited greater toughness (~324%) and elongation at break (~465%) than the corresponding PCL nanofiber filaments, while the tensile strength and Young′s modulus did not significantly change. Interestingly, the annealed Sylgard-coated filaments showed a further increase from 11.3 to 15.6 MPa in the Young′s modulus (138%) and correspondingly the decrease in the elongation at break (Table 1). As a result, annealing of the Sylgard-coated PCL nanofiber filament resulted in increased elasticity along with increasing the tensile strength and Young′s modulus.

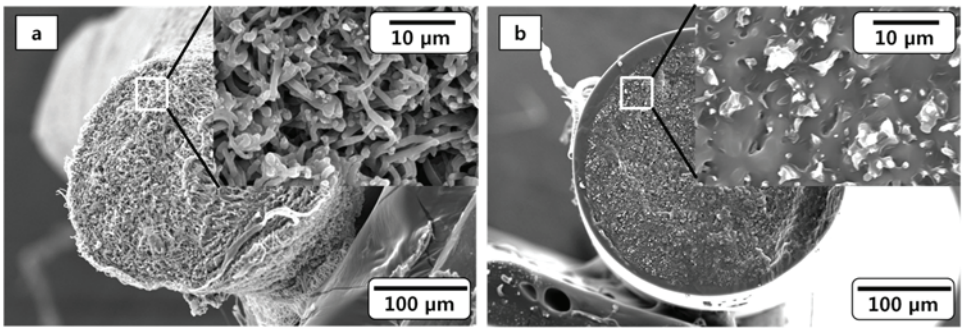

Figure 3.6 SEM images of cross-section of (a) PCL nanofiber filament and (b) Sylgard-coated PCL nanofiber filament. The width of mats and the number of twists were 7 mm and 1100 T/m.

Crystalline Structure by XRD Analysis

The X-ray diffraction patterns of the as-spun PCL nanofiber filament (curve a), Sylgard-coated filament (curve b), and annealed Sylgard-coated filaments (curve c) are shown in Figure 3.7. Sharp diffraction peaks were observed for all the samples at 2θ=22.1° and 23.9°. The former diffraction peak is assigned to the (1 1 1) lattice plane of PCL, whereas the latter one is due to (2 2 0) lattice plane of PCL [22]. Interestingly, the crystal peaks became sharper in annealed Sylgard-coated specimen (Figure 3.7, inset, curve c), suggesting the increased crystallinity of PCL. It was also observed that the melting temperature (Tm) of the Sylgard-coated nanofiber filament is slightly elevated from 60.2 to 61.1 °C after annealing (Table 3.2). These results indicated that annealing could help with increase of the crystallization of PCL [23]. In this system, it was anticipated that the elastomeric matrix (Sylgard 184) would provide rubber elasticity while each nanofiber in Sylgard-coated PCL nanofiber filaments would serve as a reversible "switch phase" for shape fixing (via crystallization) and recovery (via melting) [15].

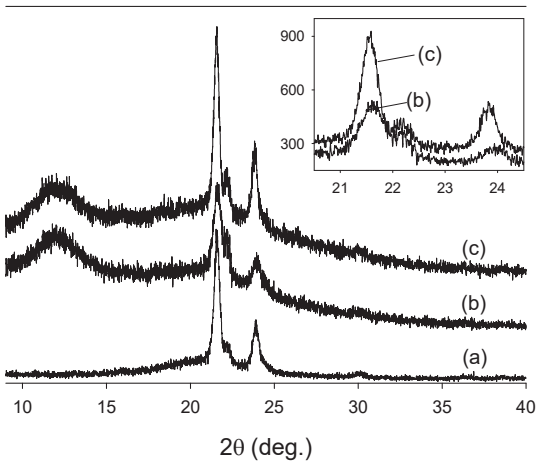

Figure 3.7 WAXD patterns of the PCL nanofiber (a) filament, (b) Sylgard-coated nanofiber filament, and (c) annealed Sylgard-coated nanofiber filament. The width of mats and the number of twists were 7 mm and 1100 T/m, respectively.

Dynamic Mechanical Analysis

The thermodynamic properties of the Sylgard-coated PCL nanofiber filaments were characterized by dynamic mechanical analysis (DMA) (Table 3.2 and Figure 3.8). Prior to DMA, all specimens were annealed at 60 °C for 24 h to remove the thermal history. The storage modulus (E′) was measured at 50 and 70 °C. The E′ of as-spun PCL nanofiber mat showed two distinct transitions in the given temperature (Figure 3.8). The sharp transition around 60 °C was attributed to the melting of PCL. After the Tm, the sample maintained the constant modulus (~0.3 MPa) at the temperature range from 62 to 72 °C, followed by a gradual decrease and then eventually missing in storage modulus. Though, a similar trend was also observed for nanofiber filament, the reason behind the latter transition was not clear and should be further studied. In contrast, the E′ of the Sylgard-coated nanofiber filaments maintained without disappearance because the Sylgard part remained despite the melting of PCL part at about 60 °C. As expected, annealed Sylgard-coated nanofiber filaments exhibited high storage modulus than the corresponding Sylgard-coated PCL nanofiber mat. It is noteworthy that the Tm of the annealed Sylgard-coated PCL nanofiber filament was 61.1 °C whereas the as spun PCL mat had Tm of 59.3 °C. In addition, the storage modulus of as-spun PCL nanofiber filament (10.53 MPa) and Sylgard-coated filament (11.65 MPa) were close to each other at room temperature, whereas, neat Sylgard was reported to have storage modulus about 1.0 MPa, which indicates that the infiltration of the Sylgard does not affect the storage modulus of the Sylgard-coated PCL nanofiber filaments. As a result, it was found that the elastomeric Sylgard gave rubber elasticity to the PCL nanofiber filaments while the fibers would serve as a switchable phase for shape fixing and recovery. Importantly, Sylgard-coating resulted in a significant role to maintain the shape of the PCL nanofiber filament even above Tm.

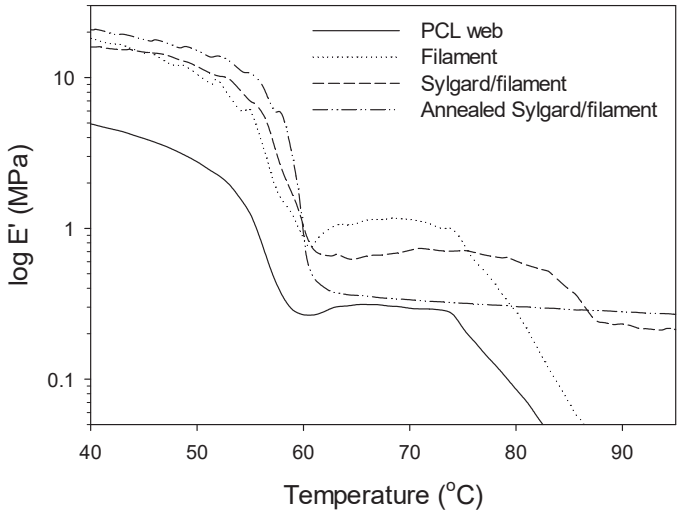

Figure 3.8 Dynamic viscoelastic curves of storage modulus for each process from PCL nanofiber mat to Sylgard-coated nanofiber filament. The width of mats and twisting number of all PCL nanofiber filaments was 7mm and 1100T/m, respectively.

Table 3.2 Mechanical and thermodynamic properties, and glass transition temperatures of PCL nanofiber mat, filament, Sylgard treatment and annealing.

PCL nanofiber	Tensile strength (MPa)	Toughness (mJ)	$E'_{.50℃}$ [a] (MPa)	$E'_{.70℃}$ [b] (MPa)	dE' [c] (MPa)	T_m (℃)
Fiber mat	2.2 ± 0.4	9.4	2.99	0.30	2.690	59.3
Filament	7.1 ± 0.6	180.8	10.53	1.15	9.38	60.4
Sylgard-coated filament	8.0 ± 0.3	323.7	11.65	0.73	10.92	60.2
Sylgard-coated and annealed filament	9.1 ± 0.7	278.6	14.67	0.33	14.34	61.1

[a] Storage modulus at 50℃

[b] Storage modulus at 70℃

[c] Deviation of storage modulus between 50℃ and 70℃

3.3.4 Shape Memory Behaviors of Sylgard-coated Elastomeric PCL Nanofiber Filaments

A series of photographs were taken as a visual representation of the shape recovery behavior (Figure 3.9). To measure shape-recovery property, the permanent coiled shape was preheated at 80 °C for 10 min, deformed to straight shape, and allowed to cool. The shape-recovery was investigated by placing the shape-fixed (straight) sample on a hot water at 80 °C. These filaments showed a desirable shape recovery effect; their recovery ratios were all above 95.0%. The recovery time of the Sylgard-coated PCL nanofiber filament (slit width: 7 mm, twisting number: 1100 T/m) was 1.75 s (Figure 3.9b). Compared to the Sylgard-coated PCL nanofiber filament (slit width: 3 mm, twisting number: 300 T/m, recovery time: 2.25 s), the shape recovery rate was slightly increased 1.3 times.

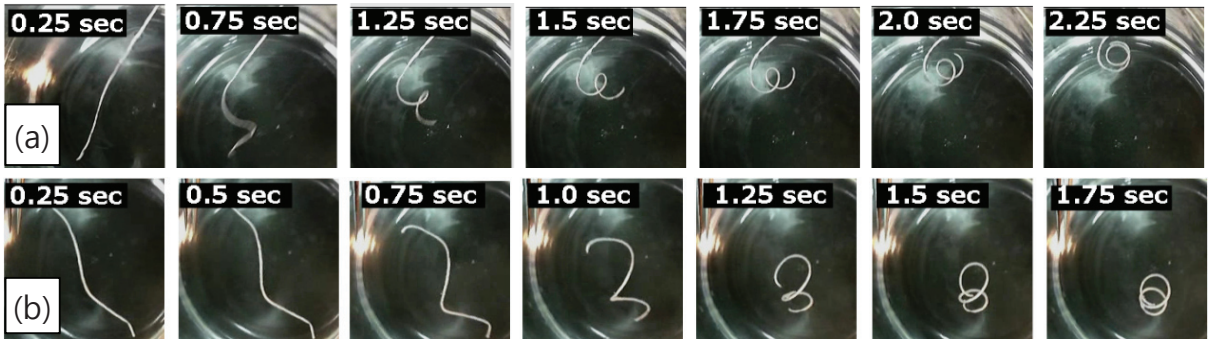

Figure 3.9 Shape memory behavior of the Sylgard-coated PCL nanofiber filaments with (a) 3 mm and 300 T/m, and (b) 7 mm and 1100 T/m, respectively.

3.4 Conclusion

As one kind of smart materials, SMPs play a crucial role, especially for biomedical devices and robotics. In this study, we introduced a new form of SMP, Sylgard-coated PCL nanofiber filaments. Coating of PCL nanofiber filaments with Sylgard has greatly improved the thermomechanical properties of the as-spun PCL nanofiber filament. Annealing of the Sylgard-coated filaments has a significant role in increasing the crystalline levels of PCL, which resulted in the improvement of the toughness and elongation at break. Data analyzed and discussed in this study give insights for broadening the applications of the Sylgard-coated PCL nanofiber filaments such as aerospace industry [24], biomedical devices [8], and smart textiles [25].

3.5 References

[1] Karaca, E. Acar, G.S. Ded, B. Basaran, H. Tobe, R.D. Noebe, et al,. Acta Mater, 61 (2013), pp. 5036–5049

[2] H. Lu, Y. Yao, W.M. Huang, J. Leng, D. Hui, Composites Part B, 62 (2014), pp. 256–261

[3] H. Meng, G. Li, Polymer, 54 (2013), pp. 2199–2221

[4] A. Lendlein, H. Jiang, O. Junger, R. Langer, Nature, 434 (2005), pp. 879–882

[5] Y. Liu, H. Lv, X. Lan, J. Leng, S. Dub, Compos Sci Technol, 69 (2009), pp. 2064–2068

[6] A.M. Schmidt, Macromol Rapid Commun, 27 (2006), pp. 1168–1172

[7] G.M. Zhu, Q.Y. Xu, G.Z. Liang, H.F. Zhou, J Appl Polym Sci, 95 (2005), pp. 634–639

[8] A. Lendlein, R. Langer, Science, 296 (2002), pp. 1673–1676

[9] M.A. Woodruff, D.W. Hutmacher, Prog Polym Sci, 35 (2010), pp. 1217–1256

[10] K.M. Lee, P.T. Knight, T. Chung, P.T. Mather, Macromolecules, 41 (2008), pp. 4730–4738

[11] C. Schuh, K. Schuh, M.C. Lechmann, L. Garnier, A. Kraft, Polymers, 2 (2010), pp. 71–85

[12] H.u. MengQ, J Polym Adv Technol, 19 (2008), pp. 131–136

[13] M. Fejős, K. Molnár, J.J. Karger-Kocsis, Ind Eng Chem, 16 (2010), pp. 256–260

[14] Y. Bai, C. Jiang, Q. Wang, T. Wang, Carbohydr Polym, 96 (2013), pp. 522–527

[15] X. Luo, P.T. Mather, Macromolecules, 42 (2009), pp. 7251–7253

[16] X. Wang, Y. Si, X. Wang, J. Yang, B. Ding, Nanoscale, 5 (2013), pp. 886–889

[17] X. Jingwei, M.W. Stephanie, L. Xiaoran, R.M. Matthew, R. Allison, Shelly ESE, et al, Biomaterials, 30 (2009), pp. 354–362

[18] Y. Lee, B.S. Kim, J.H. Hong, S. Park, H. Kim, I.S. Kim, J Polym Res, 19 (2012), pp. 9774–9779

[19] R. Nakashima, K. Watanabe, Y. Lee, B.S. Kim, I.S. Kim, Adv Polym Technol, 32 (2013), pp. E44–E52

[20] Y.I. Ko, B.S. Kim, J.S. Bae, Y.A. Kim, I.S. Kim, RSC Adv, 3 (2013), pp. 20091–20098

[21] Standard test method for tensile properties of plastics, ASTM D638-10.

[22] C. Yang, Z. Lina, L. Xiaoying, Z. Ning, X. Jian, Macromol Mater Eng, 291 (2006), pp.

[23] D.H. Reneker, A.L. Yarin, Polymer, 49 (2008), pp. 2387–2425

[24] Y. Liu, H. Du, L. Liu, J. Leng, Smart Mater Struct, 23 (2014), pp. 023001–023022

[25] YFCV Yvonne, Text Res J, 77 (2007), pp. 290–300

Chapter 4

Metal Absorbed Biocomposite using Mussel Protein-inspired Double-Walled Carbon Nanotube

4.1 Optical Sensitivity of Mussel Protein-Coated Double-Walled Carbon Nanotube on Iron-DOPA Conjugation Bond

Chapter 4.1 Optical Sensitivity of Mussel Protein-Coated Double-Walled Carbon Nanotube on Iron-DOPA Conjugation Bond

4.1.1 Introduction

Carbon nanotubes (CNTs) have been widely examined in relation to various biomaterial applications, such as drug delivery systems, biocatalysts, biosensors and bone tissue scaffold [1-3] because they exhibited high electrical and thermal conductivity, mechanical strength, and nano-sized diameter.[4-6] Especially, double-walled carbon nanotubes (DWNTs), consisting of two coaxial tubules have several advantages over single- and multi-walled carbon nanotubes (SWNTs and MWNTs) for bio/medical applications due to their unique optical and physicochemical properties. [7, 8] Because of the buffer-like function of the outer tube, optical activity of the inner tube is largely different from that of the outer one with regard to external stimulus. [9-12] Therefore, it is expected that DWNTs are more optically responsive than large-diameter MWNTs or optically suppressed SWNTs, and therefore, DWNTs can function as an optochemical sensor. However, CNTs including DWNTs are insoluble in aqueous solutions and exhibit a low degree of biocompatibility due to their strongly bundled structure as well as the hydrophobic nature of their sidewalls. Thus, in order to expand their excellent physical and chemical properties at a molecular level, various types of biomaterials have been examined for applications as an individual agent for CNTs. [13-15]

In recent years, the mussel-adhesive proteins (MAP) have attracted a great attention because of their great solubility in aqueous phase and strong affinity toward both organic and inorganic surfaces. [16-18] It has been reported that they also show high dispersing and bio-functionalizing ability with regard to DWNTs via the covalent bonds between hydroxyl groups in the outer tubes and amine groups in MAP. [19] Several studies have reported that the *3,4*-dihydroxy-L-phenylalanine (DOPA) moiety in MAP plays a key role in the adhesion of this protein to different surfaces. Because the catechol groups of DOPA form strong coordinative bonding with metal ions, the surface of MAP-coated DWNT suspension could be converted to a 3D-network structure with Fe^{3+} ions.[20,21] Therefore, it is very critical to understand the optochemical singularities of the inner and outer tubes of DWNTs, as well as to verify the physicochemical effects of MAP-metal complexes and the effectiveness of DWNTs as an optochemical sensor.

In the present study, individually dispersed DWNT suspensions were prepared by a homogeneous coating of MAP and their altered optical properties as

a function of the added amount of iron ions was characterized using various optical tools. We found that the formation of iron-DOPA coordinate bonds provided an effective non-radiative channel for the sensitively depressed optical properties of DWNTs.

4.1.2 Experimental

4.1.2.1 Synthesis of the High Purity DWNT Sample

The synthesis of DWNTs was carried out by the catalytic chemical vapour deposition method in a furnace using Mo/Al_2O_3 and Fe/MgO as a conditioning catalyst and nanotube catalyst, respectively. Subsequently, a methane/argon (1:1) mixture was fed into the reactor typically for 10 min at 875°C. The as-grown products were purified via the following steps. First, an oxidation process (500°C, 20 min) was carried out to reduce the chemically active SWNTs. Second, a hydrochloric acid (18%, 100°C, 10 h) treatment was done in order to remove the metal catalysts, followed by air oxidation at 500°C for 10 min in order to remove all carbonaceous impurities. The detailed experimental procedures were described in our previous papers. [7,22]

4.1.2.2 Dispersion of High-Purity DWNTs using MAP in Aqueous Phase

The prepared highly pure DWNTs (1mg) were individually isolated in heavy water (10ml) with the help of MAP (Recombinant mussel adhesive protein, 22.6KDa, Kollodis & Biosciences) (10mg) under strong sonication (VCX 750, Sonics & Materials, 750W) for 1h at 4°C, and subsequent ultracentrifugation (Optima Max-XP, Beckman Coulter, 240000g). The supernatant, containing MAP-dispersed DWNT suspension (70%) and rich in isolated nanotubes, was obtained and characterized in our study. To confirm the dispersibility and chemical effect of MAP, SDBS (1wt%)-dispersed DWNT suspension was also prepared in this study.

4.1.2.3 The Formation of Coordinative Bonds between DOPA and Iron

The iron (III) chloride hexahydrate ($FeCl_3 \cdot 6H_2O$) (270.3 mg) was dissolved in heavy water (10 ml) to produce 100 mM solution. The prepared $FeCl_3$ solution was added to 3ml of individually isolated MAP-DW solution in different amounts (5-100 μl) and subsequent mild sonication (1510, Branson, 5 min) was applied.

4.1.2.4 Characterizations

The optical spectra for DWNT suspensions were obtained using a UV–vis–NIR spectrophotometer (Shimadzu soildspec-3700), photoluminescence maps (NIR-PL system, Shimadzu) and a 785 nm excited Raman system (Renishaw, *inVia* Raman microscope). We also obtained Raman spectra using 532 and 633 nm laser excitations produced by a Kaiser HoloLab5000 system. The chemical bonding and elemental composition of MAP-DW and their metal absorbed composite were characterized by X-ray photoemission spectroscopy (XPS, ESCA-3400, Kratos Analytical) using a MgK_{α} X-ray source at a 10 mA emission current and a 10 kV accelerating voltage. We also obtained the morphology and elemental composition using a field emission scanning electron microscope (FE-SEM) coupled with energy dispersive X-ray spectroscopy (EDS) (JSM-7000f, JEOL). Finally, we have used a high-resolution TEM (JEM-2010FEF, JEOL) to see the dispersion state of the nanotubes as well as the coated mussel protein on the sidewalls of the DWNTs.

4.1.3 Results and Discussion

4.1.3.1 Preparation of Individually Dispersed MAP-DW Suspension

A high purity DWNTs with a large bundle size were synthesized using the chemical vapor deposition method (Figure 4.1.1 (a, b)). [5,22] Then, we examined the dispersing ability of the MAP with regard to the bundled DWNTs. [19] By subjecting the bundled DWNTs with MAP in an aqueous solution under strong sonication, an opaque suspension (Left suspension in Figure 4.1.1 (d)) is obtained. In the following ultracentrifugation process, we obtained a semi-transparent supernatant containing the individually dispersed DWNTs via the precipitation of the bundled DWNTs (Middle suspension in Figure 4.1.1 (d)). By adding $FeCl_3$ solution (10 mM) to the supernatant, we obtained a yellowish DWNT suspension (Right suspension in Figure 4.1.1 (d)). This solution was still semi-transparent and there was no precipitate.

This solution was still semi-transparent and there was no precipitate. Then, the dispersion state of DWNTs in an aqueous solution was evaluated optically using Raman/fluorescence spectra with 785nm laser line and UV-Vis-NIR absorption spectra for both supernatant and remnant (Figure 4.1.2 (a, c)). We observed well-resolved strong luminescence peaks (Figure 4.1.2 (a)) and sharp absorption peaks for the supernatant (Figure 4.1.2 (c)). In contrast, relatively depressed luminescence and absorption peaks in the remnant can be explained by strong coupling interactions between adjacent nanotubes. [23] Such optical results allowed us to conclude that DWNTs were individually dispersed in an aqueous solution with the help of MAP. [22] A typical TEM images showed an individual DWNT coated with amorphous-like MAP (Figure 4.1.2 (d)).

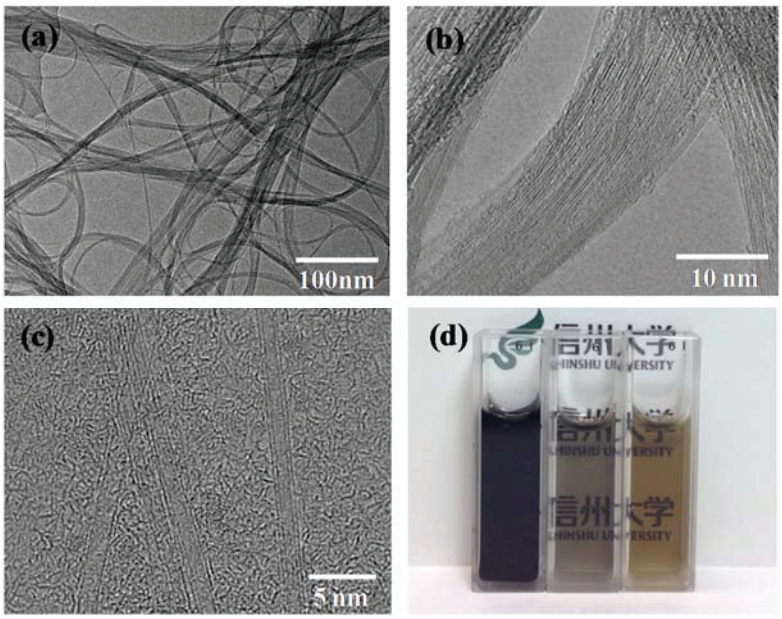

Figure 4.1.1 TEM images of (a, b) pristine bundled DWNTs at different magnifications and (c) $FeCl_3$ solution added-MAP-dispersed DWNT supernatant. (d) The sonicated opaque DWNT suspension (left), the following ultra-centrifuged semi-transparent MAP-dispersed DWNT supernatant (middle), and after adding 100 µl of $FeCl_3$ solution (100 mM) to the MAP-dispersed DWNT supernatant.

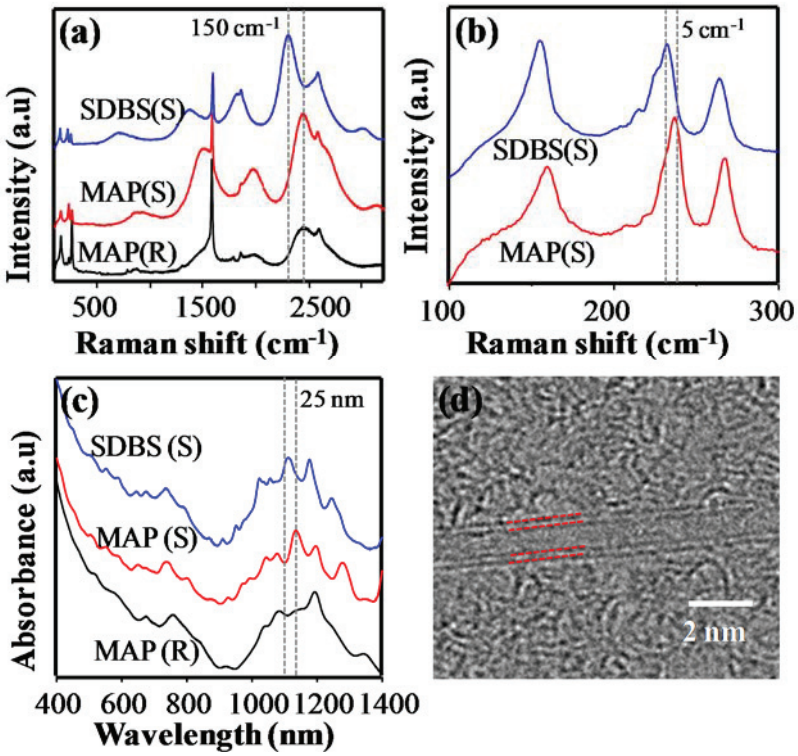

Figure 4.1.2 Wide-range Raman/fluorescence spectra, (b) their corresponding radial breathing modes taken with laser excitation of 785 nm, and (c) UV-Vis-NIR absorption spectra for SDBS-dispersed DWNT supernatant (S), MAP-dispersed DWNT supernatant (S) and MAP-dispersed DWNT remnant (R), respectively, and (d) high-resolution TEM image of MAP-coated individual DWNT.

Then the coating effects of MAP on the optical properties of the DWNTs were analysed in detail. We observed a red shift both in the luminescent peaks and in the UV-Vis-NIR absorption peaks of the supernatant as compared to that of the SDBS-dispersed DWNT suspension (Figure 4.1.2 (a, c)). The shifted energy gap (ΔE_{ii}) are summarized in Table 4.1.1 and 2. [24] It is assumed that environmental dielectric screening effects contribute to a red shift in the optical spectra. [25,26] Moreover, since strong electron-donating groups, such as hydroxyl, carboxyl and amine groups were present in the MAP structure, [17,27] the electron density of DWNTs in the MAP-dispersed nanotube solution was expected to be higher than that of the SDBS-dispersed nanotube suspension. Thus, we believe that excitons could be easily excited due to the presence of electron donating groups, thereby resulting in the redshift of both absorption and luminescent emission through a decrease in the energy-gap. [28] Both environmental dielectric screening effects and electron donating groups in the MAP structure induced a change in the energy-gap of the DWNTs, thus resulting in a modification of the resonance window when the 785 nm laser line was used. [28]

Table 4.1.1 Structures and first van Hove optical transitions for semiconducting SDBS- and MAP-dispersed DWNTs from Raman/fluorescence spectra.

Assignment (n,m)	SDBS-DWNT			MAP-DWNT			Δλ [c] (nm)	ΔE [d] (eV)
	ω (cm-1)	λ (nm)	E (eV) [a]	ω (cm-1)	λ (nm)	E (eV) [b]		
(7,5)	2995.4	1026.3	1.209	3142.4	1042.1	1.191	15.7	-0.018
(6,5)	2529.7	979.5	1.267	2681.1	994.3	1.248	14.7	-0.019
(8,3)	2289.1	957.0	1.297	2460.0	972.9	1.275	15.9	-0.021
(9,1)	1810.2	915.0	1.356	1991.2	930.4	1.334	15.4	-0.022
(6,4)	1368.4	879.5	1.411	1513.8	890.9	1.393	11.4	-0.018
(5,4)	716.3	831.8	1.492	902.8	844.9	1.469	13.1	-0.023

[a,b] Band-gap was calculated from absorption wavelength by the following equations: $E=hc/\lambda$, (E: band gap, h : speed of light in vacuum, c : Planck's constant, and λ : wavelength);
[c] The shifts of absorption wavelength ($\Delta\lambda_{ii}=\lambda_{ii}^{\text{MAP-DWNT}}-\lambda_{ii}^{\text{SDBS-DWNT}}$) are calculated;
[d] The energy differences ($\Delta E_{ii}=E_{ii}^{b}-E_{ii}^{a}$) are calculated.

Table 4.1.2 Structures and First and Second van Hove Optical Transitions a for Semiconducting SDBS- and MAP-dispersed DWNTs from UV-Vis-NIR spectra.

van Hove transitions	SDBS-DWNT		MAP-DWNT		$\Delta\lambda$ [c] (nm)	ΔE_{ii} [d] (eV)	d_t [e] (nm)	Chirality (n,m)
	λ_{ii} (nm)	E_{ii} (eV) [a]	λ_{ii} (nm)	E_{ii} (eV) [b]				
Semi-conducting (E_{11})	1248	0.994	1281	0.969	32	-0.026	1.050	(10,5)
	1178	1.053	1198	1.036	20	-0.018	0.995	(12,1)
	1114	1.114	1137	1.091	25	-0.023	0.916	(9,4)
	1058	1.173	1077	1.152	19	-0.021	0.884	(10,2)
	1026	1.209	1045	1.187	19	-0.022	0.829	(7,5)
	954	1.301	974	1.274	20	-0.027	0.782	(8,3)
	913	1.359	931	1.333	18	-0.026	0.757	(6,5)
Semi-conducting (E_{22})	872	1.423	884	1.404	12	-0.019	1.111	(14,0)
							1.186	(11,6)
							1.120	(13,2)
							1.145	(12,4)
	801	1.549	807	1.538	6	-0.012	0.995	(12,1)
	794	1.563	803	1.545	9	-0.018	1.111	(10,6)
	734	1.690	739	1.679	5	-0.011	1.032	(8,7)
							0.966	(8,6)
	675	1.838	677	1.833	2	-0.005	1.041	(12,2)
	645	1.924	656	1.891	11	-0.032	0.895	(7,5)
							0.829	(7,6)
	589	2.107	594	2.089	5	-0.018	0.840	(8,4)

[a,b] Band-gap was calculated from absorption wavelength

[c] The shifts of absorption wavelength ($\Delta E_{ii}=\lambda_{ii}^{\text{MAP-DWNT}}-\lambda_{ii}^{\text{SDBS-DWNT}}$) are calculated.

[d] The energy differences ($\Delta E_{ii}=E_{ii}^{b}-E_{ii}^{a}$) are calculated.

[e] The diameters for SWNTs are referred to reference.

4.1.3.2 Raman/fluorescence Spectra of M-DW with Fe^{3+} Complex

The effect of adding $FeCl_3$ solution (100 µl) to MAP-dispersed DWNT supernatant was evaluated by Raman/fluorescence spectra using 785 nm laser line (Figure 4.1.3 (a)). The Raman spectra of the pristine DWNT exhibited a strong G-band (E_{2g2} mode) at 1590 cm^{-1}, several radial breathing modes (RBMs) below 500 cm^{-1} and G′-band at around 2588 cm^{-1}.[29] The sonicated DWNT suspension shows a weak luminescence peak around 2400cm^{-1}. The supernatant containing the individually dispersed DWNTs showed the intensified luminescence peaks compared to the intensity of the G-band. However, after adding 100µl of $FeCl_3$ solution to the supernatant with subsequent mild sonication, these strong emissions were completely suppressed. The formation of coordinate bonds between the

DOPA (right scheme in Figure 4) in MAP and Fe^{3+} ion, [30] provided non-radiative channels, which led to quenching of luminescence of the semiconducting inner tubes, which is similar to entrapment effect of metallic tubes in bundled tubes. In other words, several DOPA groups in the MAP molecule [20, 21] allowed DWNTs to attain a 3D-network structure by DOPA-Fe^{3+} bonding. Therefore, the DWNTs lost their optical singularities due to charge transfer through the DOPA-Fe^{3+} linkage. This charge transfer effect also could be confirmed by observations of Raman/fluorescence spectra with laser excitations of 633 and 532 nm. As shown in Figure 4.1.4, even though the G-band of the DWNTs in the MAP-dispersed DWNT suspension had a relatively low intensity due to strong emission from MAP, the addition of $FeCl_3$ solution induced a marked increase in the relative intensity of the G-band with regard to the emission of MAP. This phenomenon indicated that a non-radiative channel was established by the formation of electronically active DOPA-Fe^{3+} linkages. [31, 32]

The radial breathing modes (RBMs) of CNTs have been used to evaluate their chirality and diameter as well as their dispersion state. [33-38] Strano *et al*. revealed that the RBM intensity at 267 cm^{-1} decreased and the RBM intensity at 234 cm^{-1} increased when SWNTs were isolated completely with sodium dodecyl sulfonate (SDS).[33, 38] For the MAP-dispersed DWNT supernatant, the RBM peaks from the semiconducting inner tube exhibited higher intensity at 237 cm^{-1} and relatively lower intensity at 268 cm^{-1} than those of the sonicated or bundled DWNTs (Figure 4.1.3 (b)). However, the addition of $FeCl_3$ solution caused a significant decrease in the RBM intensity at 237 cm^{-1} and an increase in the RBM intensity at 268 cm^{-1} (Figure 4.1.3 (b)). This result indicated that the electronic structure was largely modified by the formation of strong DOPA-Fe^{3+} bonds between the individually isolated DWNTs as the 3D-network structure, so that the resonance states of S inner tubes shifted like the bundled DWNTs. In contrast to the UV-Vis-NIR and Raman results, TEM image (Figure 4.1.1 (c)) showed individually isolated DWNTs state, even after the addition of $FeCl_3$ to the MAP-dispersed DWNT suspension. This result indicated that the individually isolated phase of DWNTs that enclosed by MAP-Fe^{3+} complex was retained, but non-radiative channels were created through the formation of MAP-Fe^{3+} bonds.

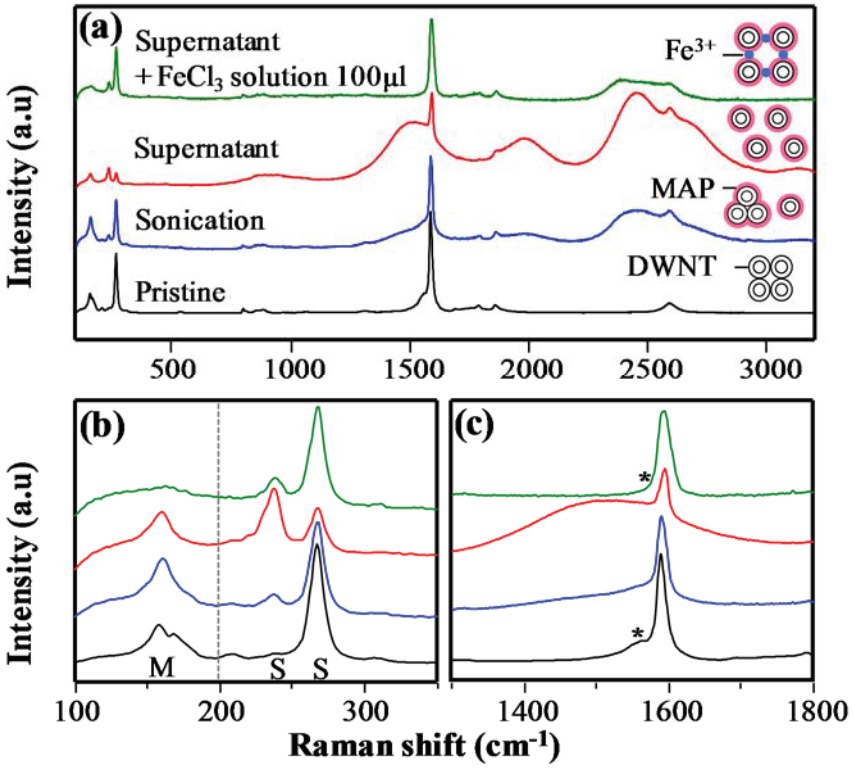

Figure 4.1.3 (a) Raman/fluorescence spectra taken with laser excitation of 785 nm for pristine DWNTs and MAP-dispersed DWNT suspensions at different dispersion states (sonicated, supernatant) and the $FeCl_3$ solution added-MAP dispersed DWNT supernatant, and their corresponding (b) radial breathing mode (where S indicates semiconducting and M indicates metallic tubes), and (c) G-band (asterisk indicates the BWF line associated with metallic outer tubes).

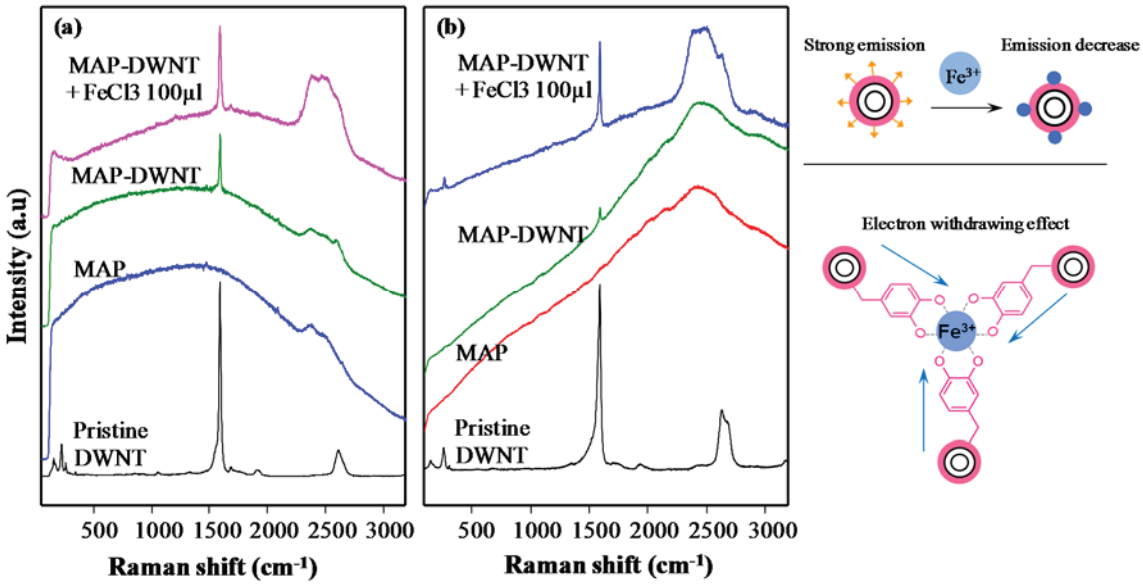

Figure 4.1.4 Raman/fluorescence spectra taken with laser excitation wavelengths of (a) 633 nm and (b) 532 nm for pristine DWNTs and MAP-dispersed DWNT solutions at different dispersion states (remnant (blue), supernatant (green), and after adding $FeCl_3$ solution (pink)).

When looking at the RBM peaks of the metallic outer tube, the intensity at 160 cm^{-1} was maintained in the MAP-dispersed DWNT supernatant (Figure 4.1.3 (b)). However, the addition of $FeCl_3$ solution caused the RBM peak at 160 cm^{-1} to be almost suppressed because the outer tubes were in direct contact with the MAP-Fe^{3+} complex. This indicated that circumferentially generated and concentrated stress was induced by surface stiffening of the sidewall which suppressed RBM vibrations in the radial direction. [39] Moreover, when looking at the G-band (Figure 4.1.3 (c)), the broad and asymmetric Breit-Wigner-Fano (BWF) line [40] of the pristine DWNT sample was strongly suppressed in the Fe-MAP-DWNT suspension. The metallic outer tube could not resonance with 785 nm excitation and their corresponding metallic shoulder of G^--band was thus reduced, which resulted in the disappearance of the RBM peak (160 cm^{-1}) in the iron-MAP-DWNT suspension. These results supported the protective function of the outer tubes in DWNTs.[41, 42]

4.1.3.3 Elemental and Bonding Composition of FeMAP-DW Composite

X-ray photoelectron spectroscopy measurement was also carried out on pristine, MAP-DWNT, and Fe-MAP-DWNT samples in order to determine the relative quantity of the functional groups attached to the outer walls of the DWNTs (Figure 4.1.5). For the pristine DWNT sample, there was an intense peak at ca. 284.7 eV from the sp^2-hybridized carbon atoms and also a broad peak at 285.3 eV due to the sp^3-hybridized carbon atoms (Figure 4.1.5 (a)). [43, 44] For MAP-DWNTs, the prominently present sp^3-hybridized peaks (*e.g.*, C-N, C=O, C=O-N and O-C=O carbon atoms) came from the functional groups of MAP, [19] indicating that the outer tubes of DWNTs had been well coated by MAP. Some weak peaks (Figure 4.1.5 (b)) came from O1s of the hydroxyl- and carboxyl-groups on defects and edges of the pristine DWNT sample; on the other hand, peaks with large intensities, such as from O-C=O, O-C and O=C at 534.4, 533.3, and 532.2 eV, respectively, were closely associated with MAP.

When 30µl of $FeCl_3$ solution was added to the MAP-dispersed DWNT supernatant, the O1s peak shifted to lower energy (ca. 0.4 eV) due to a decrease in the O-C signal, and a new peak appeared at 531.6 eV, which was associated with the O-Fe coordinative bonding. [45] From Table 4.1.3, it is interesting to note that the ratio of the O-Fe bond increased by ca. 16.40 % when the O-C bond was reduced ca. 15.8 % even though the atomic ratio of oxygen had not changed. Such result signified a transition from the O-C to O-Fe bond when the $FeCl_3$ solution was added to the supernatant, without any significant change in the N1s (Figure 4.1.6) and C1s XPS spectra (Figure 5). Therefore,

we are able to say that the hydroxyl groups of the DOPA created coordinative bonds with Fe^{3+} ion. In addition, the presence of Fe^{3+} ions was verified by the peaks at 710.8 eV and 724.2 eV associated with *2p 3/2* and *2p 1/2*, and their charge-transfer satellite peaks at 714.4 eV and 727.6 eV, respectively. [46] Furthermore, as shown in Table 4.1.3, the atomic ratio of Fe^{3+} ions did not change significantly (ca. 0.5%) on increasing the addition amount of $FeCl_3$ from 30µl to 50µl. Thus, this result indicated that the DOPA components within the MAP were saturated in this range because all the hydroxyl groups available to bond with Fe^{3+} had been fully utilized.

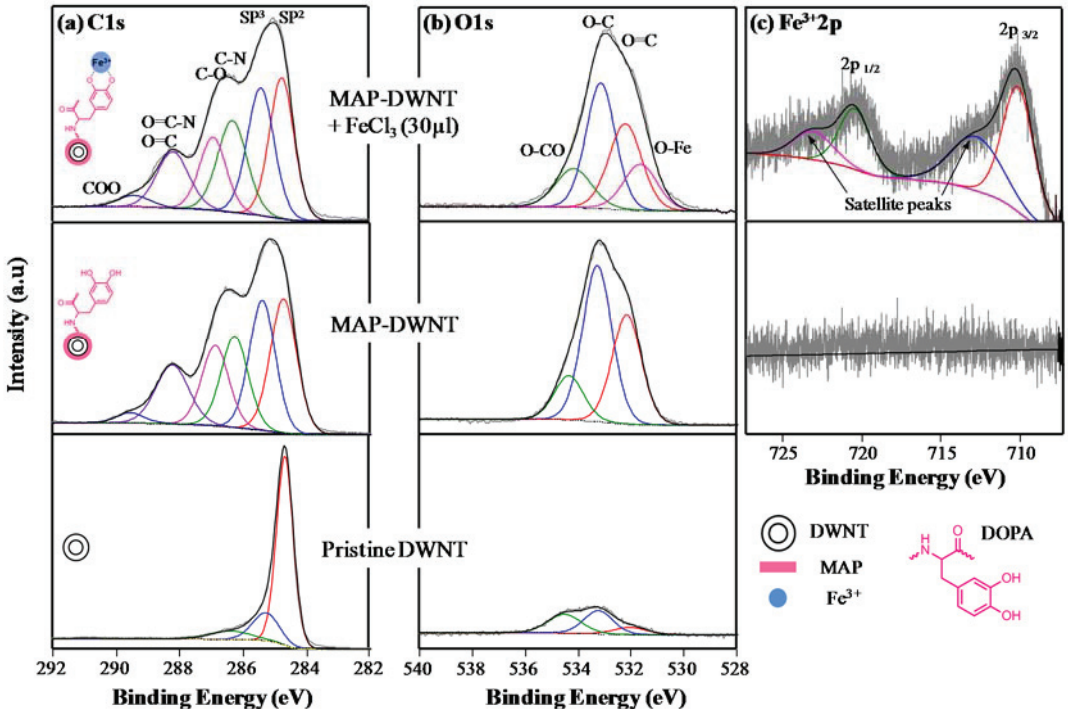

Figure 4.1.5 The (a) C1s, (b) O1s, and (c) Fe^{3+}2p XPS spectra of pristine DWNTs, MAP-coated DWNT and $FeCl_3$ solution added-MAP dispersed DWNT complexes (note that the concentration and amount of $FeCl_3$ solution were 100mM, 30µl). All the samples were prepared by buckypaper though filtration with an Omnipore membrane filter (JVWP 0.1 µm).

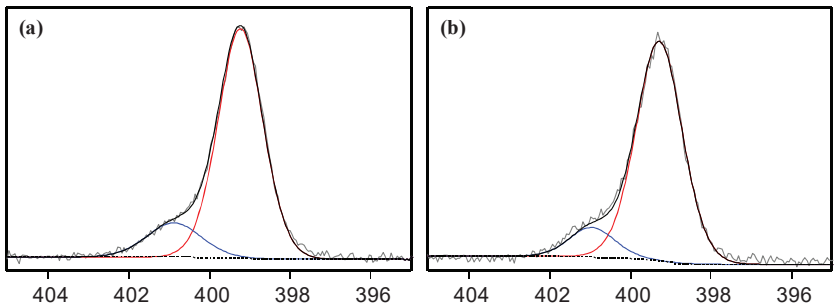

Figure 4.1.6 The XPS spectra of N1s of (a) MAP-DWNT and (b) Fe-MAP-DWNT sample (note that the concentration and amount of FeCl3 solution were 100 mM and 30 µl).

Table 4.1.3 Relative ratio of compositional atoms and oxygen-containing functional groups for pristine, MAP-dispersed DWNT supernatant, and the $FeCl_3$ (100 mM) added MAP-dispersed DWNT supernatant, respectively.

Sample ID	Atomic composition (%)				Bonding composition (%)			
	C	O	N	Fe	O-C	O=C	OCO	O-Fe
Pristine DWNTs	95.95	3.88	-	-	46.13	19.85	34.00	-
MAP-DWNTs	67.13	27.31	5.47	-	54.66	31.04	14.20	-
FeMAP-DW (30 µl)	66.67	27.86	4.67	0.79	38.86	29.77	14.60	16.57
FeMAP-DW (50 µl)	67.70	27.10	4.39	0.81	36.25	30.12	14.43	17.11

4.1.3.4 Optical Sensitivities of MAP-DW Suspension with Fe^{3+} Ions

To confirm the optical sensitivity of the MAP-dispersed DWNT supernatant in regard to the Fe^{3+} ions, Raman/fluorescent, UV-Vis-NIR absorption spectra and PL maps were measured (Figure 4.1.7,8 and 9, respectively) with 3ml of MAP-dispersed DWNT supernatant to which was added 5 to 100 µl $FeCl_3$ solution sequentially. As shown in Figure 4.1.7, with increasing amount of $FeCl_3$ solution, several strong luminescent peaks in the supernatant continuously decreased and simultaneously the RBM peak at 160 cm^{-1} disappeared, accompanying by a relative change in the RBM intensities at 237 cm^{-1} and 268 cm^{-1}. When more than 50 µl of $FeCl_3$ solution was added, the luminescent peaks disappeared completely, signifying that the hydroxyl groups within the DOPA were fully saturated with Fe^{3+} ions. Figure 4.1.8 shows that sharp absorption peaks in the UV-Vis-NIR spectra, coming from van Hove singularities of MAP-dispersed DWNT supernatant, were broadened after addition of $FeCl_3$ solution. This depressed absorption peaks can be explained by the formation of MAP-Fe^{3+} bonds on the surface of DWNTs which largely altered the electronic absorption of the inner tubes. Moreover, the inherent chiral singularities of individual DWNTs were not observed due to the electrical interaction between MAP-Fe^{3+}-linked DWNTs caused by the charge transfer effect. The broadening of the absorption peaks did not progress any more after adding 40 µl of $FeCl_3$ since all DOPA groups were consumed by bonding with Fe^{3+} ions, similar to the Raman results, as mentioned above. PL maps (Figure 4.1.9) also showed the disappearance of strong emission peaks for the MAP-dispersed DWNT supernatant after $FeCl_3$ solution was added. We observed completely depressed emissions when adding 30 µl and 50 µl of $FeCl_3$ solution. Therefore, from the combined results of Raman, UV-Vis-NIR spectra and PL maps, we observed that 3ml of MAP-dispersed DWNT supernatant was fully saturated with ca. 50 µl of $FeCl_3$ solution. From this result, the saturation ratio of Fe^{3+} with regard to MAP was decided to be ca. 9.3 wt%: 3766.7 mol% (Table 4.1.4).

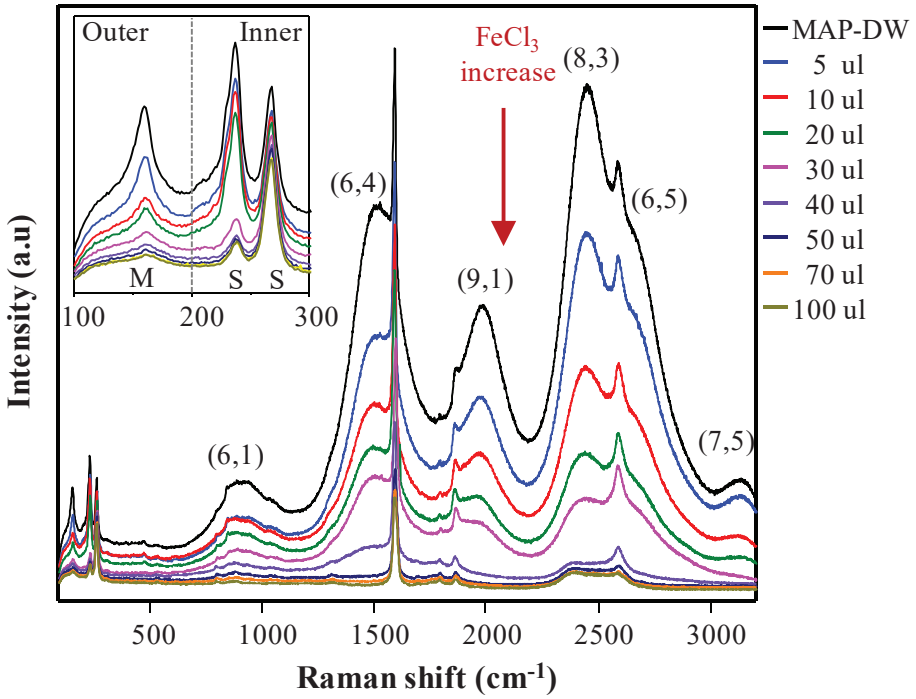

Figure 4.1.7 Raman/fluorescence spectra taken with laser excitation of 785 nm for MAP-dispersed DWNT supernatant with different amounts of $FeCl_3$ solution (100 mM). The inset shows the magnified low-frequency Raman spectra for the corresponding samples.

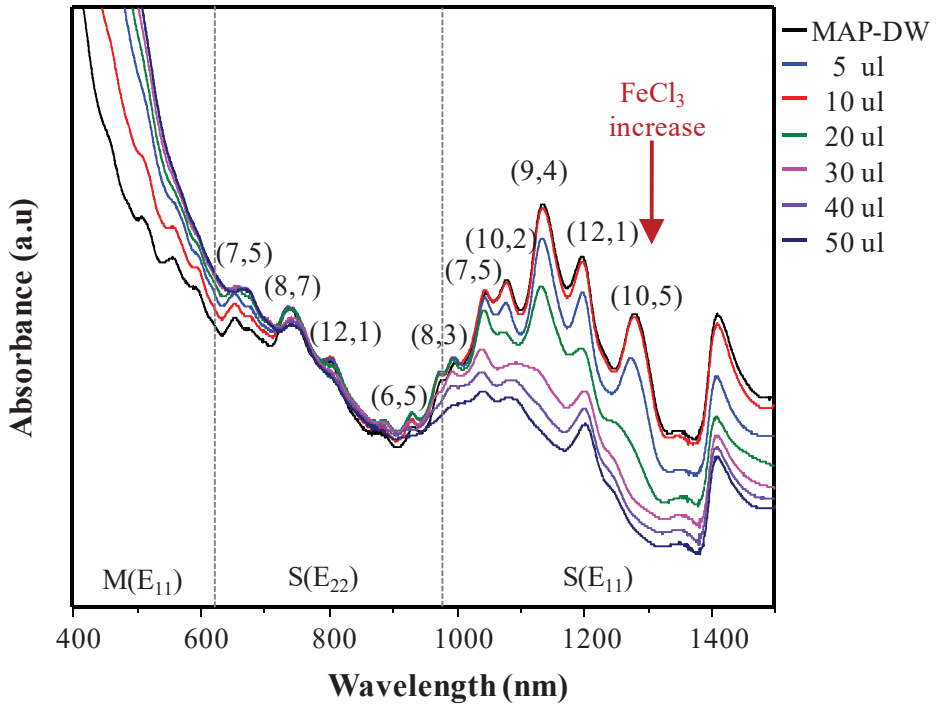

Figure 4.1.8 UV-Vis-NIR absorption spectra for MAP-dispersed DWNT supernatant with different amounts of $FeCl_3$ solution (100 mM).

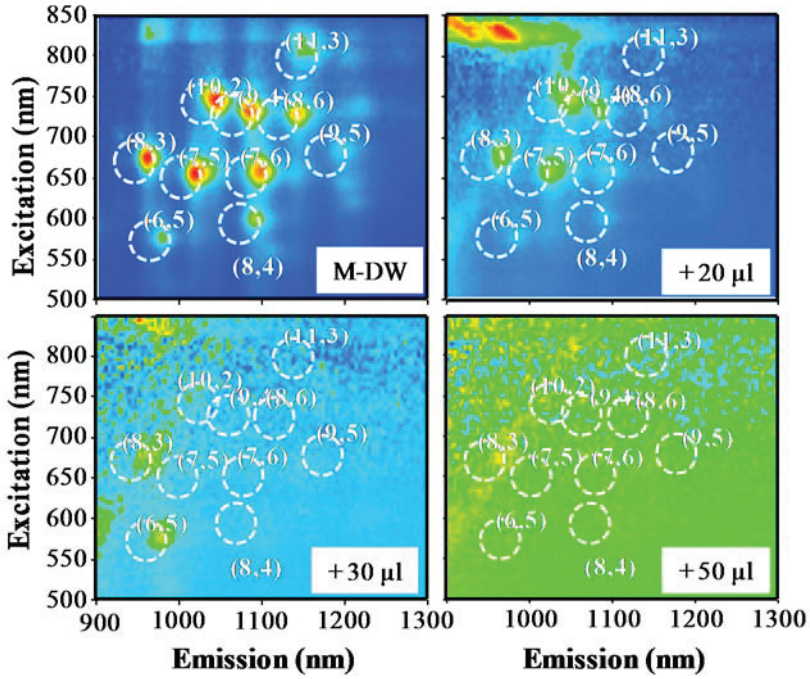

Figure 4.1.9 PL maps for MAP-dispersed DWNT supernatant with different amounts of $FeCl_3$ solution (100 mM).

Table 4.1.4 The weight (wt %) and molar (mol %) ratio of Fe^{3+} with MAP for MAP-DW suspension with different adding amount of 100mM $FeCl_3$ solution.

$FeCl_3$ Solution (ul)	Fe^{3+}		MAP [a]		Fe^{3+} / MAP	
	mg	µmol [b]	mg	µmol [b]	wt %	mol %
10	0.06	1.00	3	0.13	1.86	753.33
20	0.11	2.00	3	0.13	3.72	1506.67
30	0.17	3.00	3	0.13	5.58	2260.00
40	0.22	4.00	3	0.13	7.45	3013.33
50	0.28	5.00	3	0.13	9.31	3766.67
70	0.39	7.00	3	0.13	13.03	5273.33
100	0.56	10.00	3	0.13	18.61	7533.33

PL maps (Figure 4.1.9) also showed disappearance of strong emission peaks for the MAP-DW by adding $FeCl_3$ solution, and extremely, emissions depressed completely between 30 µl and 50 µl. Therefore, as results of Raman, UV-Vis-NIR spectra and PL maps, the 3ml of MAP-DW

4.1.4 Conclusion

In summary, I prepared individually dispersed DWNTs in aqueous solution using MAP and examined the optical sensitivity of MAP-dispersed DWNT suspensions with regard to the metal ion (Fe^{3+}) using various optical tools. With increasing dispersion state of the MAP-dispersed DWNT suspension, the intensified absorption and luminescence peaks indicated that the DWNTs were individually isolated in an aqueous solution. In comparison with SDBS-dispersed DWNT suspension, the red shift in the absorption and luminescent peaks for the MAP-dispersed DWNT suspension can be explained in terms of both the altered band-gap and the dielectric screening effect. The addition of the $FeCl_3$ solution to MAP-dispersed DWNT supernatant created the formation of coordinative bond between the DOPA of MAP and Fe^{3+} ion. From XPS spectra, we observed a transition from O-C to O-Fe bond, indicating the formation of DOPA-Fe^{3+} coordinative bonds, on addition of the $FeCl_3$ solution to MAP dispersed DWNT supernatant. The optical depression in the ferric chloride added MAP dispersed DWNT supernatant was verified by the disappearance of luminescence peaks and relative changes in the RBM intensities due to the formation of DOPA-Fe^{3+} bonds. The UV-Vis-NIR spectra also showed the loss of van Hove singularities by broadened absorption peaks on the addition of $FeCl_3$ solution. Both the depression of the BWF line and RBM peak at 160 cm^{-1} associated with metallic outer tubes indicated that the circumferentially coated MAP-Fe^{3+} complex on the outer tubes largely altered the resonance condition of the outer tubes. We also observed the optical properties to change sensitively from the Raman, UV-Vis-NIR spectra and the PL of MAP-dispersed DWNT supernatant when different amounts of the $FeCl_3$ solution were added. However, when the amount of $FeCl_3$ solution reached 50μl, the optical activities of DWNTs were completely depressed, indicating that DOPA groups in MAP were fully saturated with ca. 9.3wt% and ca. 3766.7mol% of Fe^{3+} ions. From these results, it is expected that MAP-dispersed DWNT suspensions are promising materials in the development of highly sensitive and responsive luminescence sensors for highly sensitive optoelectronic applications.

4.1.5 References

[1] K. Besteman, J. O. Lee, F. G. M. Wiertz, H. A. Heering, C. Dekker, Nano Lett. 2003, 3, 727-730.

[2] P. Asuri, S. S. Karajanagi, E. Sellitto, D. Y. Kim, R. S. Kane, J. S. Dordick, Biotechnol. Bioeng. 2006, 95, 804-811.

[3] N. Saito, K. Aoki, Y. Usui, M. Shimizu, K. Hara, N. Narita, N. Ogihara, K. Nakamura, N. Ishigaki, H. Kato, H. Haniu, S. Taruta, Y. A. Kim, M. Endo, Chem. Soc. Rev. 2011, 40, 3824-3834.

[4] A. B. Dalton, S. Collins, E. Munoz, J. M. Razal, V. H. Ebron, J. P. Ferraris, J. N. Coleman, B. G. Kim, R. H. Baughman, Nature 2003, 423, 703-703.

[5] M. Endo, H. Muramatsu, T. Hayashi, Y. A. Kim, M. Terrones, N. S. Dresselhaus, Nature 2005, 433, 476-476.

[6] W. Shi, Z. Wang, Q. C. Zhang, Y. Zheng, C. Ieong, M. Q. He, R. Lortz, Y. Cai, N. Wang, T. Zhang, H. J. Zhang, Z. K. Tang, P. Sheng, H. Muramatsu, Y. A. Kim, M. Endo, P. T. Araujo, M. S. Dresselhaus, Sci. Rep. 2012, 2, 625.

[7] Y. A. Kim, H. Muramatsu, T. Hayashi, M. Endo, M. Terrones, M. S. Dresselhaus, Chem. Vap. Deposition 2006, 12, 327-330.

[8] Y. A. Kim, K. S. Yang, H. Muramatsu, T. Hayashi, M. Endo, M. Terrones, M. S. Dresselhaus, Carbon Lett. 2014, 15, 77-88.

[9] G. M. do Nascimento, T. Hou, Y. A. Kim, H. Muramatsu, T. Hayashi, M. Endo, N. Akuzawa, M. S. Dresselhaus, Carbon 2011, 49, 3585-3596.

[10] H. Muramatsu, T. Hayashi, Y. A. Kim, D. Shimamoto, M. Endo, V. Meunier, B. G. Sumpter, M. Terrones, M. S. Dresselhaus, Small 2009, 5, 2678-2682.

[11] N. Kamaraju, S. Kumar, Y. A. Kim, T. Hayashi, H. Muramatsu, M. Endo, A. K. Sood, Appl. Phys. Lett. 2009, 95, 81106

[12] T. Hayashi, D. Shimamoto, Y. A. Kim, H. Muramatsu, F. Okino, H. Touhara, T. Shimada, Y. Miyauchi, S. Maruyama, M. Terrones, M. S. Dresselhaus, M. Endo, ACS Nano 2008, 2, 485-488.

[13] Y. Lee, K. E. Geckeler, Adv. Mater. 2010, 22, 4076-4083.

[14] S. S. Karajanagi, H. C. Yang, P. Asuri, E. Sellitto, J. S. Dordick, R. S. Kane, Langmuir 2006, 22, 1392-1395.

[15] D. Nepal, K. E. Geckeler, Small 2006, 2, 406-412.

[16] J. H. Waite, Int. J. Adhes. Adhes. 1987, 7, 9-14.

[17] B. P. Lee, P. B. Messersmith, J. N. Israelachvili, J. H. Waite, Annu. Rev. Mater. Res. 2011, 41, 99-132.

[18] S. Ryu, Y. Lee, J. W. Hwang, S. Hong, C. Kim, T. G. Park, H. Lee, S. H. Hong, Adv. Mater. 2011, 23, 1971-1975.

[19] Y. C. Jung, H. Muramatsu, K. Fujisawa, J. H. Kim, T. Hayashi, Y. A. Kim, M. Endo, M. Terrones, M. S. Dresselhaus, Small 2011, 7, 3292-3297.

[20] Z. P. Xu, Sci. Rep. 2013, 3, 2914.

[21] M. J. Harrington, A. Masic, N. Holten-Andersen, J. H. Waite, P. Fratzl, Science 2010, 328, 216-220.
[22] M. J. O'Connell, S. M. Bachilo, C. B. Huffman, V. C. Moore, M. S. Strano, E. H. Haroz, K. L. Rialon, P. J. Boul, W. H. Noon, C. Kittrell, J. P. Ma, R. H. Hauge, R. B. Weisman, R. E. Smalley, Science 2002, 297, 593-596.
[23] S. Reich, C. Thomsen, P. Ordejon, Phys. Rev. B 2002, 65, 153407.
[24] R. B. Weisman, S. M. Bachilo, Nano Lett. 2003, 3, 1235-1238.
[25] J. Lefebvre, J. M. Fraser, Y. Homma, P. Finnie, Appl. Phys. A Mater. Sci. 2004, 78, 1107-1110.
[26] Y. Miyauchi, R. Saito, K. Sato, Y. Ohno, S. Iwasaki, T. Mizutani, J. Jiang, S. Maruyama, Chem. Phys. Lett. 2007, 442, 394-399.
[27] V. V. Papov, T. V. Diamond, K. Biemann, J. H. Waite, J. Biol. Chem. 1995, 270, 20183-20192.
[28] J. Maultzsch, H. Telg, S. Reich, C. Thomsen, Phys. Rev. B 2005, 72, 205438
[29] A. M. Rao, E. Richter, S. Bandow, B. Chase, P. C. Eklund, K. A. Williams, S. Fang, K. R. Subbaswamy, M. Menon, A. Thess, R. E. Smalley, G. Dresselhaus, M. S. Dresselhaus, Science 1997, 275, 187-191.
[30] H. B. Zeng, D. S. Hwang, J. N. Israelachvili and J. H. Waite, P Natl Acad Sci USA, 2010, 107, 12850-12853.
[31] S. Y. Ma, L. Liu, V. Bromberg and T. J. Singler, J Mater Chem C, 2014, 2, 3885-3889.
[32] T. Akter, W. S. Kim, ACS Appl. Mater. Inter. 2012, 4, 1855-1859.
[33] D. A. Heller, P. W. Barone, J. P. Swanson, R. M. Mayrhofer, M. S. Strano, J. Phys. Chem. B 2004, 108, 6905-6909.
[34] A. Jorio, A. P. Santos, H. B. Ribeiro, C. Fantini, M. Souza, J. P. M. Vieira, C. A. Furtado, J. Jiang, R. Saito, L. Balzano, D. E. Resasco, M. A. Pimenta, Phys. Rev. B 2005, 72, 075207
[35] J. Jiang, R. Saito, G. G. Samsonidze, A. Jorio, S. G. Chou, G. Dresselhaus, M. S. Dresselhaus, Phys. Rev. B 2007, 75, 035407
[36] A. Jorio, M. A. Pimenta, A. G. Souza, R. Saito, G. Dresselhaus, M. S. Dresselhaus, New J. Phys. 2003, 5, 139.
[37] F. Villalpando-Paez, H. Son, D. Nezich, Y. P. Hsieh, J. Kong, Y. A. Kim, D. Shimamoto, H. Muramatsu, T. Hayashi, M. Endo, M. Terrones. M. S. Dresselhaus, Nano Lett. 2008, 8, 3879-3886.
[38] M. S. Strano, V. C. Moore, M. K. Miller, M. J. Allen, E. H. Haroz, C. Kittrell, R. H. Hauge, R. E. Smalley, J. Nanosci. Nanotechnol. 2003, 3, 81-86.
[39] J. H. Kim, M. Kataoka, D. Shimamoto, H. Muramatsu, Y. C. Jung, T. Hayashi, Y. A. Kim, M. Endo, J. S. Park, R. Saito, M. Terrones, M. S. Dresselhaus, ACS Nano 2010, 4, 1060-1066.
[40] A. M. Rao, P. C. Eklund, S. Bandow, A. Thess, R. E. Smalley, Nature 1997, 388, 257-259.

[41] D. Shimamoto, H. Muramatsu, T. Hayashi, Y. A. Kim, M. Endo, J. S. Park, R. Saito, M. Terrones, M. S. Dresselhaus, Appl. Phys. Lett. 2009, 94, 083106
[42] K. Iakoubovskii, N. Minami, T. Ueno, S. Kazaoui, H. Kataura, J. Phys. Chem. C 2008, 112, 11194-11198.
[43] H. Ago, T. Kugler, F. Cacialli, W. R. Salaneck, M. S. P. Shaffer, A. H. Windle, R. H. Friend, J. Phys. Chem. B 1999, 103, 8116-8121.
[44] H. Murphy, P. Papakonstantinou, T. I. T. Okpalugo, J. Vac. Sci. Technol. B 2006, 24, 715-720.
[45] L. M. Bronstein, A. Ivanovskaya, T. Mates, N. Holten-Andersen, G. D. Stucky, J. Phys. Chem. B 2009, 113, 647-655.
[46] T. Yamashita, P. Hayes, Appl. Surf. Sci. 2008, 254, 2441-2449.

Chapter 4

Metal Absorbed Biocomposite using Mussel Protein-inspired Double-Walled Carbon Nanotube

4.2 Mussel-Inspired Carbon Nanotube Coating on Polyvinylidene Fluoride Nanofiber filament via Metal Absorbed Complex and Vacuum Ultraviolet Irradiation

Chapter 4.2 Mussel-Inspired Carbon Nanotube Coating on Poly-vinylidene Fluoride Nanofiber filament via Metal Absorbed Complex and Vacuum Ultraviolet Irradiation

4.2.1 Introduction

Electrospinning is the simplest process to produce the nanofiber. It uses high voltage electric field to prepare the nonwoven nanofibers from electrically charged polymeric solution by whipping the jet. In general, it has been already known that the nanofiber has very large surface area to volume ratio, good flexibility in surface functionalities, and superior mechanical performance [1, 2].

However, despite the potential properties mentioned above, the applications of various nanofibers have been limited by their poor mechanical properties and the difficulties involved in mass producing them. Therefore, to improve the mechanical properties, the fabrication of nanofiber filament, prepared by the electrospinning system and the following twisting methods, was reported recently. It was reported that nanofiber filament with relatively high mechanical properties than nonwoven nanofiber can be useful for various industry areas, such as microelectronic wiring [3] and conductive fiber [4, 5]. For the same reason, various coating methods were examined to enhance the performance of the electrospun nanofiber [6, 7]. Several researchers reported that carbon nanotubes (CNTs) are great coating material because of their high electrical conductivity, good mechanical strength, and nano-sized diameter [8-12]. Especially, double-walled carbon nanotubes (DWNTs) have various advantages for bio applications due to their optical and physicochemical properties [13, 14]. However, CNTs are insoluble in aqueous solutions due to their strongly bundled structure as well as the hydrophobic nature of their sidewalls. Thus, to exploit their excellent physical and chemical properties as coating material, various biomaterials have been examined as the dispersing agent and then to fabricate CNT-biocomposites [15-17].

In recent years, the mussel-adhesive proteins (MAPs) have attracted a great attention because of their great solubility in aqueous phase and strong adhesive affinity with both hydrophilic and hydrophobic surface [18-20]. Therefore, they are expected to show good dispersing ability with regard to the strongly bundled DWNTs [21] and then they have high possibility to be used as adhesive coating agent for the electrospun-derived nanofibers. Several studies reported that 3,4-dihydroxy-L-phenylalanine (DOPA) moiety could form the strong coordinative bonding with metal ion. Thus, the MAP-dispersed DWNTs could be converted to 3D-networking structure with Fe^{3+} ions [22-25]. Therefore, it is expected that the coating of metal absorbed MAP containing DWNTs leads to the enhancement of mechanical and electrical properties of nanofiber filament.

In this study, the individually dispersed DWNT suspensions, prepared with a MAP solution and their Fe^{3+}-absorbed complex, was coated on the poly (vinylidene fluoride) (PVDF) nanofiber filament. Moreover, to partially remove residual non-conductive MAP and expose DWNTs, vacuum ultraviolet (VUV) irradiation was applied for enhancing the electric conductivity of filament. To verify chemical changes of coating on the coating surface, MAP-DWNT coated PVDF nanofiber filaments were characterized using Raman spectroscopy. Also scanning electron microscopy (SEM) was carried out to confirm the morphology of surface of filament. The mechanical and electrical properties were measured using a universal testing machine (UTM) and 2-point probe method, respectively.

4.2.2 Experimental

4.2.2.1 Preparation of Metal Absorbed MAP-DWNT Dispersion

To prepare MAP-dispersed DWNT (M-DW) solution, the prepared highly pure DWNTs (3 mg) were individually isolated in an deionized water (30 ml) with the help of MAP (pretreated mussel adhesive protein, 22.6KDa, Kollodis & Biosciences) (30mg) under strong sonication (VCX 750, Sonics & Materials, 750W) for 2 h at 4 °C. To prepare the Fe^{3+} absorbed M-DW solution (FM-DW), $FeCl_3$ solution was prepared as 100 mM solution by addition of iron (Ⅲ) chloride hexahydrate ($FeCl_3 \cdot 6H_2O$) (270.3 mg) to heavy water (10 ml). And then, the 20ul of $FeCl_3$ solution was added to the 3 ml of individually isolated M-DW solution and subsequent mild sonication (1510, Branson, 5 min) was applied. MAP solution without DWNTs was prepared by addition of MAP (10mg) to deionized water (10 ml).

4.2.2.2 Coating using MAP Dispersed DWNT Solution to PVDF Nanofiber Filament

The PVDF nanofiber filament was provided from Amogreentech (Korea). The PVDF nanofiber filaments were immersed in M-DW and FM-DW solution, and then vacuum was applied for 3 h to ensure complete infiltration of solution into the PVDF nanofiber filaments. After carefully removing the extra solution on the surface, the infiltrated M-DW and FM-DW/PLLA nanofiber filaments were dried at room temperature for 24 h.

4.2.2.3 Vacuum Ultraviolet (VUV) Treatment of the Filament Surface

A photochemical reaction was carried out by irradiating the prepared M-DW/PVDF nanofiber filament with ultraviolet light from a deuterium lamp (VUV ionizer:

L12542, HAMAMATSU) (λ = 160 nm) in vacuum condition for 20 seconds. The output power of the lamp used in our study is 90 W.

4.2.2.4 Characterization

The Raman spectra were obtained using two different lasers lines (785 nm and 514 nm) (Reinshaw, inVia Raman microscope). We also observed the morphology and elemental composition using field emission scanning electron microscopy (FE-SEM). Mechanical properties of specimens were performed by using a universal testing machine (5567A, INSTRON) under a cross-head speed of 20 mm/min at room temperature. The gauge length of nanofiber filaments was 25 mm. The drawing rate was 10 mm/min at a road cell of 100N. Electro conductivity was measured by 2-point prove method using source measure unit (2400 Source Meter, Keithley). The applied voltage and current were 10.5 V and 0.5 μA, respectively. The specific resistance and electric conductivity were based on linear resistance method, and distance of cathode and anode was 5 mm. The resulting errors in the linear resistance are estimated to be less than 10%.

4.2.3 Results and Discussion

4.2.3.1 Mussel-inspired DWNTs Coating with PVDF Nanofiber Filament

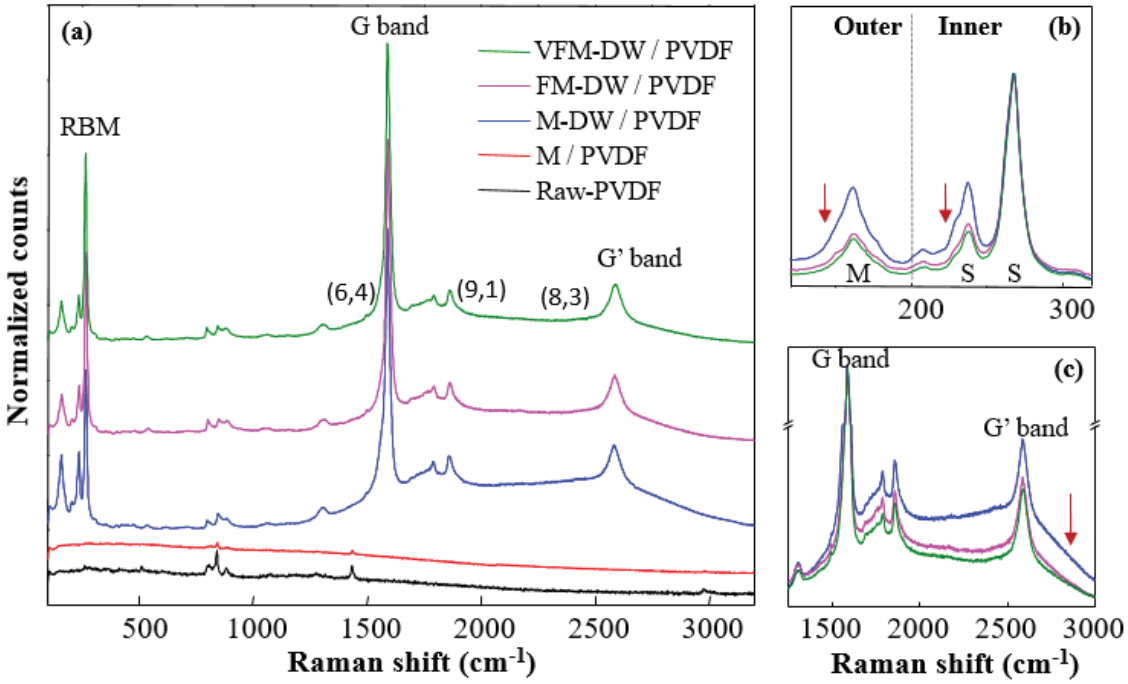

Figure 4.2.1 (a) Raman/ fluorescence spectra taken with laser excitation of 785 nm for raw, MAP, M-DW, FM-DW and VUV treated FM-DW / PVDF nanofiber filament. (b) The magnified low-frequency Raman spectra and (c) changing of fluorescence spectra for the corresponding samples.

The well dispersed M-DW solution and the effect of $FeCl_3$ addition were characterized with the help of optical tools, as reported previously [25]. Figure 4.2.1a shows wide-range Raman/fluorescence spectra taken with laser excitation of 785 nm for raw, MAP, M-DW, FM-DW and VUV treated FM-DW / PVDF nanofiber filament. From Raman spectra of MAP coated PVDF nanofiber filament without DWNTs, there is no strong Raman band and luminescence emission of MAP by excitation at 785 nm. After M-DW coating, we could see a strong G-band (E_{2g2} mode) at 1589.6 cm^{-1}, while below 400 cm^{-1}, several radial breathing mods (RBMs) could be seen with the second order symmetry-scattered G′-band at around 2584.8 cm^{-1}.[26]

Since the RBMs of CNTs are useful to provide information for the diameter, dispersion level and physicochemical environment of surrounding CNTs [25, 27, 28], the low-frequency Raman spectra is magnified (Figure 4.2.1b). From a theoretical Kataura plot based on the extended tight binding exciton model [29], we could assign the inner tubes with diameters of ca. 0.86 nm (269.3 cm^{-1}) and 0.98 nm (237.6 cm^{-1}) that are in resonance with 785 nm laser excitation to be S tubes, while the outer tubes with diameters of ca. 1.52 nm (160 cm^{-1}) were identified to be M tubes (S@M DWNT) [30, 31]. As shown in several RBM peaks, the intensity at 237.6 cm^{-1} was significantly decreased comparing with 269.3 cm^{-1}. This phenomenon indicates that the electronic structure is changed by formation of strong DOPA-Fe^{3+} bonds between individually isolated DWNTs as network structure, so that the resonance states of S inner tubes are shifted like the bundled DWNTs.[27, 32] When looking at the RBM peaks of M outer tube, the intensity at 160 cm^{-1} was maintained in M-DW/PVDF filament, but in case of FM-DW/PVDF, their intensity was decreased. This phenomenon is determined by modified directional vibration mode due to outer tubes are directly contacted with MAP-Fe^{3+} layer. It is indicating that the circumferentially generated and concentrated stress induced by surface stiffening of sidewall physically suppresses the RBM vibration in a radial direction.[25, 33]

Furthermore, luminescence peaks were observed with the M-DW/PVDF corresponding semiconducting inner tube in the isolated DWNTs. However, in case of FM-DW/PVDF, these emissions were suppressed. Since the coordinative bonding between the DOPA in MAP and Fe^{3+} ion is formed on the on the surface of DWNTs,[34] this networked structure quench luminescence similar to entrapment effect of outer tube in bundled DWNTs. Furthermore, since several DOPA groups in the MAP molecule,[22, 23] M-DWs are linked by 3D network structure form DOPA-Fe^{3+} bonding. Therefore, DWNTs loss their optical singularities by charge transfer though DOPA-Fe^{3+} linkage.[24, 25, 35] Consequently, PVDF nanofiber filaments were well-coated with MAP-inspired

DWNT solution, and isolated DWNTs were cross-linked by DOPA-Fe^{3+} bonding in the coating layer.

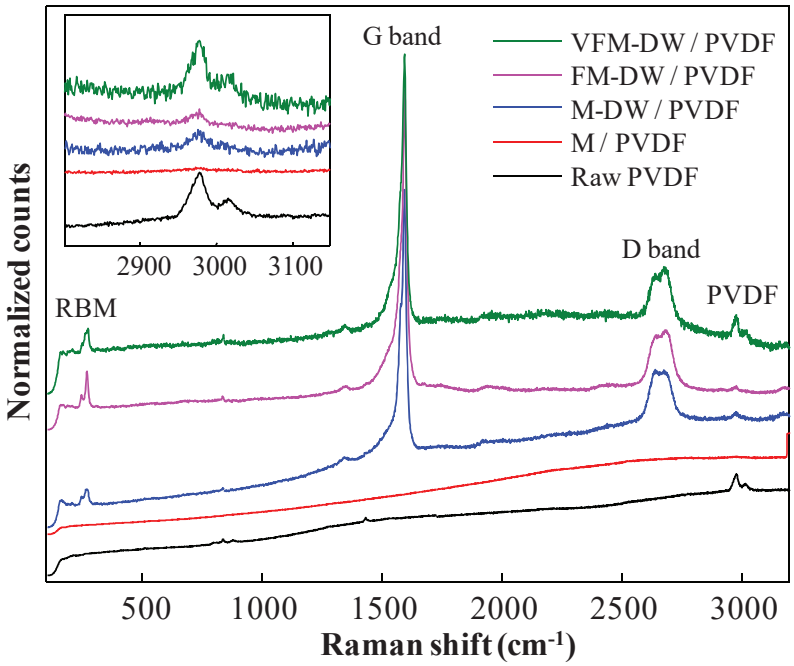

Figure 4.2.2 Raman spectra taken with laser excitation of 514 nm for raw, MAP coated, M-DW coated, FM-DW coated and VUV treated FM-DW PVDF nanofiber filament. The inset show the magnified Raman spectra for corresponding samples near the $–CH_2$ vibration of PVDF.

Figure 4.2.2 shows the Raman spectra taken with 514 nm for raw, MAP, M-DW, FM-DW and VUV treated FM-DW / PVDF nanofiber filament. As shown in this figure, strong vibration of $–CH_2$ stretching at 2978cm^{-1} was observed in the raw PVDF nanofiber filament sample. However, after coating with MAP solution, the peak corresponding PVDF was disappeared and broad luminescence of MAP was arisen. This result indicates that PVDF filament is well coated by MAP. Moreover, M-DW coated sample shows various peaks corresponding DWNTs such as D-band at 2679.3 cm^{-1}, G band at 1592.1 cm^{-1} and RBM at low frequency below 400 cm^{-1} with luminescence of MAP. Therefore, these results indicate that PVDF nanofiber filament was well coated with MAP-inspired DWNT solution. The FM-DW coated PVDF nanofiber filament show disappearance of luminescence from MAP because of formation between Fe^{3+} ion and DOPA groups in the MAP.[25] When after VUV treatment, the peak of $–CH_2$ vibration was increased comparing with non-treated FM-DW / PVDF filament, this result indicates that MAP was partial etched by VUV irradiation, so that PVDF part under the coating was exposed to the outside. However, Raman peaks corresponding DWNTs were still strongly remain, consequently, mainly MAP components was decomposed by VUV treatment.

The SEM images of MAP-inspired DWNTs coated PVDF nanofiber filaments are shown in Figure 4.2.3. As shown in Figure 4.2.3a, PVDF nanofiber filament consists of two twisted nanoweb as 2-ply yarn structure, and diameters of filament and nanofiber were ca. 336±73 μm and ca.310±78 nm, respectively. After coating FM-DW solution to filament, the diameter of nanofiber is increased to ca. 413±101nm, although diameter of filament was not changed. It is indicated that each nanofibers were well-coated with MAP-inspired DWNTs solution by complete infiltration.[36, 37] Moreover, after VUV irradiation, coating surface was etched and shrank by irradiation energy. Consequently, PVDF filament was well-coated by infiltration and vacuum dry process, and VUV treatment induce the change of surface morphology.

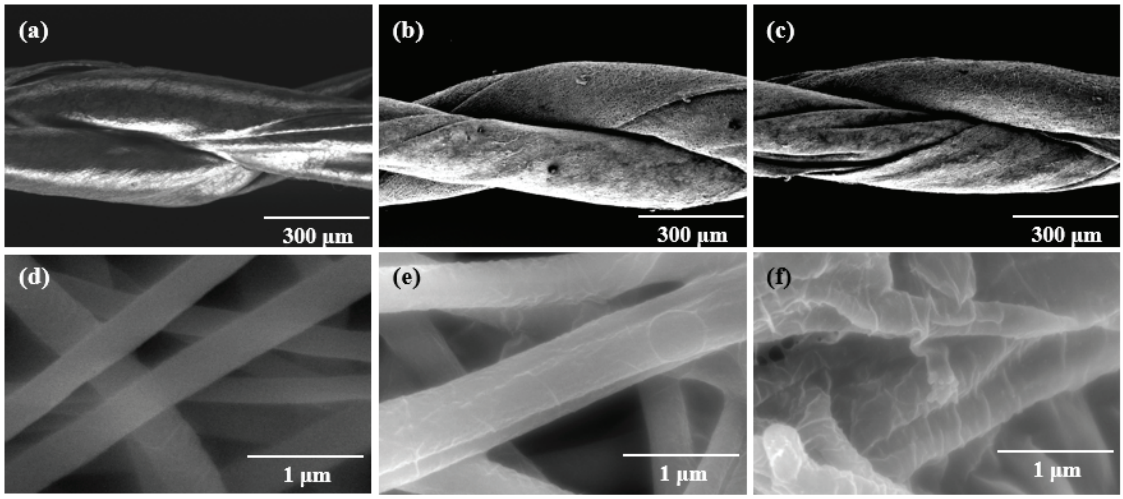

Figure 4.2.3 SEM images of MAP-inspired DWNT coated PVDF nanofiber filaments: (a,d) raw PVDF, (b,e) FM-DW coated, (c,f) VUV treated FM-DW/PVDF filament.

4.2.3.2 Mechanical Properties by Metal Absorbed MAP-DWNTs Coating

Figure 4.2.4a presents the tensile stress-strain curve, and the variation of Young's modulus, tensile strength and strain for the PVDF nanofiber filament with MAP-inspired DWNTs coating were also shown in Figure 4.2.4b. The specific value of Young's modulus, tensile strength and strain are shown in Table 4.2.1.

After coating by MAP solution without DWNTs on the PVDF filament, both of the tensile strength and strain were increased. These results indicate that MAPs were coated on the filament surface by complete infiltration, and they have mechanically enhancing performance itself. Also the tensile toughness was increased up to 257.6 mJ/m^3 by MAP coating, indicating that MAP effectively acted as a mechanical toughening agent. The decrease in the young's modulus is clear experimental evidence about the increased elastomeric property. By fully exploiting the intrinsic properties of CNTs [38], we improved young modulus, tensile stress and strain of nanofiber filaments via the coating with M-DW solution.

The noteworthy point is that mechanical properties of PVDF filament were remarkably increased by FM-DW coating. These results can be explained by cross-linking of MAP through coordinative bonding between DOPA and Fe^{3+} ion, so that it could be form the 3D networking structure.[22, 34] Thus, individually coated FM-DW layer on the each nanofiber acted as mechanical reinforcing agent of the PVDF nanofiber filament.[20] However, in case of VUV treatment FM-DW coated filament (VFM-DW/PVDF), we observed the decreased mechanical properties because of the partially etched MAP by irradiation. However, they had good performance as compare with that of M-DW/PVDF filament.

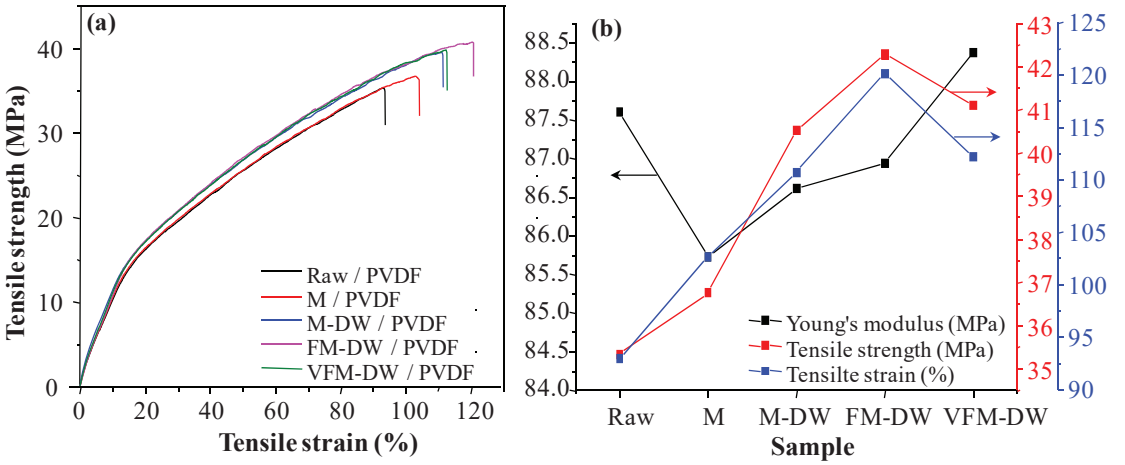

Figure 4.2.4 (a) Stress-strain curves, (b) Young's modulus, tensile strength and elongation at break of PVDF nanofiber filament with MAP-inspired DWNT coating.

Table 4.2.1 Mechanical properties of PVDF nanofiber filaments with MAP-inspired DWNT coating and VUV treatment.

Sample I.D.	Young's modulus (MPa)	Tensile strength (MPa)	Elongation at break (%)	Tensile toughness (mJ/m^{-3})
Raw PVDF	87.61±0.6	35.34±0.4	93.3±1.2	217.0
M / PVDF	85.73±0.3	36.76±0.3	103.2±3.1	257.8
M-DW / PVDF	86.65±0.7	40.52±0.3	111.1±2.7	311.2
FM-DW / PVDF	86.94±0.4	42.28±0.2	120.5±3.1	349.6
VFM-DW / PVDF	88.38±0.5	41.09±0.4	112.6±1.4	310.3

4.2.3.3 Electro Conductivity of VUV Treated FM-DW/PVDF Filament

The 2-point probe results of PVDF filament with MAP-inspired DWNT coating are shown in Table 4.2.2. Because PVDF is originally insulator,[39] the resistance of raw PVDF nanofiber filament is in the out of the range. After coating with M-DW solution, we are able to detect the resistance (ca. 9.3 MΩ), since electrically conductive DWNTs [38] were coated on the PVDF surface.

The noteworthy point is the drastically decreased resistance by FM-DW coating. This result can be explained by the formation of charge transferable network structure in the DWNT-MAP-Fe^{3+} complex layer. The coordinative bonding between MAP-Fe^{3+} and electrically conductive iron ion make more electrically transferable environmental. In addition, VUV treat induces significantly decreased resistance down to 0.65 MΩ. This results indicat that DWNTs were exposed because of partially etched MAP under VUV treatment. Consequently, using Fe^{3+} addition and VUV treatment, MAP-inspired DWNTs coating induced drastic enhancement of electrical conductivity of nanofiber filament.

Table 4.2.2 Electrical properties of MAP-inspired PVDF filament with Fe^{3+} complex and VUV treatment

Sample I.D	Resistance (MΩ)	Specific resistance (Ω·m)	Electric conductivity ($S \cdot m^{-1}$)
PVDF	n/a	n/a	0
M-DW / PVDF	9.35	84.1	0.012
FM-DW / PVDF	1.21	10.9	0.091
VFM-DW / PVDF	0.65	5.88	0.170

4.2.4 Conclusion

In summary, we have successfully coated MAP-inspired DWNTs solution on the PVDF nanofiber filament surface and verified improvements of physical performance by formation of metal absorbed complex and VUV irradiation.

By using Raman/ luminescence spectroscopy, it is confirmed that M-DW solution was well coated on the surface of PVDF filament, as results from appearance of G-, D-band and RBM corresponding DWNTs, and luminescence of MAP. Moreover, Fe^{3+} absorbed complex were photochemically verified at excitation with 785nm by RBM and luminescence change of DWNTs. From the increased intensity of PVDF after VUV treatment, we verified that the optical irradiation partially etched the MAPs.

The mechanical properties of PVDF filaments were significantly enhanced by MAP-inspired DWNTs coating. Furthermore, Fe^{3+} absorbed MAP-DWNT coating induced remarkable improvement of tensile toughness by ca. 61.1 % comparing with raw filament. This enhancement occurred by formation of coordinative bonding between Fe^{3+} and MAP. The electrical properties also enhanced by MAP-inspired DWNTs coating due to DWNTs, and Fe^{3+} induced drastic improvement of electric conductivity. Furthermore, after VUV treatment, electric conductivity was greatly increased by above 13 times.

Consequently, we confirm that MAP-inspired DWNTs coating is highly effective physical reinforcing agent for nanofiber, and mechanical/electrical performance could be enhance by formation of metal absorbed complex and VUV treatment.

4.2.5 References

[1] Z.M. Huang, Y.Z. Zhang, M. Kotaki, S. Ramakrishna, *Composites Science and Technology,* **63**, 2223-2253, (2003)

[2] T. Subbiah, G.S. Bhat, R.W. Tock, S. Pararneswaran, S.S. Ramkumar, *Journal of Applied Polymer Science,* **96**, 557-569, (2005)

[3] A. Theron, E. Zussman, A.L. Yarin, *Nanotechnology,* **12**, 384-390, (2001)

[4] A.G. MacDiarmid, W.E. Jones, I.D. Norris, J. Gao, A.T. Johnson, N.J. Pinto, J. Hone, B. Han, F.K. Ko, H. Okuzaki, M. Llaguno, *Synthetic Metals,* **119**, 27-30, (2001)

[5] I.D. Norris, M.M. Shaker, F.K. Ko, A.G. MacDiarmid, *Synthetic Metals,* **114**, 109-114, (2000)

[6] J. Zeng, A. Aigner, F. Czubayko, T. Kissel, J.H. Wendorff, A. Greiner, *Biomacromolecules,* **6**, 1484-1488, (2005)

[7] W. He, Z.W. Ma, T. Yong, W.E. Teo, S. Ramakrishna, *Biomaterials,* **26**, 7606-7615, (2005)

[8] C.M. Trottier, P. Glatkowski, P. Wallis, J. Luo, *Journal of the Society for Information Display,* **13**, 759-763, (2005)

[9] E.W. Keefer, B.R. Botterman, M.I. Romero, A.F. Rossi, G.W. Gross, *Nature Nanotechnology,* **3**, 434-439, (2008)

[10] A.B. Dalton, S. Collins, E. Munoz, J.M. Razal, V.H. Ebron, J.P. Ferraris, J.N. Coleman, B.G. Kim, R.H. Baughman, *Nature,* **423**, 703-703, (2003)

[11] M. Endo, H. Muramatsu, T. Hayashi, Y.A. Kim, M. Terrones, N.S. Dresselhaus, *Nature,* **433**, 476-476, (2005)

[12] W. Shi, Z. Wang, Q.C. Zhang, Y. Zheng, C. Ieong, M.Q. He, R. Lortz, Y. Cai, N. Wang, T. Zhang, H.J. Zhang, Z.K. Tang, P. Sheng, H. Muramatsu, Y.A. Kim, M. Endo, P.T. Araujo, M.S. Dresselhaus, *Sci Rep-Uk,* **2**, (2012)

[13] Y.A. Kim, H. Muramatsu, T. Hayashi, M. Endo, M. Terrones, M.S. Dresselhaus, *Chem Vapor Depos,* **12**, 327-+, (2006)

[14] Y.A. Kim, H. Muramatsu, M. Kojima, T. Hayashi, M. Endo, M. Terrones, M.S. Dresselhaus, *Chem Phys Lett,* **420**, 377-381, (2006)

[15] Y. Lee, K.E. Geckeler, *Adv Mater,* **22**, 4076-4083, (2010)

[16] S.S. Karajanagi, H.C. Yang, P. Asuri, E. Sellitto, J.S. Dordick, R.S. Kane, *Langmuir,* **22**, 1392-1395, (2006)

[17] D. Nepal, K.E. Geckeler, *Small,* **2**, 406-412, (2006)

[18] J.H. Waite, *Int J Adhes Adhes,* **7**, 9-14, (1987)

[19] B.P. Lee, P.B. Messersmith, J.N. Israelachvili, J.H. Waite, *Annu Rev Mater Res,* **41**, 99-132, (2011)

[20] S. Ryu, Y. Lee, J.W. Hwang, S. Hong, C. Kim, T.G. Park, H. Lee, S.H. Hong, *Adv Mater,* **23**, 1971-1975, (2011)

[21] Y.C. Jung, H. Muramatsu, K. Fujisawa, J.H. Kim, T. Hayashi, Y.A. Kim, M. Endo, M. Terrones, M.S. Dresselhaus, *Small,* **7**, 3292-3297, (2011)

[22] Z.P. Xu, *Sci Rep-Uk,* **3**, (2013)

[23] M.J. Harrington, A. Masic, N. Holten-Andersen, J.H. Waite, P. Fratzl, *Science,* **328**, 216-220, (2010)
[24] T. Akter, W.S. Kim, *Acs Appl Mater Inter,* **4**, 1855-1859, (2012)
[25] Y.I. Ko, C.S. Kang, E.A. Shin, Y.C. Jung, H. Muramatsu, T. Hayashi, Y.A. Kim, M.S. Dresselhaus, *Rsc Advances,* **6**, 16308-16313, (2016)
[26] A.M. Rao, E. Richter, S. Bandow, B. Chase, P.C. Eklund, K.A. Williams, S. Fang, K.R. Subbaswamy, M. Menon, A. Thess, R.E. Smalley, G. Dresselhaus, M.S. Dresselhaus, *Science,* **275**, 187-191, (1997)
[27] D.A. Heller, P.W. Barone, J.P. Swanson, R.M. Mayrhofer, M.S. Strano, *J Phys Chem B,* **108**, 6905-6909, (2004)
[28] A. Jorio, A.P. Santos, H.B. Ribeiro, C. Fantini, M. Souza, J.P.M. Vieira, C.A. Furtado, J. Jiang, R. Saito, L. Balzano, D.E. Resasco, M.A. Pimenta, *Phys Rev B,* **72**, (2005)
[29] J. Jiang, R. Saito, G.G. Samsonidze, A. Jorio, S.G. Chou, G. Dresselhaus, M.S. Dresselhaus, *Phys Rev B,* **75**, (2007)
[30] A. Jorio, M.A. Pimenta, A.G. Souza, R. Saito, G. Dresselhaus, M.S. Dresselhaus, *New J Phys,* **5**, (2003)
[31] F. Villalpando-Paez, H. Son, D. Nezich, Y.P. Hsieh, J. Kong, Y.A. Kim, D. Shimamoto, H. Muramatsu, T. Hayashi, M. Endo, M. Terrones, M.S. Dresselhaus, *Nano Lett,* **8**, 3879-3886, (2008)
[32] M.S. Strano, V.C. Moore, M.K. Miller, M.J. Allen, E.H. Haroz, C. Kittrell, R.H. Hauge, R.E. Smalley, *J Nanosci Nanotechno,* **3**, 81-86, (2003)
[33] J.H. Kim, M. Kataoka, D. Shimamoto, H. Muramatsu, Y.C. Jung, T. Hayashi, Y.A. Kim, M. Endo, J.S. Park, R. Saito, M. Terrones, M.S. Dresselhaus, *Acs Nano,* **4**, 1060-1066, (2010)
[34] H.B. Zeng, D.S. Hwang, J.N. Israelachvili, J.H. Waite, *P Natl Acad Sci USA,* **107**, 12850-12853, (2010)
[35] S.Y. Ma, L. Liu, V. Bromberg, T.J. Singler, *J Mater Chem C,* **2**, 3885-3889, (2014)
[36] Y.I. Ko, B.S. Kim, J.S. Bae, Y.A. Kim, I.S. Kim, *Rsc Advances,* **3**, 20091-20098, (2013)
[37] Y.K. Ko, C. Im, J. Do, Y.S. Park, *European Journal of Organic Chemistry,* **2014**, 3460-3467, (2014)
[38] Y.A. Kim, K.S. Yang, H. Muramatsu, T. Hayashi, M. Endo, M. Terrones, M.S. Dresselhaus, *Carbon Letters,* **15**, 77-88, (2014)
[39] S.H. Lim, A.C. Rastogi, S.B. Desu, *Journal of Applied Physics,* **96**, 5673-5682, (2004)

Chapter 4

Metal Absorbed Biocomposite using Mussel Protein-inspired Double-Walled Carbon Nanotube

4.3 Double walled Carbon Nanotube Based Aerogel via Coacervation of Mussel Adhesive Protein and Single Stranded Deoxyribonucleic Acid

Chapter 4.3 Double walled Carbon Nanotube Based Biocompatible Aerogel via Coacervation of Mussel Adhesive Protein and Single Stranded Deoxyribonucleic Acid

4.3.1 Introduction

Aerogels are exceptionally porous materials having large pore volumes and low bulk densities. Their unique structure provides remarkable properties and wide applications.[1-3] In spite of the considerable need using aerogels, only limited types of materials can be produced into the ‘‘aerogel’’ structure. In generally, these high valuable aerogel could be converted from sol-gel method.[4] Coacervation is electrostatically-driven sol phase separation in liquid, inducing from aggregation of oppositely charged particles.[5] It is expected that investigation of protein-polyelectrolyte complexes having self-organized systems can impart useful applications in bio medical area.[6, 7] However, coacervate is type of sol, additional method will be necessary to convert into aerogel such as chemical bonding and cross-linker.

In recent years, carbon nanotubes (CNTs) have been widely used in biomaterial applications such as drug delivery systems, biocatalyst, and biosensors [8-10] because of their high physical properties and and nano-sized diameter.[11-13] Several researchers reported that CNTs are good 1D material for preparation of aerogel.[14] Thus, it is expected that CNTs could be used for conversion coacervate into aerogel as physical cross-linker. The single stranded DNA (ssDNA) and mussel adhesive protein (MAP) have attracted a great attention as dispersing agent with regard to the st r ongly bundled CNTs.[15-17] Moreover, it is expected that they can form the coacervate phase by combination of negatively charged ssDNA (phosphate groups) and positively charged MAP (amine groups).[18, 19] MAP’s ability to form the coordinative bond with metal ion[19] can help to proceed the gelation process via the formation of chemical bonding. Thus, it is possible to prepare aerogel from ssDNA-MAP coacervate using DWNTs using the sol-gel method.

In this study, from coacervation with MAP and ssDNA-dispersed CNTs, aerogel was prepared by sol-gel method and freeze drying. The coacervation process was confirmed by optical analysis using Raman/fluorescence and UV-Vis-NIR spectroscopy, and electrokinetic analysis using dynamic light scattering (DLS). Furthermore, mechanical and electrical performances were measured to verify the optically active, mechanically strong, electrically conductive, and biologically active metal-absorbed MAP-ssDNA-DWNTs aerogel.

4.3.2 Experimental

4.3.2.1 Synthesis of the High Purity DWNT Sample

The synthesis of DWNTs was carried out by the catalytic chemical vapor deposition method with furnace using Mo/Al_2O_3 and Fe/MgO as conditioning catalyst and nanotube catalyst, respectively. Subsequently, a methane/argon (1:1) mixture was fed into the reactor typically for 10 min at 875 °C. A purification processes were applied to the as-grown products by following methods: Firstly, an oxidation process (500 °C, 20 min) was carried out to reduce the chemically active SWNTs. Secondly a hydrochloric acid (18%, 100 °C, 10 h) treatment was carried out in order to remove the metal catalysts, followed by air oxidation at 500 ° C for 10 min in order to remove carbonaceous impurities. The detailed experimental procedures were described in our previous papers. [20, 21]

4.3.2.2 Dispersion of DWNTs using ssDNA in Aqueous Phase

The prepared highly pure DWNTs (1 mg) were individually isolated in an deionized water (10 ml) with the help of single-stranded deoxyribonucleic acid (ssDNA) (Aldrich) (10mg) under strong sonication (VCX 750, Sonics & Materials, 750W) for 1 hr at 4 °C, and subsequent ultracentrifugation (Optima Max-XP, Beckman Coulter, 240000g) for 1hr at 5 °C. Their supernatant of ssDNA-dispersed DWNT (D-DW) suspension (70%), rich with isolated nanotubes, was obtained and characterized in our optical study. In the following procedure for preparing aerogel, D-DW solutions without centrifugation were also used in order to high contents of DWNTs. To verify dispersibility and chemical effect of ssDNA, MAP-dispersed DWNTs (M-DW) and sodium dodecyl benzene sulfonate (SDBS) -dispersed DWNTs (S-DW) were prepared as previous chapter.

4.3.2.3 Coacervation of Metal-Absorbed MAP-ssDNA-DWNT

To prepare coacervate, MAP (pretreated mussel adhesive protein, 22.6 KDa, Kollodis & Biosciences) (10mg) was dissolved in the 10 ml of deionized water. The prepared MAP solution (1mg/ml) was added to the 3 ml of D-DW supernatant or D-DW dispersion without centrifugation by various wt% vs ssDNA. To achieve highly cross-linked gel phase, $FeCl_3$ solution (100 mM) was added to MAP-ssDNA-DWNT emulsion (MD-DW). $FeCl_3$ solution (100 mM) was prepared by addition the iron chloride hexahydrate ($FeCl_3 \cdot 6H_2O$ Aldrich) (270.3 mg) to 10 ml of deionized water.

4.3.2.4 Conversion Coacervate into Aerogel

Fe^{3+}-absorbed MD-DW prepared from D-DW supernatant (FMD-DW) and FMD-DW having high DWNTs contents without centrifugation (hFMD-DW) were concentrated in the vacuum chamber for 12, and subsequent mild sonication was applied (1510, Branson, 10 min). And then, gelated emulsion was converted to aerogel by freeze drying (FDU-1200, EYELA) for 48 h.

4.3.2.5 Characterization

The optical spectra for DWNT suspensions were obtained using a UV–vis–NIR spectrophotometer (V-670, JASCO) and a 785 nm excited Raman system (Reinshaw, inVia Raman microscope).

To verify surface energy and size changing of coacervate, zeta-potential and size of particle were measured by dynamic light scattering (DLS, Zetasizer Nano ZS, Malvern). And structural durability of FMD-DW aerogel was measured by simple press of ca.10g of slide glass to compare FMD without DWNTs and FMD-DW supernatant. Moreover, to identify the electro conductive property of FMD-DW aerogel, simple on-off test of LED bulb was measured by touch the electrode to aerogel under 4.5 V voltage.

4.3.3 Results and Discussion

4.3.3.1 Preparation of Individually Dispersed ssDNA-DWNT Suspension

Figure 4.3.1a and 1b show wide-range Raman/fluorescence spectra taken with laser excitation at 785nm and UV-Vis-NIR absorption spectra for pristine DWNTs, MAP-DW supernatant, D-DW remnant and D-DW supernatant, respectively. From the Raman spectra of pristine DWNTs, we could see a strong G-band (E_{2g2} mode) at 1590 cm^{-1}, while below 400 cm^{-1}, several RBMs (which correspond to a coherent vibration of the carbon atoms normal to the tube axis) could be seen along with the second order symmetry-allowed G′-band at around 2588 cm^{-1}.[22] As shown in this figure, D-DW supernatant exhibited well resolved strong luminescence peaks (Figure 4.3.1a) and sharp absorption peaks (Figure 4.3.1b), and they were not able to observe in the remnant state because of bundled tubes.[23] Therefore, it indicating that individually dispersed DWNTs were generated through the strong interaction with ssDNA.[15, 21]

To confirm the optoelectric effects of ssDNA as dispersing agent for DWNTs, we measured optical change comparing ssDNA with SDBS using optical analysis. As shown in Figure 4.3.1a, the luminescent spectra of the D-DW suspension is red-shifted by 133 cm^{-1} ((8,3), ca. 165 meV) compared to that of the S-DW suspensions. Moreover, the bathochromic shifted UV-Vis-NIR absorption peak comparing D-DW with S-DW suspension by 14 nm ((8,3), ca. 177 meV) is observed in Figure 4.3.1b. This red-shift

phenomenon of D-DW could be explained by environmental dielectric screening effects.[24, 25] Furthermore, since strong electron-donating groups such as phosphate, carbonyl and amine group in ssDNA structure,[18] the electron density of DWNTs in D-DW solution is higher than SDBS. As a result of this electron-donating effect, since excitons could be easily excited, both of absorption and luminescent emission were red-shifted by reduction of energy-gap.[17, 26]

Since the RBMs of DWNTs are well-known to provide information on the chirality and diameter,[27, 28] the low-frequency Raman spectra is magnified (inset in Figure 4.3.1a). Several studies reported that the resonance singularity in the RBM of CNTs is dependent on the bundle organization and inter-nanotube contact area due to modified electronic structure. Therefore, it is confirmed that aggregation affects the excitation state and cause changing of intensity of RBM.[27, 29] In the case of the supernatant of D-DW, the RBM peaks from S inner tube exhibited increasing intensity at 236.3 cm^{-1} and relatively decreasing intensity at 267.4 cm^{-1} comparing with bundled P-DW and remnant of D-DW. Thus, it is confirmed that this result could be evidence of dispersibility of ssDNA for DWNTs.

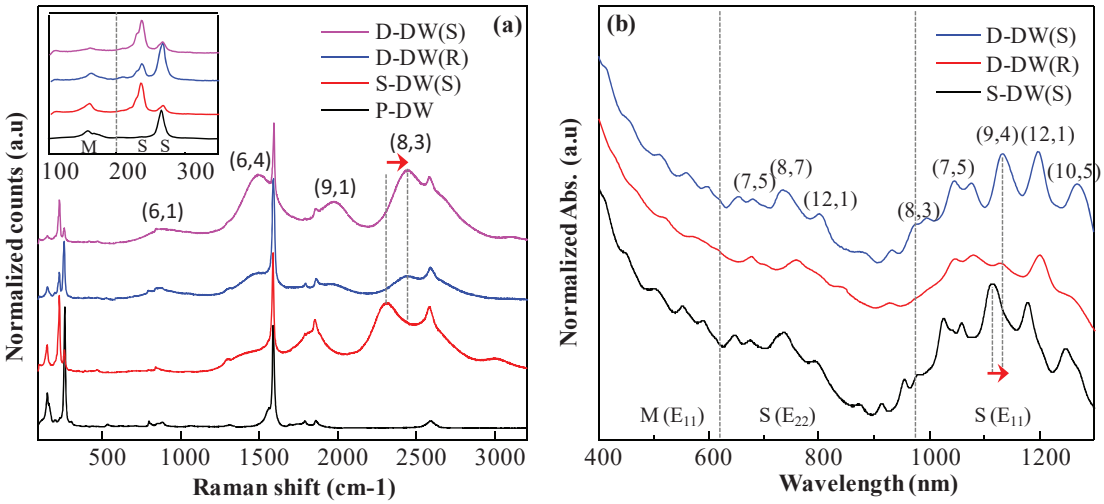

Figure 4.3.1 (a) Wide-range Raman/fluorescence spectra, (b) UV-Vis-NIR absorption spectra for pristine P-DW, S-DW supernatant (S), D-DW remnant (S) and D-DW supernatant (R). Inset of 1a shows corresponding radial breathing mode (RBM).

4.3.3.2 Raman/fluorescence and UV-Vis-NIR Spectra of Coacervate

Figure 4.3.2a shows wide-range Raman/fluorescence spectra taken with laser excitation of 785 nm for D-, M-, MD- and FMD-DW solutions. As shown in this figure, D-DW suspension shows strong luminescence peaks as mentioned above. The M-DW suspension shows emission at more longer wavelength comparing with D-DW suspension by +27 cm^{-1} ((8,3), ca.-33 meV). When addition MAP solution to D-DW suspension (300 wt% vs ssDNA), bathochromic shift was appeared by +48 cm^{-1} ((8,3), ca. -59 meV) comparing with D-DW. These results indicated that optochemical environment surrounding DWNTs was modified with addition of MAP into D-DW solution, and their coacervate structure is chemically different from M-DW. Moreover, although high turbidity of MD-DW emulsion, their luminescence were still strong. Therefore, MD-DW coacervates maintained individually isolated DWNTs structure, even if suspension converted to opaque emulsion having large particles (Figure 4.3.3). After adding 50µl of $FeCl_3$ solution (100mM) to MD-DW emulsion, the luminescence peaks corresponding van Hove singularities were completely disappeared. It is indicated that MD-DW coacervates were cross-linked by coordinative bonding between Fe^{3+} and MAP as studied previous chapter.[17]

As shown in Figure 4.3.2b, RBM peaks of D-DW indicate individually dispersed DWNTs due to high intensity of 0.99 nm semiconducting tube corresponding isolated DWNTs.[27] This individual dispersion state was maintained even after addition of MAP into D-DW, as shown still strongly existing peak of isolated DWNTs. Consequently, as shown in photo image of Figure 4.3.3, addition of MAP to D-DW induced growth of coacervate and conversion to emulsion of high turbidity, it is verified that dispersion state of individually isolated DWNTs was maintained. But on the other hands, when after adding Fe^{3+}, the intensity at 236.3 cm^{-1} was significantly decreased and 267.4 cm^{-1} was increased. This phenomenon indicates that the electronic structure is changed by formation of strong DOPA-Fe^{3+} bonds between individually isolated DWNTs as 3D network structure, so that the resonance states of S inner tubes are shifted like the bundled DWNTs.[17]

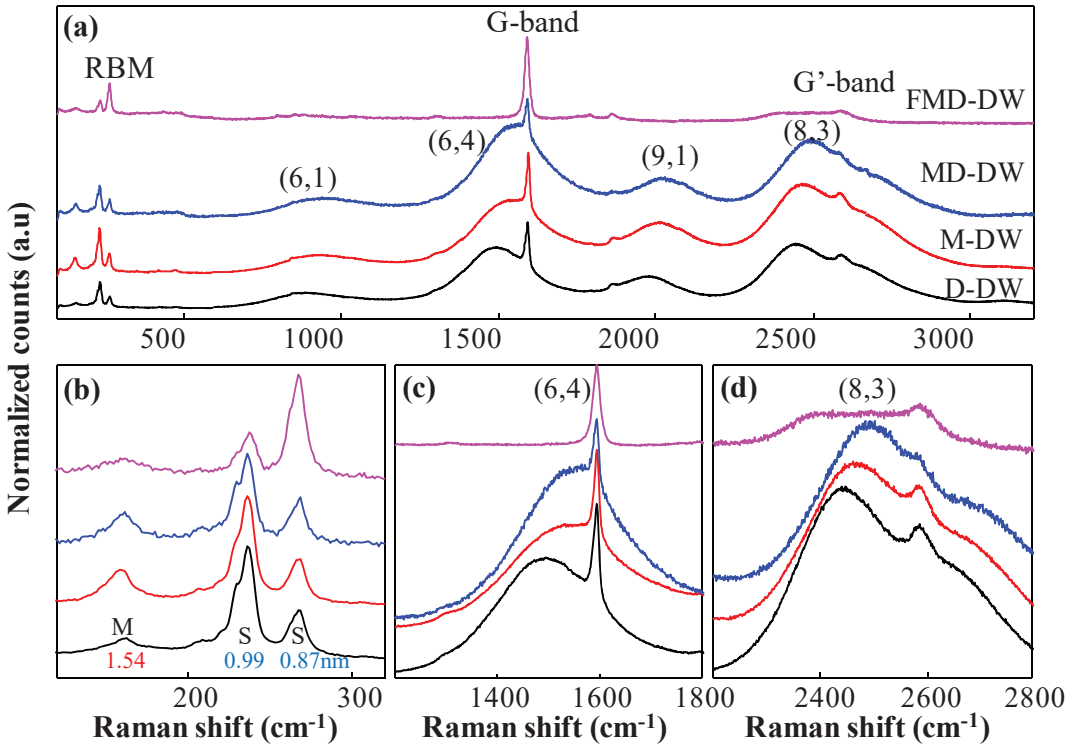

Figure 4.3.2 (a) Raman/fluorescence spectra taken with laser excitation of 785 nm for D-DW, M-DW, MD-DW and FMD-DW suspension, their corresponding (b) radial breathing mode, (c) around G-band, and (d) around G'-band.

Figure 4.3.3 The ultracentrifugated semitransparent D-DW suspension (left), the following addition of MAP to D-DW suspension (middle) and after adding 20µl of $FeCl_3$ solution (100mM) to MAP-DW suspension.

The UV-Vis-NIR absorption spectra of MD-DW show bathochromic shifted absorption peaks comparing with D-DW and they show strong absorption at longer wavelength comparing with M-DW (Figure 4.3.4). These results also indicate that MD-DW coacervate is chemically different from D-DW and M-DW. Specific values of red-shift and energy gap were calculated in Table 4.3.1. However, after addition of $FeCl_3$ to MD-DW solution, sharpness of absorption peaks were decreased due to the formation of the electrical network and the surface hardening effect of MAP-Fe^{3+} bond, as mentioned previous chapter.[17]

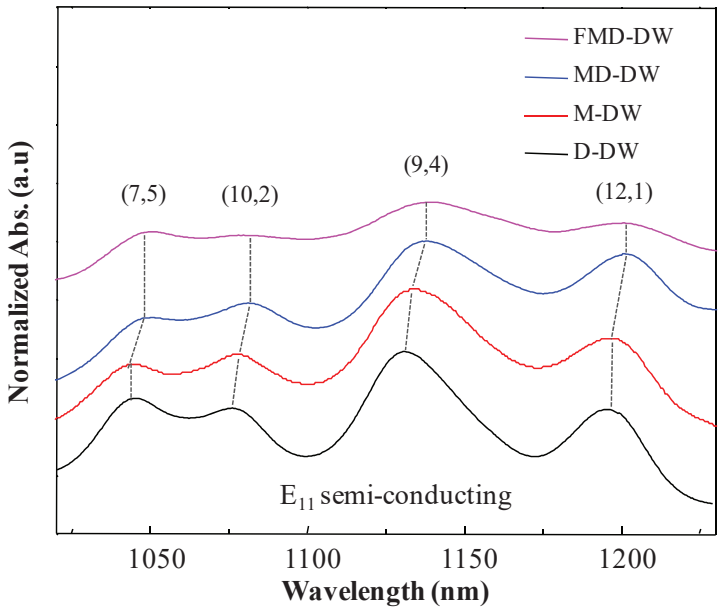

Figure 4.3.4 UV-Vis-NIR absorption spectra for D-, M-, MD- and FMD-DW suspension.

Table 4.3.1 Structures and first van Hove optical transitions for Semiconducting D- and MD-dispersed DWNTs from UV-Vis-NIR spectroscopy.

Chirality	D-DW		MD-DW			
	λ_{ii} (nm)	E_{ii} (eV)	λ_{ii} (nm)	E_{ii} (eV)	$\Delta\lambda$ (nm)	ΔE_{ii} (ΔmeV)
(12,1)	1196	1.037	1202	1.032	6	-5.179
(9,4)	1131	1.097	1139	1.089	8	-7.706
(10,2)	1076	1.153	1081	1.148	5	-5.334
(7,5)	1044	1.189	1048	1.184	4	-4.536

4.3.3.3 Optically Sensitive Coacervation Process of D-DW with MAP and Fe^{3+}

To confirm the optical activity of FMD-DW, Raman/fluorescent and UV-Vis-NIR absorption spectroscopy were carried out. As shown in Figure 4.3.5, when increasing amounts of MAP solution, the emissions of luminescence corresponding van Hove singularities were shifted to high frequency. But after addition above 300 wt% of MAP vs ssDNA, these bathochromic phenomena were completely stopped and maintained their emission without any change. These results indicated that the phosphate groups in the ssDNA were fully saturated with cationic groups of the MAP. But after addition of $FeCl_3$ solution, several luminescence peaks and RBM peaks at 236.3 cm^{-1} was extremely decreased (Figure 4.3.6). These results induced by several chemical and physical effects as discussed above. Significantly, luminescent peaks were completely extinguished similar to pristine DWNTs when adding more than 40 μl of $FeCl_3$ solution, and it indicated that hydroxyl groups in the DOPA were fully saturated with Fe^{3+} ions.[17]

The UV-Vis-NIR spectra of D-DW with addition of MAP and $FeCl_3$ were shown in Figure 4.3.7. As similar results from Raman measurement, the bathochromic shift was occurred by addition of the MAP into D-DW suspension, oppositely, sharpness of absorption was decreased without red shift by addition of $FeCl_3$. Consequently, we could be verified saturation point of ssDNA-MAP coacervate, and their highly sensitive optochemical properties were confirmed by optical analysis.

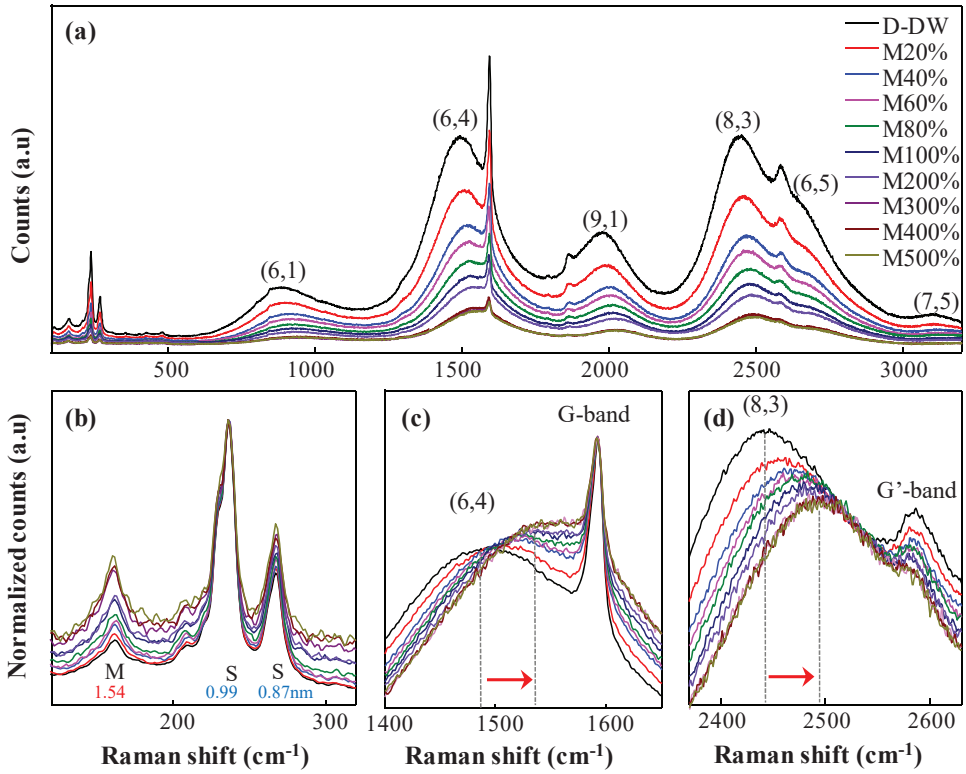

Figure 4.3.5 (a) Raman/fluorescence spectra taken with laser excitation of 785 nm for D-DW suspension with different amounts of MAP solution (1mg/ml), and their corresponding normalized (b) RBM, (c) luminescence of (6,4) tube and (d) (8,3) tube.

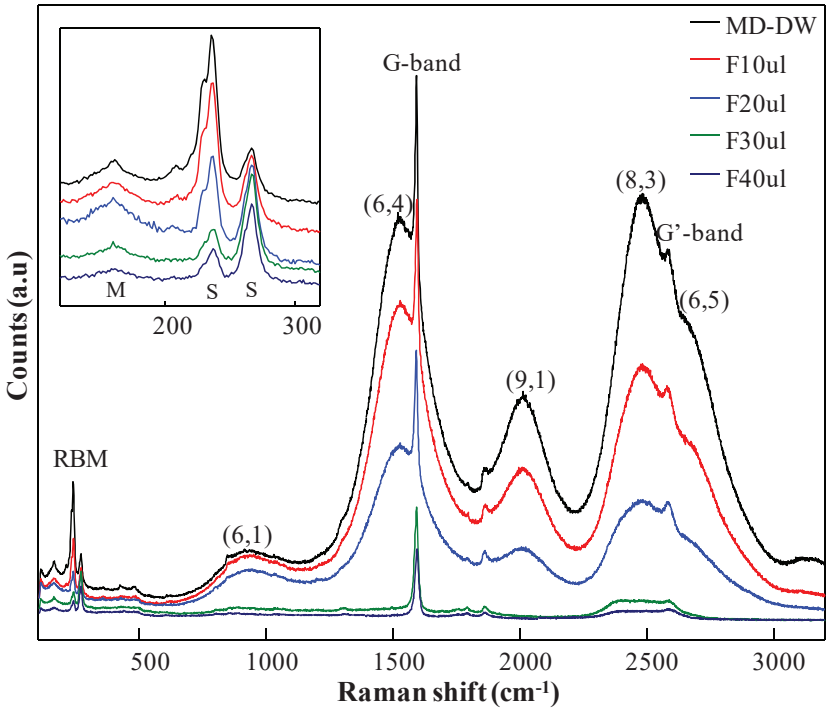

Figure 4.3.6 Raman/fluorescence spectra taken with laser excitation of 785 nm for MD-DW with different amounts of $FeCl_3$ solution (100mM). The inset shows the magnified low-frequency Raman spectra for the corresponding samples.

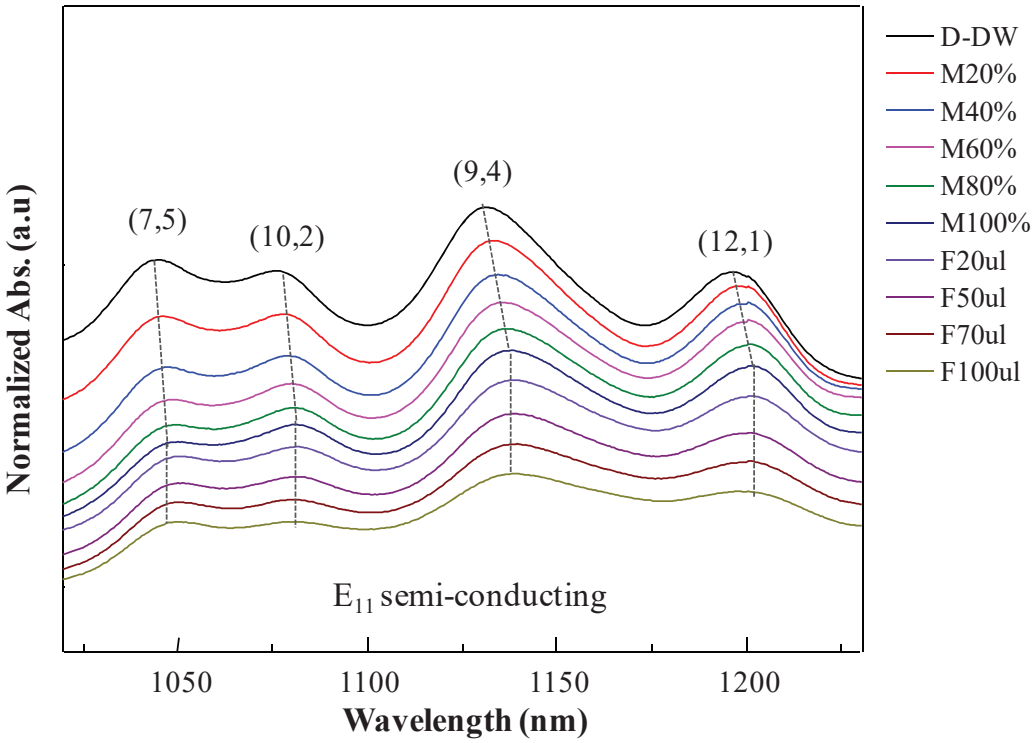

Figure 4.3.7 UV-Vis-NIR absorption spectra of MD-DW solutions with different amounts of $FeCl_3$ solution (100mM).

4.3.3.4 Dynamic light scattering (DLS) measurement of FMD-DW coacervate

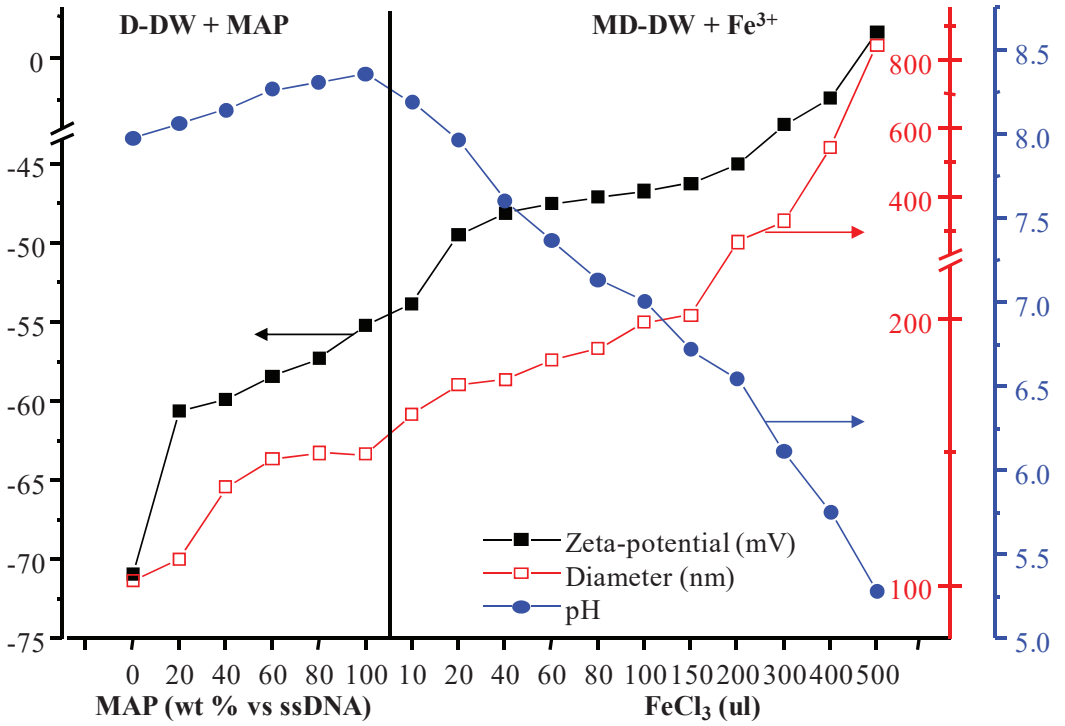

Figure 4.3.8 The changing of Zeta-potential, particle size and pH of D-DW solution with addition of MAP and Fe^{3+} from dynamic light scattering (DLS) and pH meter.

To verify the change of surface charge and diameter in the coacervation process, dynamic light scattering (DLS) analysis was carried out. The zeta-potential of MAP (1mg/ml) and $FeCl_3$ solution (10mM) were 27.0mV and 22.7mV, respectively. When increasing addition of MAP to the D-DW, zeta potential of solution increased continuously and reached -55.2 mV by addition of 100 wt%. As reported in reference [30], when absolute value of zeta potential is above ±40 mV, suspension was stable in aqueous phase having highly charged surface. Thus, MD-DW coacervate was stable in the emulsion and maintained their dispersion state. At the same time, size of coacervate was increased to 149.4 nm with increasing MAP amount, since MAP molecules wrapped the surrounding of D-DW. The pH behavior shows no particular change. It is expected that deprotonation of phosphate in ssDNA and protonation of amino group in MAP were equalized in the emulsion. [31, 32]

By addition of $FeCl_3$ solution until 200 μl, zeta potential was increased by positively charged Fe^{3+} solution and their size was increased to 201.6 nm. This result indicates that the addition of $FeCl_3$ induces the coordinative bonding between Fe^{3+} and MAP on the surrounding of MD-DW coacervate, so that size of particle was increased. However, after addition above 200 μl, zeta potential was rapidly approaching to 0 mV as

hydrophobic, furthermore, their size grew up to micro-scale. As results of that, coacervates could not maintain dispersion state, as results of that, precipitated in aqueous phase. In addition, pH was rapidly decreased to acidic condition, because formation between Fe^{3+} and MAP caused rapid deprotonation of hydroxyl group in MAP. Consequently, it is confirmed that addition of $FeCl_3$ help the growth of coacervate, but excessive amounts induce unstable dispersion state.

4.3.3.5 Conversion FMD-DW Coacervate to Aerogel

In above chapter, to confirm the optical and electrostatic properties of FMD-DW coacervate, D-DW supernatant after centrifugation was used in the Raman, UV-Vis-NIR and DLS analysis. Therefore, to identify the effect of DWNTs for gelation, FMD-DW emulsion having high DWNTs contents (hFMD-DW) was prepared from just sonicated D-DW without centrifugation.

hFMD-DW coacervate was prepared by addition of 60 ul of $FeCl_3$ solution into MD-DW emulsion which is mixture of sonicated D-DW dispersion and 50 wt% (vs ssDNA) of MAP. At this time, the concentration of DWNTs was 0.1 mg/ml. Prepared hFMD-DW emulsion was concentrate in the vacuum chamber for 12 h to achieve DWNTs concentration by 0.5 mg/l, and subsequent mild sonication was applied (Figure 4.3.9).

As shown in Figure 4.3.10, after concentration, hFMD-DW emulsion had drastic high viscosity, so that flowability was very low when turned upside down, although FMD-DW from D-DW supernatant (after centrifugation) is easily flowed down. Therefore, these results indicated that DWNTs ratio is important factor for gelation and DWNTs were worked as cross-linker between coacervate. These prepared coacervate gels were freeze dried for 48 h to convert them into aerogel phase.

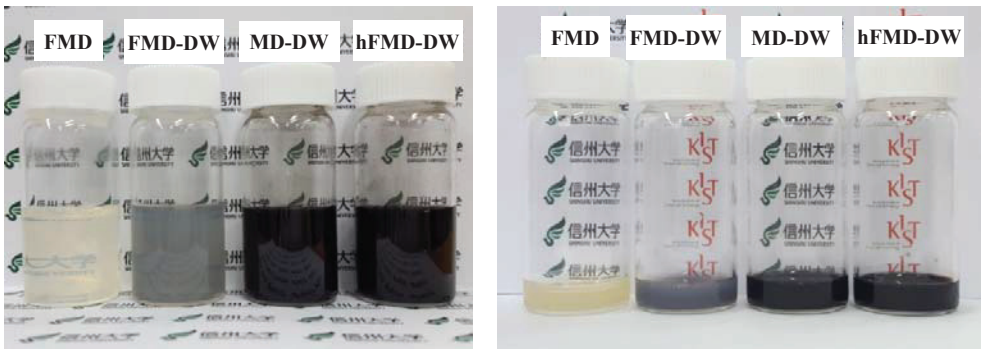

(a) Coacervate emulsion (b) After concentration

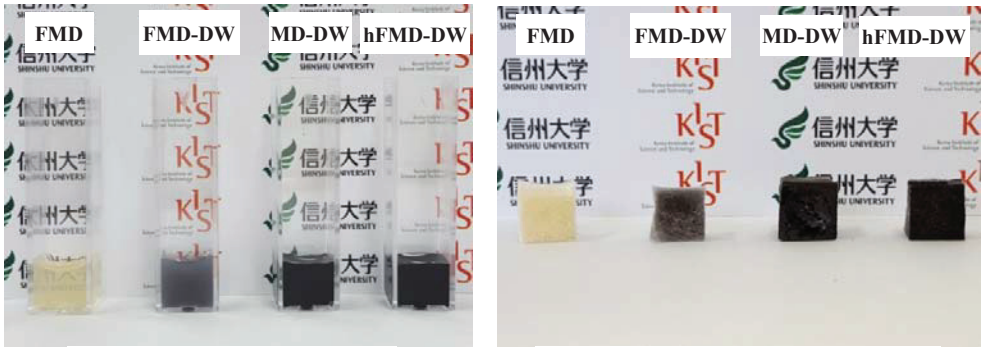

(c) After Concentration (in cuvette cell) (d) Conversion to aerogel (Freeze drying)

Figure 4.3.9 Digital photos of conversion coacervate emulsion to aerogel.

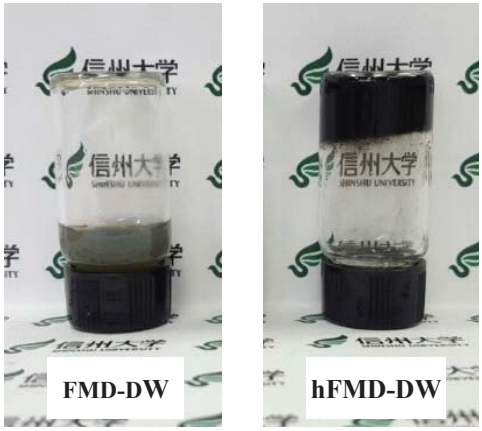

Figure 4.3.10 The flowability of FMD-DW and hFMD-DW after concentrate.

4.3.3.6 Physical Performance of FMD-DW Aerogel

To verify the mechanical durability of hFMD-DW aerogel, simple pressing test was carried out. As shown in Figure 4.3.11, sample of FMD without DWNTs and FMD-DW were completely compressed by pressing using slide glass (ca. 8.3g). In other hand, sonicated FMD-DW aerogel was maintained their shape. This result indicated that DWNTs worked as reinforcing agent of cross-linker for coacervate.

Electrical performance was identified by simple Current flow test of hFMD-DW aerogel using LED bulb (Figure 4.3.12). When the anode contacted on the aerogel surface, blue LED bulb was turn on, thus, it is confirmed that entire hFMD-DW aerogel is electrically conductive.

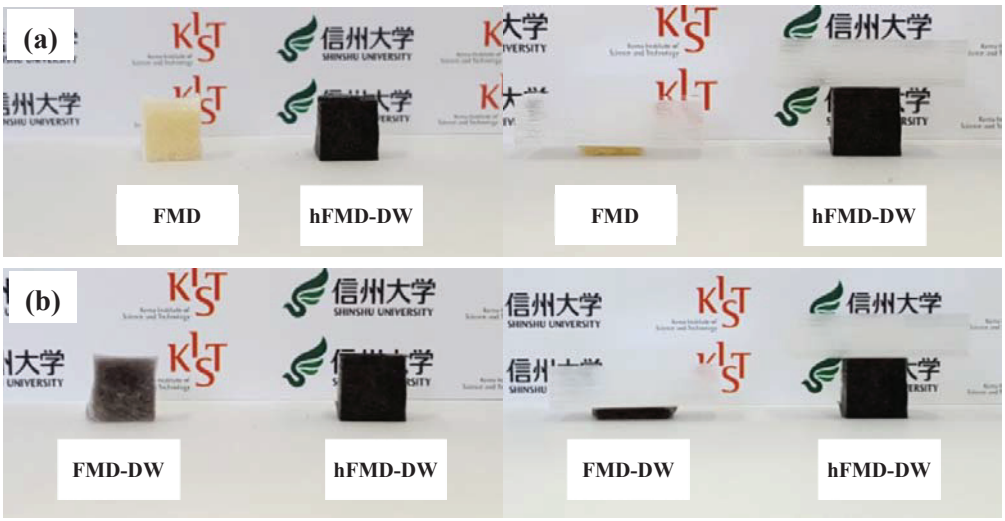

Figure 4.3.11 Pressing test of (a) FMD and hFMD-DW, and (b) FMD-DW and hFMD-DW

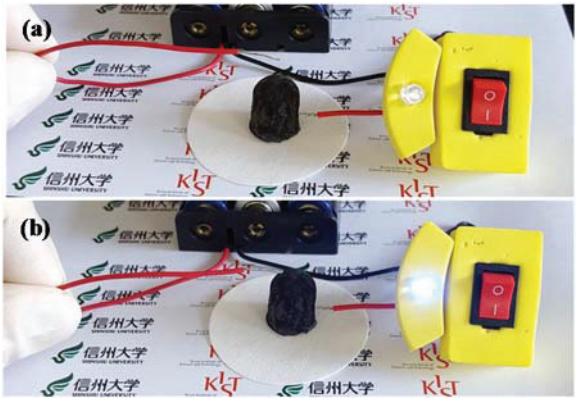

Figure 4.3.12 Current flow test of hFMD-DW aerogel using LED bulb

4.3.4 Conclusion

In summary, I have successfully prepared mechanically strong, electrically conductive and biocompatible metal-absorbed aerogel containing DWNTs by gelating MAP-ssDNA coacervation. In order to confirm opto-chemical changing of the coacervation and gelation process, optical measurement such as Raman/fluorescence and UV-Vis-NIR spectroscopy were carried out. MAP-ssDNA-DWNT coacervates had different chemical state from ssDNA- or MAP-dispersed DWNTs, and they maintained dispersion state of DWNTs. Moreover, surface charge, diameter and stability in aqueous phase of coarcervates were verified using the dynamic light scattering (DLS) measurement. The prepared FMD-DW coacervate emulsion was converted to aerogel by concentration and freeze drying process. We found that DWNTs acted as cross-linker between coacervate when converting sol to gel. The prepared FMD-DW aerogel was mechanically stable and electrically conductive, indicating that DWNTs are good reinforcing agent and cross-linker to improve physical performance. Consequently, it is expected that optically active, mechanically strong, electrically conductive, and biologically active metal-absorbed MAP-ssDNA-DWNTs coacervate should find many potential uses in the biological and medical areas.

4.3.5 References

[1] A.E. Aliev, J.Y. Oh, M.E. Kozlov, A.A. Kuznetsov, S.L. Fang, A.F. Fonseca, R. Ovalle, M.D. Lima, M.H. Haque, Y.N. Gartstein, M. Zhang, A.A. Zakhidov, R.H. Baughman, *Science,* **323**, 1575-1578, (2009)

[2] J.T. Korhonen, P. Hiekkataipale, J. Malm, M. Karppinen, O. Ikkala, R.H.A. Ras, *Acs Nano,* **5**, 1967-1974, (2011)

[3] R.T. Olsson, M.A.S.A. Samir, G. Salazar-Alvarez, L. Belova, V. Strom, L.A. Berglund, O. Ikkala, J. Nogues, U.W. Gedde, *Nat Nanotechnol,* **5**, 584-588, (2010)

[4] T.Y. Wei, C.H. Chen, H.C. Chien, S.Y. Lu, C.C. Hu, *Adv Mater,* **22**, 347-+, (2010)

[5] H. Bungenberg de Jong, H. Kruyt, *Kruyt, H, Ed,* 335-432, (1949)

[6] W.D. Nes, *Journal of the American Chemical Society,* **121**, 1625-1625, (1999)

[7] Y.F. Wang, J.Y. Gao, P.L. Dubin, *Biotechnol Progr,* **12**, 356-362, (1996)

[8] K. Besteman, J.O. Lee, F.G.M. Wiertz, H.A. Heering, C. Dekker, *Nano Lett,* **3**, 727-730, (2003)

[9] P. Asuri, S.S. Karajanagi, E. Sellitto, D.Y. Kim, R.S. Kane, J.S. Dordick, *Biotechnol Bioeng,* **95**, 804-811, (2006)

[10] L. Cooper, H. Amano, M. Hiraide, S. Houkyou, I.Y. Jang, Y.J. Kim, H. Muramatsu, J.H. Kim, T. Hayashi, Y.A. Kim, M. Endo, M.S. Dresselhaus, *Appl Phys Lett,* **95**, (2009)

[11] A.B. Dalton, S. Collins, E. Munoz, J.M. Razal, V.H. Ebron, J.P. Ferraris, J.N. Coleman, B.G. Kim, R.H. Baughman, *Nature,* **423**, 703-703, (2003)

[12] M. Endo, H. Muramatsu, T. Hayashi, Y.A. Kim, M. Terrones, N.S. Dresselhaus, *Nature,* **433**, 476-476, (2005)

[13] W. Shi, Z. Wang, Q.C. Zhang, Y. Zheng, C. Ieong, M.Q. He, R. Lortz, Y. Cai, N. Wang, T. Zhang, H.J. Zhang, Z.K. Tang, P. Sheng, H. Muramatsu, Y.A. Kim, M. Endo, P.T. Araujo, M.S. Dresselhaus, *Sci Rep-Uk,* **2**, (2012)

[14] M.A. Worsley, J.H. Satcher, T.F. Baumann, *Langmuir,* **24**, 9763-9766, (2008)

[15] J.H. Kim, M. Kataoka, D. Shimamoto, H. Muramatsu, Y.C. Jung, T. Hayashi, Y.A. Kim, M. Endo, J.S. Park, R. Saito, M. Terrones, M.S. Dresselhaus, *Acs Nano,* **4**, 1060-1066, (2010)

[16] Y.C. Jung, H. Muramatsu, K. Fujisawa, J.H. Kim, T. Hayashi, Y.A. Kim, M. Endo, M. Terrones, M.S. Dresselhaus, *Small,* **7**, 3292-3297, (2011)

[17] Y.I. Ko, C.S. Kang, E.A. Shin, Y.C. Jung, H. Muramatsu, T. Hayashi, Y.A. Kim, M.S. Dresselhaus, *Rsc Adv,* **6**, 16308-16313, (2016)

[18] T.M. Rana, *Nat Rev Mol Cell Bio,* **8**, 23-36, (2007)

[19] B.P. Lee, P.B. Messersmith, J.N. Israelachvili, J.H. Waite, *Annu Rev Mater Res,* **41**, 99-132, (2011)

[20] Y.A. Kim, H. Muramatsu, T. Hayashi, M. Endo, M. Terrones, M.S. Dresselhaus, *Chem Vapor Depos,* **12**, 327-+, (2006)

[21] M.J. O'Connell, S.M. Bachilo, C.B. Huffman, V.C. Moore, M.S. Strano, E.H. Haroz, K.L. Rialon, P.J. Boul, W.H. Noon, C. Kittrell, J.P. Ma, R.H. Hauge, R.B. Weisman, R.E. Smalley, *Science,* **297**, 593-596, (2002)

[22] A.M. Rao, E. Richter, S. Bandow, B. Chase, P.C. Eklund, K.A. Williams, S. Fang, K.R. Subbaswamy, M. Menon, A. Thess, R.E. Smalley, G. Dresselhaus, M.S. Dresselhaus, *Science,* **275**, 187-191, (1997)

[23] S. Reich, C. Thomsen, P. Ordejon, *Phys Rev B,* **65**, (2002)

[24] J. Lefebvre, J.M. Fraser, Y. Homma, P. Finnie, *Appl Phys a-Mater,* **78**, 1107-1110, (2004)

[25] Y. Miyauchi, R. Saito, K. Sato, Y. Ohno, S. Iwasaki, T. Mizutani, J. Jiang, S. Maruyama, *Chem Phys Lett,* **442**, 394-399, (2007)

[26] J. Maultzsch, H. Telg, S. Reich, C. Thomsen, *Phys Rev B,* **72**, (2005)

[27] D.A. Heller, P.W. Barone, J.P. Swanson, R.M. Mayrhofer, M.S. Strano, *J Phys Chem B,* **108**, 6905-6909, (2004)

[28] A. Jorio, A.P. Santos, H.B. Ribeiro, C. Fantini, M. Souza, J.P.M. Vieira, C.A. Furtado, J. Jiang, R. Saito, L. Balzano, D.E. Resasco, M.A. Pimenta, *Phys Rev B,* **72**, (2005)

[29] M.S. Strano, V.C. Moore, M.K. Miller, M.J. Allen, E.H. Haroz, C. Kittrell, R.H. Hauge, R.E. Smalley, *J Nanosci Nanotechno,* **3**, 81-86, (2003)

[30] R. Greenwood, K. Kendall, *Journal of the European Ceramic Society,* **19**, 479-488, (1999)

[31] K. Kaibara, T. Okazaki, H. Bohidar, P. Dubin, *Biomacromolecules,* **1**, 100-107, (2000)

[32] J. Lazko, Y. Popineau, J. Legrand, *Colloids and Surfaces B: Biointerfaces,* **37**, 1-8, (2004)

Chapter 5

Conclusion

Chapter 5 Conclusion

My PhD thesis is constructed based on three parts; (a) the improvement both in the mechanical, thermodynamic performance and shape memory behavior of biodegradable electrospun nanofiber yarn prepared by twisting process, followed by coating with silicone elastomer, (b) the dispersion of hydrophobic carbon nanotubes by decorating with typical biomolecules (*e.g.*, ssDNA and mussel adhesive protein (MAP)), (c) the preparation of electrically conductive, mechanically tough and biocompatible nanocomposite using biofunctionalized carbon nanotubes.

The fabrication of silicone elastomer-coated polylactide nanofiber yarn was successfully prepared using the electrospinning system, twisting process, and coating (Chapter 2). Both the mechanical and thermodynamic properties of the polylactide nanofiber yarn were dramatically improved with increasing the width of nanofiber sheets as well as twisting number, due to the decreased voids and the increased internal friction within nanofiber yarn. The cross-sectioned SEM image of nanofiber yarn showed the complete infiltration of the silicone elastomer, indicating the biphasic bulk morphology. In addition, the higher rate in their shape memory behavior was observed for nanofiber yarn prepared by increasing slid width and twisting number.

Furthermore, I introduced a new type of shape memory polymer, silicone elastomer-coated polycaprolactone nanofiber yarn (Chapter 3). The coating process with silicone elastomer has greatly improved the thermomechanical properties of the as-spun polycaprolactone nanofiber yarn. In addition, annealing of the silicone elastomer-coated nanofiber yarn has contributed to the increase in the crystalline level of polycaprolactone, thereby resulting in the improvement of the toughness and elongation at break. The experimental results I achieved have a high probability of broadening the applications of the silicone elastomer-coated polycaprolactone nanofiber yarn, such as aerospace industry, biomedical devices, and smart textiles.

I have prepared individually dispersed DWNTs in an aqueous solution using MAP as dispersing agent and then examined the optical sensitivity of MAP-dispersed DWNT suspension with regard to the metal ion (Fe^{3+}) using various optical tools (Chapter 4.1). With increasing dispersion state of the MAP-dispersed DWNT suspension, the intensified absorption and luminescence peaks indicated that the DWNTs were individually isolated in an aqueous solution. In comparison with SDBS-dispersed DWNT suspension, the red shift in the absorption and luminescent peaks for the MAP-dispersed DWNT suspension can be explained in terms of both the altered band-gap and the dielectric screening effect. The addition of the $FeCl_3$ solution to MAP-dispersed DWNT supernatant created the formation of coordinative bond between the DOPA of MAP and

Fe^{3+} ion. From XPS spectra, we observed a transition from O-C to O-Fe bond, indicating the formation of DOPA-Fe^{3+} coordinative bonds, upon adding the $FeCl_3$ solution to MAP dispersed DWNT supernatant. The optical depression in the ferric chloride added MAP dispersed DWNT supernatant was verified by the disappearance of luminescence peaks and relative changes in the RBM intensities due to the formation of DOPA-Fe^{3+} bonds. The UV-Vis-NIR spectra also showed the loss of van Hove singularities with the broadened absorption peaks on the addition of $FeCl_3$ solution. Both the depression of the BWF line and RBM peak at 160 cm^{-1} associated with metallic outer tubes indicated that the circumferentially coated MAP-Fe^{3+} complex on the outer tubes largely altered the resonance condition of the outer tubes. We also observed the sensitive change in the optical properties of DWNTs when adding the $FeCl_3$ solution to MAP dispersed DWNT supernatant from the Raman, UV-Vis-NIR and PL studies. However, when the amount of $FeCl_3$ solution reached 50μl, the optical activities of DWNTs were completely depressed, indicating that DOPA groups in MAP were fully saturated with ca. 9.3wt% and ca. 3766.7mol% of Fe^{3+} ions.

I successfully modified the PVDF nanofiber yarn by coating with MAP-inspired DWNT suspension and then verified the large improvements of physical performance via the formation of metal absorbed complex and VUV irradiation (Chapter 4.2). I confirmed that MAP-dispersed DWNT solution was infiltrated into the nano-sized voids created by intersected nanofibers from the clear observation of the DWNT-derived Raman peaks (*e.g.*, G-, D-band and RBM), and luminescence of MAP. Moreover, the formation of Fe^{3+} absorbed complex was verified using a 785nm laser line by observing the RBM and luminescence changes of DWNTs. The mechanical properties of PVDF yarn was significantly enhanced by coating with MAP-dispersed DWNT suspension. Furthermore, Fe^{3+} absorbed MAP-DWNT coating contributed to the remarkable improvement of tensile toughness (ca. 61.1 %) as compared with that of uncoated nanofiber yarn. This enhancement is due to the formation of coordinative bonding between Fe^{3+} and MAP. I also observed the large improvement in the electrical conductivity by coating with MAP-dispersed DWNT suspension because DWNTs and Fe^{3+} played large role in improving electric conductivity of nanofiber yarn. Furthermore, VUV treatment induced 13-fold enhancement in the electric conductivity. Consequently, it is confirmed that the infiltrated DWNTs within nanofiber yarn acted as both a strong reinforcing filler and electrical conductor and also the formation of metal absorbed complex and VUV treatment contributed to the large improvement in the mechanical and electrical properties of the coated nanofiber yarn.

Finally, I prepared mechanically strong, electrically conductive and biocompatible carbon nanotube-based aerogel via the judicious combination of ssDNA

and MAP (Chapter 4.3). In order to opto-chemically confirm the coacervation and gelation process, Raman/fluorescence and UV-Vis-NIR spectra were measured. MAP/ssDNA/DWNT coacervate exhibited different chemical state compared to ssDNA- or MAP-dispersed DWNTs, and DWNTs were in good dispersion state. Surface charge, diameter and stability in an aqueous phase of coacervate were verified using the dynamic light scattering measurement. MAP/ssDNA/DWNT coacervate emulsion was easily converted to aerogel via the concentrating process and the subsequent freeze drying process. I clearly observed that DWNTs acted as cross-linker in a coacervate state. The MAP/ssDNA/DWNT aerogel was mechanically stable and electrically conductive, indicating that DWNTs acted as good reinforcing filler. It is envisaged that MAP/ssDNA/DWNTs coacervate can be used in various biological and medical areas, where optical activity, mechanical strength, electrical conductivity, and biological activities are critically required.

Publications

[1] Yong-Il Ko, Yumi Ha, Cheol-Min Yang, Takuya Hayashi, Yoong Ahm Kim, Morinobu Endo, Yong Chae Jung, Flexible Transparent Conducting Film Using Photo-chemically Oxidized Thin-Multi Walled Carbon Nanotubes, Journal Of Nanoscience And Nanotechnology, *Journal Of Nanoscience And Nanotechnology*, 2016, **16**, 11980-11985

[2] Hyunjung Lee, Yu-Mi Ha, Sang Hyun Lee, Young-il Ko, Hiroyuki Muramatsu, Yoong Ahm Kim, Min Park, Yong Chae Jung, Spontaneously Restored Electrical Conductivity of Bioactive Gel Comprising Mussel Adhesive Protein-Coated Carbon Nanotubes, *RSC Advances*, 2016, **6**, 87044–87048

[3] Cheon-Soo Kang, Kazunori Fujisawa, Yong-Il Ko, Hiroyuki Muramatsu, Takuya Hayashi, Morinobu Endo, Hee Jou Kim, Daun Lim, Jin Hee Kim, Yong Chae Jung, Mauricio Terrones, Mildred S. Dresselhaus, Yoong Ahm Kim, Linear carbon chains inside multi-walled carbon nanotubes: Growth mechanism, thermal stability and electrical properties, *Carbon*, 2016, **107**, 217-224

[4] Yong-Il Ko, Cheon-Soo Kang, Eun-Ae Shin, Yong Chae Jung, Hiroyuki Muramatsu, Takuya Hayashi, Yoong Ahm Kim, Mildred S. Dresselhaus, Optical Sensitivity of Mussel Protein-Coated Double-Walled Carbon Nanotube on Iron-DOPA Conjugation Bond, *RSC Advances*, 2016, **6(20)**, 16308-16313

[5] Hiroyuki Muramatsu, Kazunori Fujisawa, Yong-Il Ko, Kap-Seung Yang, Takuya Hayashi, Morinobu Endo, Cheol-Min Yang, Yong Chae Jung, Yoong Ahm Kim, A selective way to create defects by the thermal treatment of fluorinated double walled carbon nanotubes. Chinese Journal of Catalysis, *Chinese Journal of Catalysis*, 2014, **35(6)**, 864-868

[6] Yoong Ahm Kim, Shunta Aoki, Kazunori Fujisawa, Yong-Il Ko, Kap-Seung Yang, Cheol-Min Yang, Yong Chae Jung, Takuya Hayashi, Morinobu Endo, Mauricio Terrones, and Mildred S. Dresselhaus, Defect-Assisted Heavily and Substitutionally Boron Doped Thin Multi-Walled Carbon Nanotubes, *The Journal of Physical Chemistry C*, 2014, **118(8)**, 4454-4459

[7] Santosh Kumar Yadav, Yong Chae Jung, Cheol-Min Yang, Yong-Il Ko, Kap-Seung Yang, Yoong Ahm Kim and Jae Whan Chom, An Environmentally Friendly Approach to Functionalizing Carbon Nanotubes for Fabricating Strong Biocomposite Films, *RSC Advances*, 2014, **4(11)**, 5382-5388

[8] Yong-Il Ko, Yujin Lee, Kesavan Devarayan, Byoung-Suhk Kim, Takuya Hayashi, Ick-SooKim, Annealing effects on mechanical properties and shapememory behaviors of silicone-coated elastomeric polycaprolactone nanofiber filaments, *Materials Letters*, 2014, **131**, 128-131

[9] Jong Woo Yi, Yong Il Ko, Jin-Seok Bae, Evaluation of new phospholipid MPCE finishing agent for polyester, *Fibers and Polymers*, 2013, **14(11)**, 1817-1825

[10] Hiroyuki Muramatsu, Takuya Hayashi, Kazunori Fujisawa, Tomohiro Tojo, Yong-Il Ko, Aaron Morelos-Gomez, Kap-Seung Yang, Yoong Ahm Kim, Morinobu Endo, Mauricio, Terronesef and Mildred S. Dresselhausg, Boron-Assisted Coalescence of Parallel Multi-Walled Carbon Nanotubes, *RSC Advances*, 2013, **3(48)**, 26266-26270

[11] Santosh Kumar Yadav, Yong Chae Jung, Jin Hee Kim, Yong-Il Ko, Hee Jeong Ryu, Mukesh Kumar Yadav, Yoong Ahm Kim, and Jae Whan Cho, Mechanically Robust, Electrically Conductive Biocomposite Films Using Antimicrobial Chitosan-Functionalized Graphenes, *Particle&particle System Characterization*, 2013, **30(8)**, 721-727

[12] Jin Hee Kim, Masakazu Kataoka, Yong Chae Jung, Yong-Il Ko, Kazunori Fujisawa, Takuya Hayashi, Yoong Ahm Kim, and Morinobu Endo, Mechanically Tough, Electrically Conductive Polyethylene Oxide Nanofiber Web Incorporating DNA-Wrapped Double-Walled Carbon Nanotubes, *ACS Applied Materials & Interfaces*, 2013, **5(10)**, 4150-4154

[13] Yong-Il Ko, Byoung-Suhk Kim, Jin-Seok Bae, Yoong-Ahm Kim and Ick-Soo Kim, Silicone-coated elastomeric polylactide nanofiber filaments: mechanical properties and shape memory behavior, *RSC Advances*, 2013, **3(40)**, 20091-20098

[14] Yong-Il Ko, Jong Woo Lee, Sung-Hoon Kim, Jin-Seok Bae, Synthesis of New Phospholipid Biocompatible Textile Finishing Agent, *Textile Coloration and Finishing*, 2010, **22(4)**, 293-299

Acknowledgements

When I decided to start my PhD course in Japan, the nanoscience and nanotechnology regarding the study and application of very small things made me hard to do research. However, with the lavish help of many people, I completed my doctoral course and took the first step towards research field of nanoscience and nanotechnology. So I would like to thank all of people who encouraged and helped me with valuable guidance and assistance.

First of all, I would like to thank Prof. Yoong Ahm Kim of Chonnam National University and Prof. Takuya Hayashi of Shinshu National University for giving me this opportunity, continuous guidance and support during my PhD course. They always led me to a correct way as scientist. Dear Prof. Kim and Hayashi, thank you very much for everything.

I wish to thank Prof. Ick-Soo Kim of Shinshu National University and Prof. Jin-Seok Bae of Kyungpook National University for giving me the chance to enter into this exciting area, and I also thank Prof. Hiroyuki Muramatsu of Shinshu National University and Prof. Byoung-Suhk Kim of Chonbuk National University for many valuable advices about not only technical experiment but also mindset as researcher.

Also I would like to express my gratitude to the Dr. Yong-Chae Jung in Korea Institute of Science and Technology (KIST) for both material and spiritual support at tough times and giving me a chance to continue my research.

Finally, I would like to give my special thanks to my family, especially my parents and fiancee. It was possible to finish this thesis and I could stand here by their continuous encouragement and unlimited support. So I am very much grateful for being able to say that I have a great family. Thanks again.